



**Michigan
Technological
University**

Michigan Technological University
Digital Commons @ Michigan Tech

Dissertations, Master's Theses and Master's Reports

2018

LINEAR RING RESONATOR MODULATOR FOR MICROWAVE PHOTONIC LINKS

Arash Hosseinzadeh

Michigan Technological University, ahosseini@mtu.edu

Copyright 2018 Arash Hosseinzadeh

Recommended Citation

Hosseinzadeh, Arash, "LINEAR RING RESONATOR MODULATOR FOR MICROWAVE PHOTONIC LINKS",
Open Access Dissertation, Michigan Technological University, 2018.
<https://digitalcommons.mtu.edu/etdr/661>

Follow this and additional works at: <https://digitalcommons.mtu.edu/etdr>



Part of the [Electromagnetics and Photonics Commons](#)

LINEAR RING RESONATOR MODULATOR FOR MICROWAVE PHOTONIC
LINKS

By

Arash Hosseinzadeh

A DISSERTATION

Submitted in partial fulfillment of the requirements for the degree of

DOCTOR OF PHILOSOPHY

In Electrical Engineering

MICHIGAN TECHNOLOGICAL UNIVERSITY

2018

© 2018 Arash Hosseinzadeh

This dissertation has been approved in partial fulfillment of the requirements for the Degree of DOCTOR OF PHILOSOPHY in Electrical Engineering.

Department of Electrical and Computer Engineering

Dissertation Advisor: *Dr. Christopher T. Middlebrook*

Committee Member: *Dr. Paul L. Bergstrom*

Committee Member: *Dr. Durdu Guney*

Committee Member: *Dr. Miguel Levy*

Department Chair: *Dr. Daniel R. Fuhrmann*

Table of Contents

Chapter 1:	Microwave Photonics.....	1
1.1	Analog fiber optic communication	1
1.2	Microwave photonics links figure of merits	4
1.2.1	Gain.....	4
1.2.2	Noise figure.....	5
1.2.3	Spur-free dynamic range.....	6
Chapter 2:	Electro-optic Modulation	10
2.1	Electrical-to-Optical modulation strategies	10
2.2	External modulator materials.....	11
2.3	Mach-Zehnder Interference (MZI) modulators	14
2.4	Ring resonator modulators (RRM)	17
Chapter 3:	Nonlinearity Analysis of a Ring Resonator Modulator	23
3.1	Static analysis	23
3.2	Dynamic analysis.....	27
3.3	Harmonic distortions	30
3.4	SFDR and operational bandwidth.....	32
3.5	Noise bandwidth effects on SFDR	35
3.6	Ring-waveguide coupling condition tolerances.....	38
3.7	Ring resonator modulator for radio-over-fiber applications.....	40
3.8	Summary.....	42
Chapter 4:	Dual Ring Resonator Modulator	45
4.1	IMD3 suppression strategy	46
4.2	DRRM figure of merits.....	54

4.3	Summary.....	61
Chapter 5: Ring Resonator Modulator Design.....		62
5.1	Photonic device simulation methods	62
5.2	Single mode optical waveguides	64
5.3	Ring resonator coupling condition design	68
5.4	Optical power splitter design for DRRM.....	71
5.5	Summary.....	73
Chapter 6: Fabrication of All-polymer Electro-optic Modulation Devices		75
6.1	Material selection.....	75
6.2	Fabrication Procedure.....	76
6.3	Summary.....	82
Chapter 7: RRM Characterizations		83
7.1	Resonance	85
7.2	Modulation index.....	88
7.3	Analog modulation	90
7.4	DRRM characterizations	93
7.5	Summary.....	95

Abstract

Modulators within Microwave photonic links (MPLs) encode Radio Frequency (RF) signal information to the optical domain for transmission in applications such as wireless access networks and antenna remoting exploiting advantages optical fiber offers over RF coaxial cables including bandwidth, loss, size, weight, and immunity to electromagnetic interference. A critical figure-of-merit in MPLs is spur-free-dynamic-range (SFDR) defining the range of RF signal power a MPL transmits without distortion. Current Mach-Zehnder Interference (MZI) modulators used in MPLs limit the SFDR because of the associated nonlinear sinusoidal transfer function.

A rigorous theoretical method is developed followed by design, fabrication, and testing to investigate a linear ring resonator modulator (RRM) modulator for MPLs. The linear nature of the Lorentzian transfer function for the RRM is utilized over the sinusoidal transfer function within MZI modulators offering significant improvement in MPL SFDR. A novel bias voltage adjustment method is developed for practical implementations improving SFDR of 6 dB versus MZI at 500 MHz noise bandwidth. RRM is shown to be applicable for applications requiring high operational frequencies while in a limited operational bandwidth such as millimeter-wave wireless networks. To improve RRM SFDR in wide operational bandwidths a novel dual ring resonator modulator (DRRM) design is demonstrated. DRRM suppresses the third order intermodulation distortion in a frequency independent process removing SFDR limits of RRM.

Chapter 1: Microwave Photonics

1.1 Analog fiber optic communication

The invention of laser as the coherent source of light [1] and optical fiber for transporting light [2] opened a door to the fiber-optic communication era. Significant effort has been devoted to develop and implement fiber-optic communication systems for transmitting, processing, and detecting electronic signals. Fiber-optic communication systems provides highly efficient and flexible data communication systems due to compelling advantages of optical fibers. Optical fibers tremendously reduce system weight, size, and signal loss [3]. For example, coaxial cables typically weigh 567 kg/km while posing 360 dB/km loss (at 2 GHz) [3]. In contrast, common optical fibers weigh and loss are 1.7 kg/km and 0.5 dB/km respectively [3]. Optical fibers have THz bandwidths in comparison to GHz bandwidth capacity of coaxial cables [3]. Optical fibers are immune to electromagnetic interference (EMI) effects providing a more compact routing in a noisy RF environment.

To convey electrical signals using optical fibers there are two fundamental building blocks in either digital or analog applications as shown in Figure 1-1. The first block is to encode the data signal from the electrical domain to optical domain in a process known as modulation. The second block is to recover the original electrical data signal from optical domain at the end of the link referred to as de-modulation.

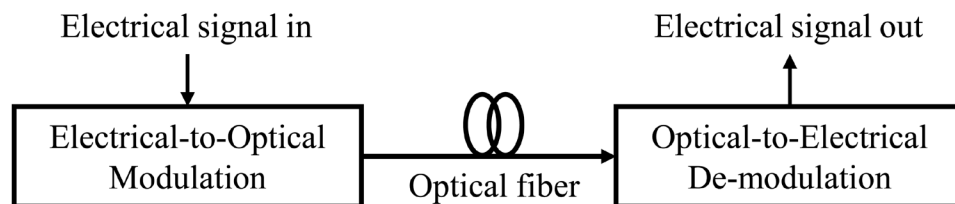


Figure 2-1 A basic schematic of a fiber-optic communication link.

Fiber-optic communication links are widely implemented for a multitude of digital applications, large capacity links for long-haul applications [4], fiber-to-home network deployments [5], and rack-to-rack and module-to-module interconnects within data centers [6]. However digital links have limited success in conveying analog signals because of required digitization process using analog-to-digital converters (ADC). Operational bandwidths of ADCs are in the range of 1 GHz, limited primarily by the electronic sampling rate [7]. To convey analog signals with bandwidths beyond capabilities of ADCs multiple units of frequency down-conversions and ADCs are needed which makes the link complex, power hungry, bulky, and costly [8]. Analog fiber-optic links are critical for application such as antenna remoting where digital signal transmission is difficult to apply or even not possible. As shown in Figure 1-2 analog link yields wider bandwidth with simpler, smaller and less power consuming antenna sites by removing ADCs and downconverters.

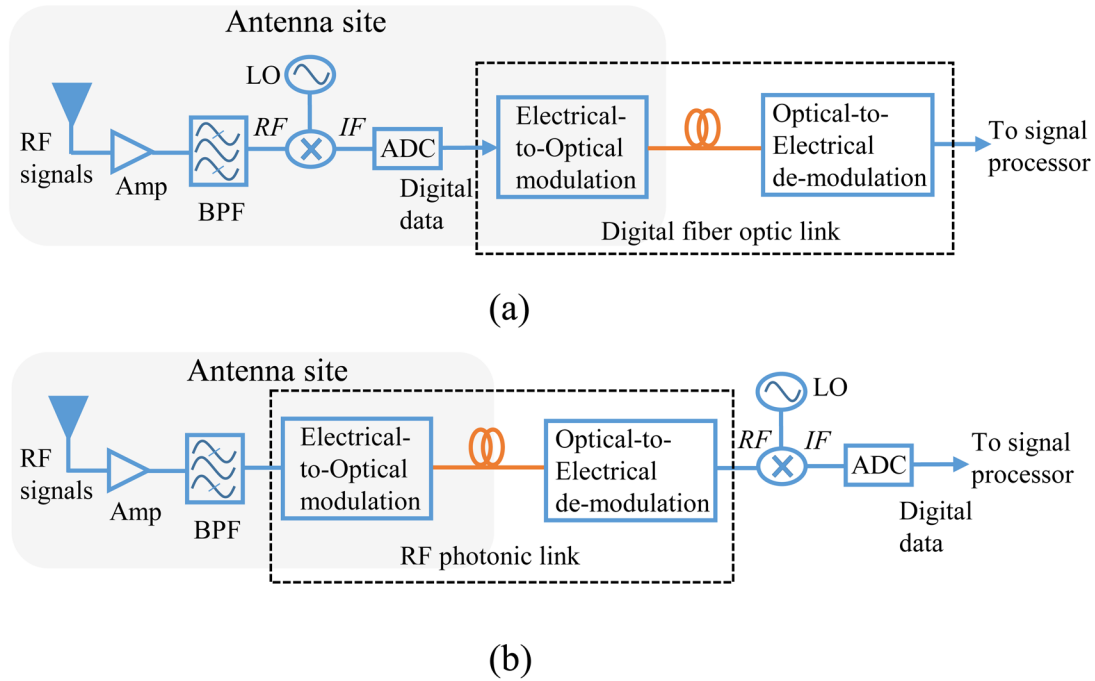


Figure 2-2 Comparison of fiber optic link component requirements using (a) digital fiber optic link, and (b) analog fiber-optic link.

Analog fiber-optic links which are referred to as microwave photonic links (MPLs) is the main part of a broader multidisciplinary field named as microwave photonics (MWP) with applications in various optical and microwave systems such as wireless access networks [9], cellular [10] and satellite communication [11], radars [12], cable television [13], antenna remoting [14], optical signal processing [15], and medical imaging [16]. MWP consists of photonic devices operating at microwave frequencies and has evolved traditional microwave systems by introducing photonic unique capabilities, enabling key functionalities in microwave systems which are very complex or even not possible in the microwave domain. MWP contributes in microwave systems through various critical functions including generation [17, 18], distribution [19, 20], and processing [15] of microwave signals.

Initially MPLs in the commercial sector were driven by analog cable TV networks (CATV) where MPLs were commercialized and many CATV networks deployed utilizing MPLs in 1990s [13, 21-23]. However by advancing digital TV networks CATV networks have replaced by digital networks. Currently radio-over-fiber (RoF) applications are considered as drivers of MPLs with rapid advancing applications in wireless access networks and distributed antenna systems [9, 24-26]. The proliferation of mobile devices and ever-increasing demand for broadband multimedia services has led a worldwide interest to pursue solutions providing multi-Gb/s data rates for large number of users. The RoF techniques can be used for wireless access networks installed in large buildings such as shopping malls, airports, stadiums, etc with large number of internet users [3]. In addition RoF is being actively pursued for cellular networks [9]. Wireless signals due to high loss in high frequency ranges pushes wireless network architectures towards using large number of antennas covering small areas. Utilizing MPLs to feed large number of antennas is a viable solution to increase capacity and reduce cost.

1.2 Microwave photonics links figure of merits

A MPL performance is evaluated utilizing figure-of-merits commonly used to evaluate RF components performances. The most critical figure-of-merits are gain (g_{MPL}), noise figure (NF), and spur-free dynamic range (SFDR) [27]. These parameters should meet the system level figure-of-merits dictated by each application in the required operational bandwidth.

To obtain figure-of-merits a MPL is considered as a unit with RF power entering and exiting the unit as shown in Figure 1-3. MPL figure-of-merits are dominated by the modulation and demodulation blocks. The intrinsic link therefore is a link solely consisting of modulation and demodulation stages while excluding any amplifiers or signal processing steps either in RF or optical domain [19, 27].

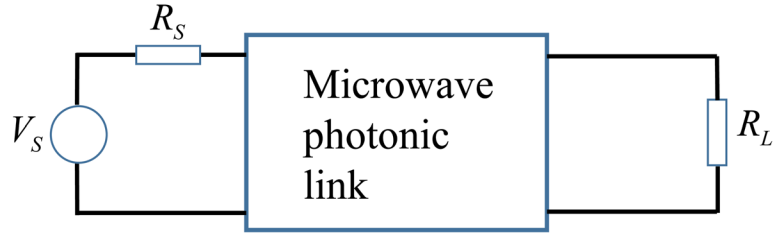


Figure 2-3 Simplified microwave system with MPL to calculate figure-of-merits.

1.2.1 Gain

The amount of RF input power passed by the MPL and delivered at the output is defined as the g_{MPL} . In a MPL modulation and demodulation performances have dominant effects in the g_{MPL} which can be defined according to Equation (1.1) [27]

$$g_{MPL} = S_m^2 R_{pd}^2 \quad (1.1)$$

where S_m is the modulation slope efficiency and R_{pd} is the photodetector responsivity factor. The units for S_m and R_{pd} are watts per ampere and amperes per watt respectively. To

characterize g_{MPL} using Equation (1.1) the MPL is impedance matched to R_s and R_L as shown in Figure (1-3) assuming $R_s = R_L$.

Common MPLs can limit g_{MPL} in the range of -20 dB and -40 dB [28]. Various methods have been proposed and utilized to improve g_{MPL} such as using low noise amplifiers (LNA), high power lasers, reducing MPL optical and electrical losses, and improving modulation and demodulation efficiencies [29]. LNAs diminish the considerable bandwidth advantage of using MPLs and add to the power consumption, system size, and vulnerability to electromagnetic interference effects. It is desired to improve g_{MPL} by removing the need for LNA [19, 29, 30] specially in applications such as compact antenna sites [31, 32], optoelectronic oscillators [18], and handling high power electromagnetic pulse effects [33]. Research efforts have made considerable progress improving g_{MPL} using MPL intrinsic elements [29].

1.2.2 Noise figure

One of the important figure-of-merits in MPLs is the noise figure (NF) which characterize signal-to-noise ratio (SNR) degradation by MPL [27]. NF is defined as the ratio of total output noise of MPL (N_{out}) and the portion of output noise because of the MPL input noise as described in Equation (1.2) [27]. The input noise to MPL is considered as thermal noise formulated by $k_B T_0 B$ where k_B is Boltzmann's constant, T_0 is the temperature, and B is the instantaneous bandwidth [34]. The input noise is either amplified or attenuated due to the intrinsic MPL gain (g_{MPL}). The output noise of MPL (N_{out}) is formulated as Equation (1.3) showing the MPL contribution to the microwave system noise level due to the relative intensity noise (RIN) of laser, photodetector shot noise, and MPL thermal noises. The RIN noise power appears in the electrical signal after the photodetector as $\langle I_D \rangle^2 R_D RIN$ where $\langle I_D \rangle$ is the average photodetector current and R_D is the detector terminating resistor [27]. The photodetector shot noise is a result of the statistical nature of random photon arrival

causing random fluctuations in the photodetector current and can be modeled as $2q\langle I_D \rangle R_D$ where q is the charge of an electron [35].

$$NF = 10 \log \left[\frac{N_{out}}{kT_0 B g_{MPL}} \right] \quad (1.2)$$

$$N_{out} = (I_D^2 R_D RIN + 2I_D R_D q + kT_0 g_{MPL} + kT_0) B \quad (1.3)$$

Initial MPLs without amplification impose more than -30 dB NF to the microwave system which is considered as a critical issue hindering MPLs advancement [19, 29, 36]. Similar to g_{MPL} a traditional way to improve the NF is to use LNAs which is not a viable solution for applications such as antenna remoting as mentioned in Section 1.2.1. Various methods have been developed to enhance NF of intrinsic MPLs including high power lasers with low RIN [37-41], suppressing $\langle I_D \rangle$ [19, 42-47], and improving g_{MPL} [19, 29, 30]. Depending on the application requirements and practicality these techniques can be implemented either individually or in combination to improve NF [48].

1.2.3 Spur-free dynamic range

SFDR defines the maximum and minimum RF power limits that can be transmitted or processed by a microwave system by quantifying the nonlinearity involved in microwave components. Nonlinearities cause harmonic distortions and intermodulation distortions. Harmonic distortions are at multiples of RF input signal frequency as shown in Figure 1-4(a). Intermodulation distortions happen when signals with different frequencies are mixed. For example by applying two signals with frequencies f_1 and f_2 distortion signals are generated at various frequencies such as $f_1 \pm f_2$ or $2f_2 \pm f_1$ as shown in Figure 1-4(b). Among various type of distortions the third order intermodulation distortion (IMD3) with frequencies $2f_2 \pm f_1$ or $2f_1 \pm f_2$ is the most critical distortion because IMD3 is always located inside the bandwidth and filtering out is either impossible or impractical [27]. In applications with multi-octave bandwidths ($f_{high} > 2f_{low}$) in addition to IMD3 the second

order intermodulation distortion (IMD2) at frequencies $f_1 \pm f_2$ and the second order harmonics at $2f_1$ are inside the band and therefore need to be considered in SFDR characterization of MPLs.

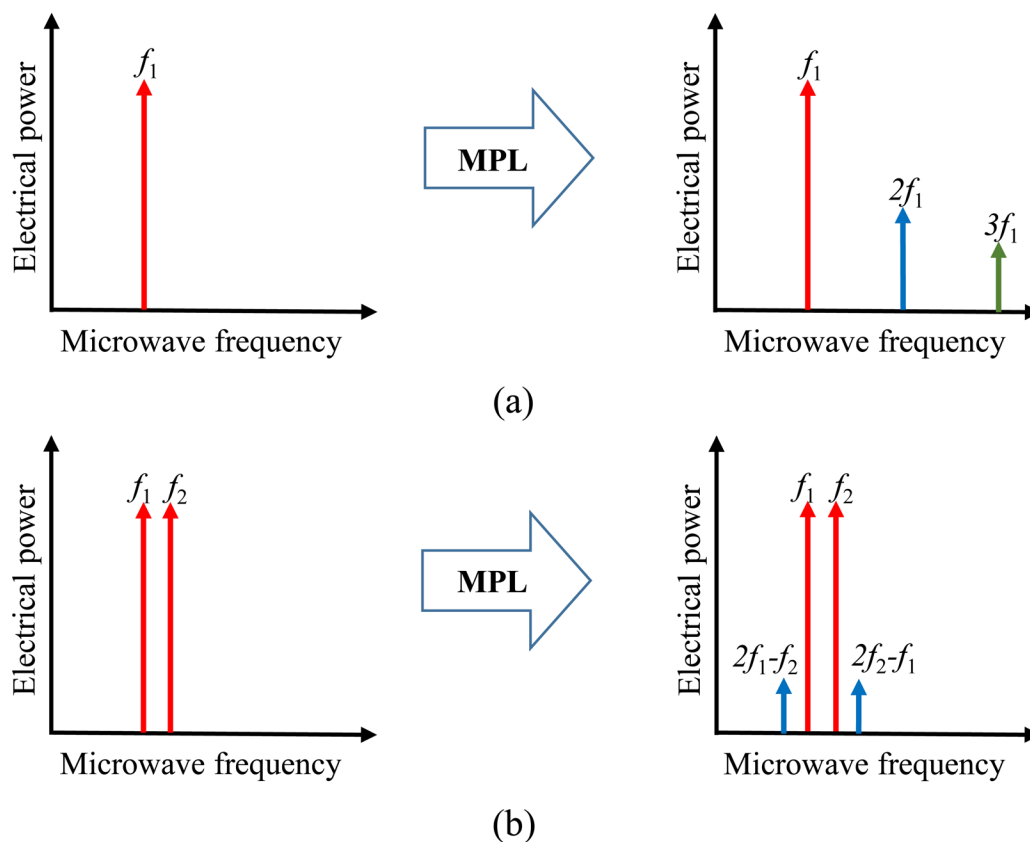


Figure 2-4 Distortions, (a) harmonic distortions, (b) third order intermodulation distortion (IMD3).

SFDR is the difference between maximum and minimum usable RF input signal powers as shown by P_1 and P_2 in Figure 1-5. The minimum useable input RF signal power (P_1) is determined when output RF signal power reaches the noise level meaning that if input RF power is decreased further the output signal power will no longer be distinguishable from the noise. On the other hand maximum RF input signal power (P_2) is defined when RF output distortion powers reach the noise level. If the input RF power is increased beyond P_2 the output RF power is distorted and link performance is degraded.

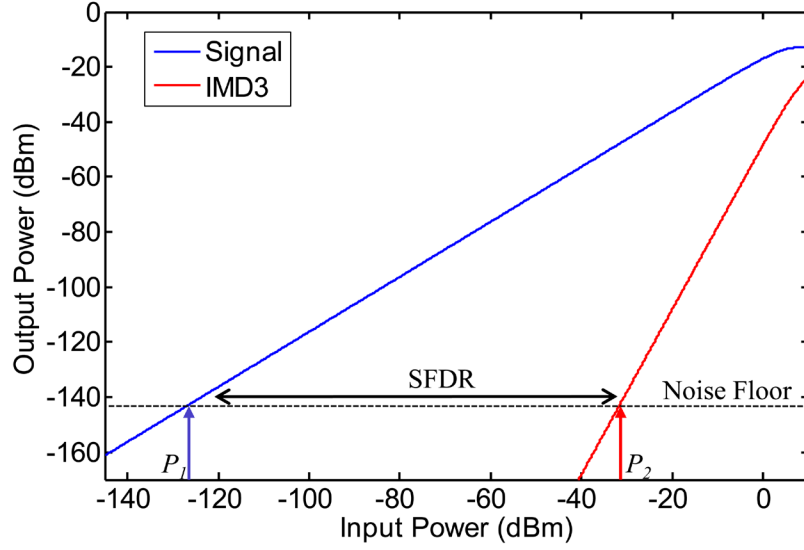


Figure 2-5 SFDR diagram of a microwave system.

SFDR is measured in dB according to MPL output noise level (N_{out}). Since N_{out} is related to noise bandwidth (B) as shown in Equation (1.2) a common practice is to calculate SFDR at 1 Hz noise bandwidth and report SFDR in the unit of $\text{dB}\cdot\text{Hz}^{(m-1)/m}$ where m is the slope of intermodulation distortion power change versus input RF power. SFDR at different noise bandwidths is calculated using Equation (1.3). It is worth mentioning that Equation (1.3) is useful when m is constant through the whole RF input power range of interest [49] otherwise SFDR needs to be characterized at each required noise bandwidth.

$$SFDR(B) = SFDR(1\text{Hz}) - \frac{m-1}{m} \times 10 \times \text{Log}(B) \quad (1.4)$$

SFDR of typical MPLs is $\sim 110 \text{ dB}\cdot\text{Hz}^{2/3}$ hindering MPL advancements for applications such as RoF [48, 50] demanding 10-20 dB higher SFDR. While all figure-of-merits of g_{MPL} , NF, and SFDR are critical for MPLs the SFDR holds a unique position in setting applicability of MPLs [27]. Various methods are utilized to improve g_{MPL} and NF of MPLs with success [45-47, 51, 52]. Despite vast amount of efforts, SFDR improvements have been with limited success and resulted MPLs are complex, difficult to implement and limited in bandwidth [19, 20, 27, 30, 48, 53]. Therefore SFDR remains as the main

drawback of MPLs full scale implementation and solving this problem is the top priority for MPW research and development [48, 50].

SFDR is critically limited by the nonlinearity of modulation process and a sole promising solution is to increase the modulation linearity. All existing modulation techniques are studied and fundamental limitations of current technologies are identified as described in the Chapter 2. Novel modulation methods are developed theoretically and verified experimentally which can improve SFDR of MPLs in the range of 10-20 dB. Proposed modulation techniques are promising for MPLs such as RoF application of wireless access networks.

Chapter 2: Electro-optic Modulation

2.1 Electrical-to-Optical modulation strategies

To modulate an electrical signal onto an optical wave several methods can be utilized including intensity [36], phase [54], frequency [55], and polarization [56]. Intensity modulation, where the light-wave intensity is modulated in proportion to an applied RF signal, is by far the most studied and implemented technique in MPLs since photodetectors detect intensity variations of light [19, 20, 29, 36, 57]. All other modulation types need to be converted to intensity modulation before photodetection yielding complexity and potential complications in the de-modulation scheme [54, 55, 58].

The intensity modulation links as shown in Figure 2-1 are called intensity modulation direct detection (IMDD) links [27] which can be conducted directly on the laser (direct modulation) as seen in Figure 2-1(a) or externally through a modulator separate from the laser as illustrated in Figure 2-1(b). The external modulation can be implemented in a wider application ranges versus direct modulation due to higher link figure-of-merits including gain (g_{MPL}), and bandwidth [19, 20, 36, 48]. The g_{MPL} in direct modulation is limited by laser diode efficiency and optical loss in the link [59] while external modulation provides higher g_{MPL} which can be controlled by the laser power and the modulation index of the external modulator. In addition the bandwidth in direct modulation is limited to few GHz because of frequency chirping [35].

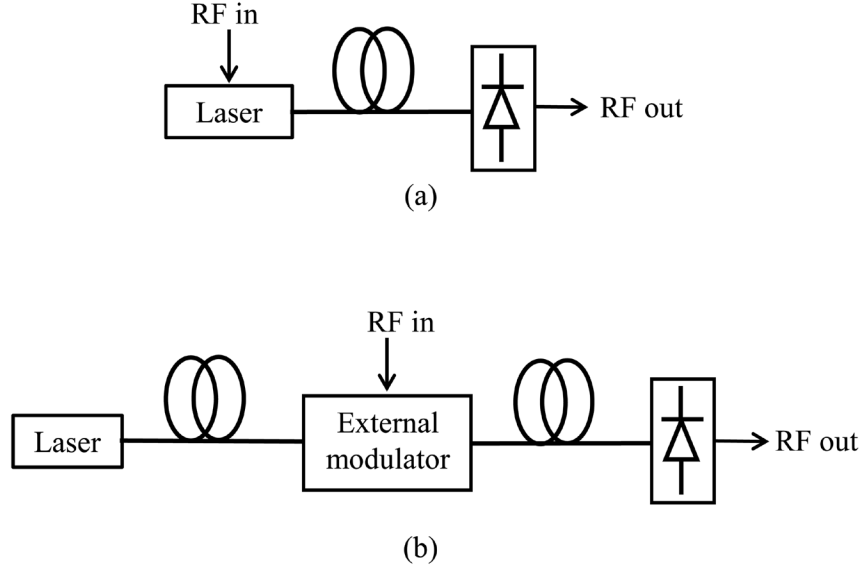


Figure 2-1 MPL schematic of intensity modulation and direct detection, (a) direct modulation, (b) external modulation.

2.2 External modulator materials

External modulators consist of electro-optically active materials which are utilized to fabricate light-wave transmission mediums (optical waveguides) while responding efficiently to the applied external voltage [60]. The refractive index of the electro-optically active materials changes according to electric field amplitude changes passing through the material [60]. The most implemented electro-optic effect in external modulators is the linear electro-optic effect or Pockel's effect where refractive index of material changes linearly versus applied electric field [60]. The refractive index change with linear polarization input light and the applied electric in one direction is simplified to Equation (2.1). The refractive index change is Δn , r is the electro-optic coefficient with regards to the electric field direction, n is the refractive index, and E is the applied electric field component.

$$\Delta n = -\frac{1}{2}n^3rE \quad (2.1)$$

Few types of materials are known so far that can present sufficient and applicable linear electro-optic properties [61]. One type of materials are inorganic crystals without inversion symmetry such as LiNbO_3 and III-V semiconductors [61]. Another type is especially designed organic materials named as electro-optic polymers [61].

The most studied and implemented electro-optic material is LiNbO_3 [61]. Modulators with LiNbO_3 are reliable devices able to be operational for years while tolerating the operational temperatures [62]. Commercial LiNbO_3 modulators pass the 10000 hours at 85°C operation tests and they can stand up to 125°C [62]. In addition LiNbO_3 modulators tolerate high optical power as much as 500 mW [19]. Optical waveguides fabricated by LiNbO_3 have low propagation loss (less than 0.2 dB/cm) and waveguides can be efficiently pigtailed to single mode optical fibers [63]. However LiNbO_3 advancement for MPL applications is hindered because of high power consumption, limited bandwidth, and bulky size. The LiNbO_3 maximum electro-optic coefficient is 30.8 pm/V which limits the modulation index causing high power consumption. The bandwidth is limited because of the large refractive index differences in microwave and optical frequencies as well as RF electrode loss [64]. The refractive index of LiNbO_3 at optical frequency is $n = 2.15$ while at microwave frequency is $n = 4.2$ causing phase velocity mismatch of propagating fields degrading the modulation index at high frequencies [65]. Various velocity matching techniques comes with the price of modulator index degradation, modulator length increase, higher RF electrode loss [65]. Moreover LiNbO_3 modulators, due to the limited modulation index, are bulky with lengths in the order of centimeters that can be used only as discrete component.

III-V semiconductors, compound of elements from III and V groups of periodic table, are considered as one of alternative platforms for electro-optic modulators especially for the purpose of integration. Two types of common III-V semiconductor modulators are based on GaAs and InP compounds that are widely used in other active devices such as amplifiers, lasers, photodetectors, and transistors [61]. Recently InP platform is gaining attentions for integration in MPLs [66, 67]. Electro-optic coefficients obtained from III-V semiconductor

compounds are low (~ 20 times less than LiNbO_3) however relatively efficient modulation is obtained due to large refractive indexes (InP: 3.2, GaAs: 3.4) small area of waveguide structure (2-3 μm) [63]. However low electro-optic coefficient, low optical power handling (< 50 mW), and high optical power loss (20 dB/mm) need to be improved for full implementation of III-V semiconductors in MPLs.

A type of syntactic organic materials called electro-optic polymers are designed to have strong linear electro-optic effects [68, 69]. A common type of electro-optic polymers is called guest-host polymers that consist of amorphous polymers as the host while nonlinear optical molecules called chromophores are doped into the host polymer as the active element. Various types of chromophores and host materials have been utilized so far to form electro-optic polymers [70]. Electro-optic polymers initially do not exhibit an electro-optic effect. Poling where an electric field is applied through the polymer to align chromophore dipoles inside the host polymer matrix creates an electro-optic effect [70].

Electro-optic polymers have very distinctive advantages that make them an attractive alternative to more mature structures. A prominent advantage is easy thin film fabrication process which can be applied on various types of substrates to form an active optical layer. This makes polymers promising candidates for integration to combine the active layer with various types of electronics and electro-optic components [71, 72]. Polymers can have high electro-optic coefficient (> 100 pm/V) which is critical parameter in modulators functionality. The electro-optic effect of polymers can respond to high frequencies in mm ranges making polymers as one of the widest bandwidth electro-optic materials. In addition very low refractive index difference in microwave and optical frequencies (~ 0.1) is another reason to make polymers very suitable for high frequency applications [73]. The optical, physical and chemical properties of polymers can be engineered to meet specific application requirement. This capability is possible because of various options of host and chromophores available to make polymers. In addition polymers have refractive indexes

around 1.6-1.7 which is lower than other electro-optic materials yielding an easier impedance matching process.

Main drawbacks of electro-optic polymers are their high optical power loss, low tolerance for optical power and environmental conditions. Polymers can get permanent damage at high optical powers (tens of milliwatts) [61, 74]. Polymers functionality is sensitive to the temperature and the humidity. High temperatures close to polymers glass transition temperature (T_g) can damage polymers [61]. Polymers are facing fast aging problem that chromophores in time lose their orientation degrading the electro-optic coefficient and polymer can get oxidized [61]. Optical waveguides fabricated with polymers have more than 2 dB/cm insertion loss. Electro-optic polymers are still in research stage and there are just a few examples of commercialized electro-optic polymers and the cost is relatively high [75]. Research in polymers is rapidly progressing to solve limitations mentioned [69, 70]. Specifically recent advances are moving towards solving problems of thermal stability and high optical power handling. New electro-optic polymers capable of standing up to 100-200 C and handling 100 mW are reported [74, 76].

2.3 Mach-Zehnder Interference (MZI) modulators

The most dominating and widely implemented type of modulator is intensity modulators based on MZI modulators [63]. A general schematic of MZI modulators is shown in Figure 2-2(a) where the input light is divided equally between two branches and recombines at the output. By applying voltage to branches the phase of optical wave passing through the branches are modulated versus each other. At the output the phase modulation translates to the intensity modulation due to the interference effects between two branches. When light-waves in two branches are in-phase the whole optical power transmits showing normalized transmission coefficient of one while output optical power is zero when light-waves are π radians out-of-phase. The MZI operational principle can be translated to a simple sinusoidal transfer function as Equation (2.2) and shown in Figure 2-2(b) [27]. V_π is the required voltage to bring the MZI modulator from “on” to “off” state by imposing π radian

phase difference between two branches. V_π determines the modulation index of MZI modulator and lower V_π yields higher modulation index improving link figure of merits of g_{MPL} and NF .

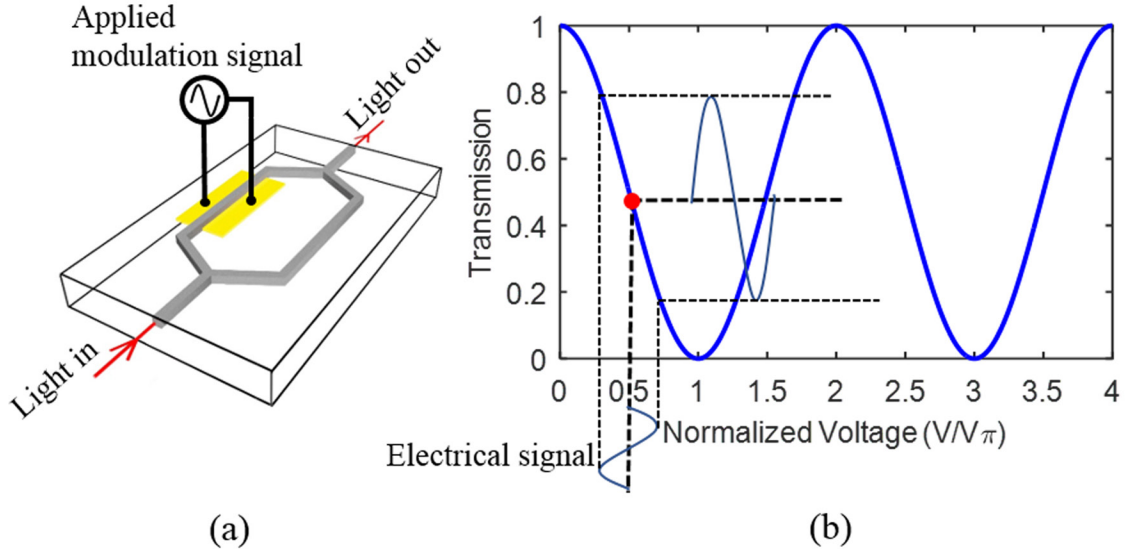


Figure 2-2 (a) A general schematic of MZI modulator, (b) sinusoidal transfer function of MZI modulator with showing common quadrature bias point.

$$Y(V_{dc}) = \left[\cos\left(\frac{\pi V_{dc}}{2V_\pi}\right) \right]^2 \quad (2.2)$$

Main advantages of a MZI modulator are the relative simple structure and well-defined transfer function. If material with linear electro-optic effect is utilized in MZI modulator Equation (2.2) is sufficient to accurately model MZI modulators in a MPL [49]. In addition MZI modulators specially with LiNbO_3 are reliable and enduring in time and working conditions.

However MZI modulators encounter substantial drawbacks which limit MZI modulator implementations in MPLs demanding high operational frequency, low power consumption, smaller foot-prints, and higher linearity. The modulation index decrease beyond 3 dB at

operational frequency ranges higher than 50 GHz due to the electrode loss and velocity mismatch between optical and RF frequencies as shown in Figure 2-3 which make MZI modulators not suitable for high frequency applications [73].

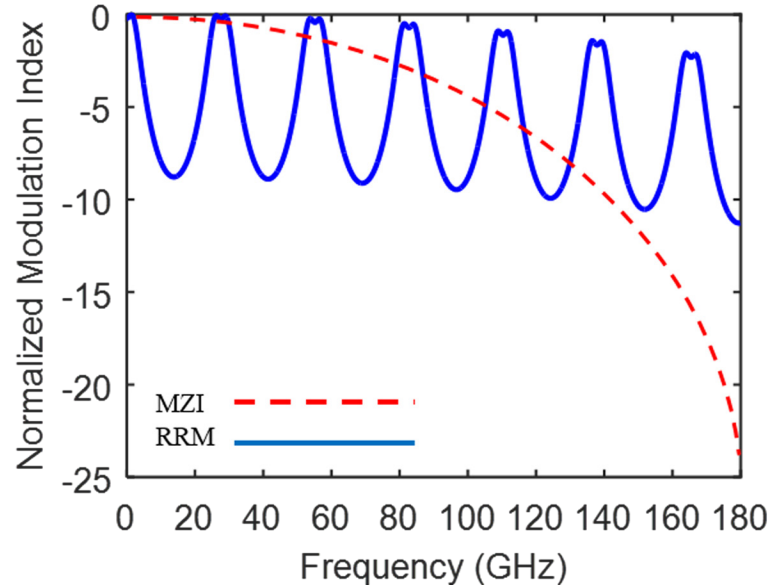


Figure 2-3 Normalized modulation index of MZI modulator versus RRM considering velocity mismatch factor of $\Delta n = 0.1$ in electro-optic polymer modulators.

Another main drawback of MZI modulator is its nonlinearity originated from sinusoidal transfer function limiting MPL SFDR [27]. Improving the MZI modulator linearity has been one of prominent targets in the last two decades and various types of linearization techniques have been proposed [42-47, 49, 52, 77-101]. A basic method to alter SFDR of MZI modulator is to adjust bias voltage [42-47, 52, 82]. The most common bias voltage is the quadrature point ($V_\pi/2$) where the second harmonic distortion is minimized and the third order harmonic distortion is maximized limiting SFDR [49]. If the application required bandwidth is sub-octave then one method to increase the SFDR, which is also accompanied by decreasing the noise level, is to bias the modulator away from quadrature point. However by moving away from quadrature bias point the fundamental signal is also suppressed causing the g_{MPL} degradation. To improve SFDR through the distortion

cancellation in optical domain several approaches have been pursued including parallel MZI [46, 49, 83-85], series MZI [86-88], dual-wavelength [102], and dual-polarization [89, 91]. Another category is to utilize a ring resonator to increase linearity of sinusoidal transfer function [79-81, 97-101]. In this approach a ring resonator is coupled to one or both arms of MZI using nonlinear phase response of ring to improve the linearity of the transfer function.

While proposed methods show SFDR improvements in theoretical analysis there are a few experimental demonstrations because of structures complexity in fabrication and implementation. Proposed linearization methods for the MZI modulator inherit sinusoidal transfer function, required size, and power requirements from MZI structure. MZI modulator is known for its robust and reliable operation however linearization techniques cause MZI modulator to be sensitive to structure properties and implementing conditions. For instance ring assisted MZI modulators limit the bandwidth and are sensitive to the loss factor of ring and coupling coefficient [81, 99].

2.4 Ring resonator modulators (RRM)

Electro-optic modulator applications of ring resonator structures named as ring resonator modulators (RRM) offer potentials for low power consumption, high modulation index, small foot-print [73, 103]. In addition ring resonator structures have become potential building blocks of integrated photonic devices for various applications such as optical filters [104-106], switches [107, 108], lasers [109, 110], and sensors [111, 112].

A general schematic of ring resonator structure is shown in Figure 2-4(a) where a circular ring waveguide is coupled to a base waveguide [113, 114]. The waveguide and the ring are located close enough to each other that power transfer can take place between them in the coupling region where a portion of propagating light-wave inside straight path is coupled to the ring waveguide and vice versa. When the wave inside the ring has a roundtrip phase shift for 2π times an integer number the wave propagating around the looped path interferes

constructively leading to the ring resonance state which builds up high intensity field inside the ring. While ring waveguide is in the vicinity of resonance mode the wave passing through the straight waveguide is suppressed due to the destructive interference between intensified field inside ring waveguide and straight waveguide as shown in Figure 2-4(b). The level of field suppression inside the straight waveguide and methods to control suppression level is the essential property that introduced ring resonator structures for various applications from filtering to modulating [104-112, 115-117].

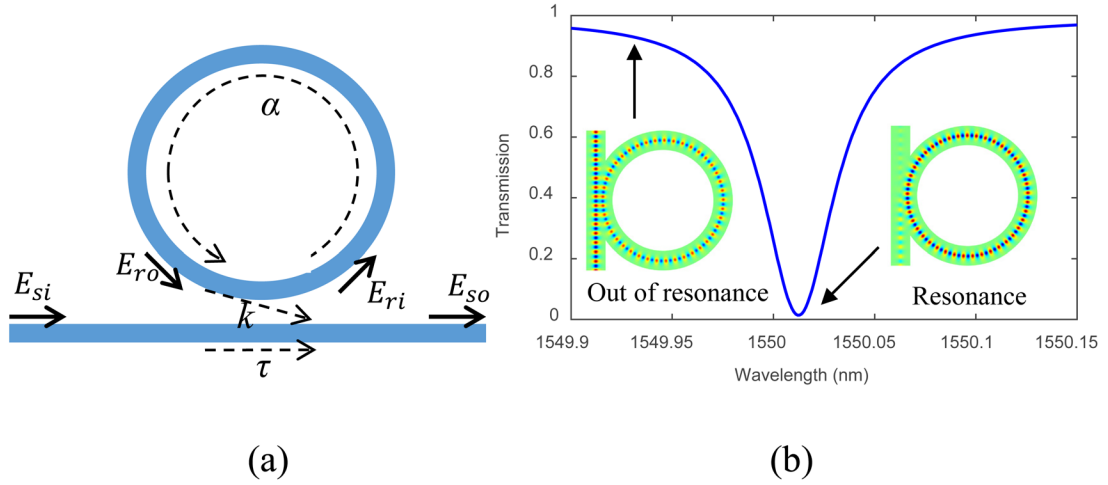


Figure 2-4 (a) A basic schematic of ring resonator structures, (b) Ring resonator structure transmission versus operating wavelength. Inside field profiled show light-wave propagations in resonance and out-of-resonance states.

In RRM the effective index of propagation mode inside the ring waveguide is controlled by applying voltage to the electrodes as shown in Figure 2-5. As the result the resonance frequency of ring resonator is altered which changes the filtering passband frequency yielding the optical transmission change in the shape of Lorentzian transfer function as shown in Figure 2-5(b).

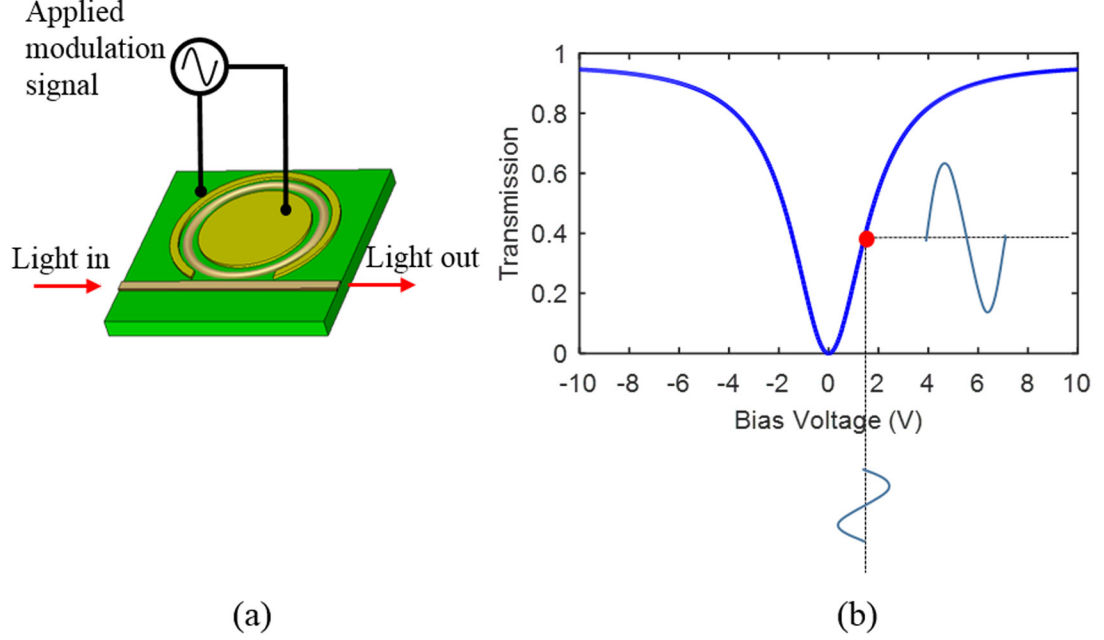


Figure 2-5 (a) general schematic of intensity RRM, (b) Lorentzian transfer function of RRM.

The ring resonator transfer function is derived theoretically by describing the relation between electromagnetic waves in the straight waveguide before and after coupling region according to Equation (2.3) where E_{si} and E_{so} are normalized mode amplitudes at the input and output of straight waveguide respectively as noted in Figure 2-4(a) [118]. The optical power exchange process between ring and base waveguide is considered to be lossless, meaning the total power entering and exiting the coupling region are equal. In addition single mode, unidirectional, and one polarization is excited inside ring resonator.

$$\begin{pmatrix} E_{so} \\ E_{ri} \end{pmatrix} = \begin{pmatrix} \tau & \kappa \\ \kappa^* & -\tau^* \end{pmatrix} \begin{pmatrix} E_{si} \\ E_{ro} \end{pmatrix} \quad (2.3)$$

The mode amplitude excited inside the ring before circulating the ring is E_{ri} and after one round trip is E_{ro} . The coupling coefficient in the straight waveguide is τ and κ is the coupling coefficient from ring to straight waveguide. The * is for conjugated complex

values of τ and κ . Since the coupling condition is lossless leading a unitary coupling matrix the relation between τ and κ is defined according to Equation (2.4).

$$|\tau|^2 + |\kappa|^2 = 1 \quad (2.4)$$

The relation between E_{ri} and E_{ro} is defined according to the loss factor of ring (α) and the round trip phase shift (θ) according to Equation (2.5).

$$E_{ro} = \alpha e^{i\theta} E_{ri} \quad (2.5)$$

θ is related to the physical ring circumference (L) and the propagation constant of wave (β) according to Equation (2.6) where n_0 is the effective refractive index of the light-wave mode propagating inside the ring, λ is the wavelength of light, and r is the radius of ring.

$$\theta = \beta L = \frac{n_0 4\pi^2 r}{\lambda} \quad (2.6)$$

The transfer function of ring resonator is derived as Equation (2.7) using Equations (2.3) to (2.6) [119]. Equation 2.7 is an essential equation in analyzing ring resonator structure showing that the transmission can be controlled by the phase shift factor of ring defined by θ and coupling conditions determined by α and τ . While maximum suppression of transmission factor happens at the exact resonance frequency in order to reach zero transmission coefficient at the resonance frequency a coupling condition $\alpha = \tau$, which is named as critical coupling condition, needs to be satisfied [119, 120].

$$\left| \frac{E_{so}}{E_{si}} \right|^2 = \frac{\alpha^2 + |\tau|^2 - 2\alpha|\tau|\cos\theta}{1 + \alpha^2|\tau|^2 - 2\alpha|\tau|\cos\theta} \quad (2.7)$$

The ring resonator transfer function is periodic in frequency since the phase shift factor (θ) is periodic and the ring resonator resonance repeats in frequency as shown in Figure 2-6. The wavelength difference between two successive resonance states is called Free Spectral Range (FSR) [113]. The periodic Lorentzian resonance characteristic of RRM yields enhanced modulation index compared to MZI modulators in a limited bandwidth around

the resonance frequency as shown in Figure 2-3. The modulation index enhancement of a RRM is dependent to the Q-factor of the resonator. The higher Q-factor results in higher modulation index enhancement because of steeper Lorentzian transfer function and small change of applied voltage produce large resonance frequency shift. The RRM advantage of enhanced modulation index mitigates the RF electrode loss and phase velocity mismatch factors in the modulation index degradation at high frequencies that commonly perturb MZI operation [73, 103]. Due to the enhanced modulation index functional RRM has been reported to be operated at multiples of the FSR, up to 165 GHz fabricated by electro-optic polymer material [73].

The resonance characteristic of RRM dictates limited operational bandwidth around resonance frequency. The operational bandwidth is related to the resonance Q-factor as the operational bandwidth gets narrower when Q-factor gets higher [121]. The RRM operational bandwidth imposes frequency dependent MPL figure-of-merits determining MPL operational bandwidth. So far effects of RRM resonance bandwidth have been studied on the modulation index defining bandwidths for g_{MPL} and NF [121]. However RRM bandwidth in terms of linearity and SFDR has not been addressed yet.

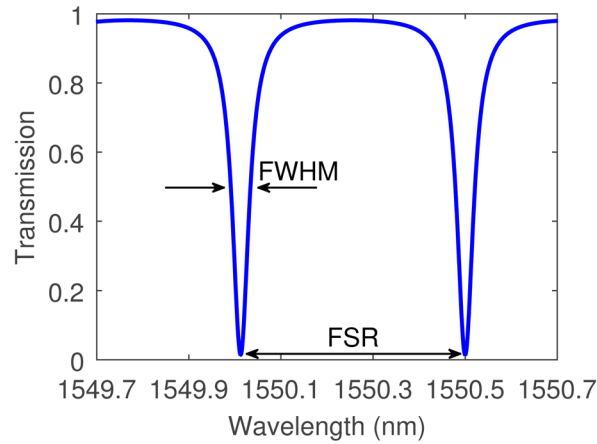


Figure 2-6 Periodic transmission coefficient of ring resonator in frequency domain.

Despite promising features of RRM for MPLs, there are limited studies on RRM functionalities in MPLs [73, 103, 122-124]. While initial studies have shown that RRM is capable of providing higher SFDR versus MZI modulator [122, 125], which can be a notable advantage in advancing MPLs the limits and applicability of this advantage has not been fully investigated. A rigorous theoretical approach is developed to analyze RRM linearity incorporated in MPLs proving that RRM can provide higher SFDR compared to MZI modulator as described in Chapter 3. However it is shown that superior performance of RRM is not sustainable in a wide bandwidth and the bandwidth limitation due to linearity is more severe than previously defined bandwidths according to the modulation index based on resonance linewidth [121]. Possible methods to improve operational bandwidth of RRM are discussed in Chapter 3 and it is shown RRM is an appealing choice for applications in need of high frequency operations > 50 GHz while in a limited bandwidth (a few GHz). One of these applications can be RoF implementation for wireless access networks in 57-64 GHz frequency range to feed multi-Gb/s data rates to the large number of wireless access points for network architectures featuring significantly smaller cell sizes (pico-cells) [9, 24-26].

Chapter 3: Nonlinearity Analysis of a Ring Resonator Modulator

While RRM can be a promising alternative for MPLs the linearity of RRM has not been fully investigated. To analyze a RRM two models namely static [119] and dynamic models [120] have been developed. The static model is limited in characterizing frequency response of RRM due to the resonance nature of RRM [120]. To capture a full frequency behavior of RRM the dynamic model is required. The dynamic model has been addressed for modulation index of RRM [73, 126] however the linearity of RRM has been mostly limited to the static model [124, 125].

Static and dynamic models are reviewed for RRM and a rigorous analytical method originated from dynamic method is developed to analyze linearity of RRM. The higher SFDR in RRM versus MZI modulator is examined showing operational bandwidth limits of the RRM SFDR. It is shown that the linearity of RRM imposes stricter limits on operational bandwidths than previously presented based on the modulation index of RRM [121]. The practical implementation conditions of RRM SFDR is studied in terms of noise bandwidth and ring-waveguide coupling conditions. A novel method of bias voltage adjustment is proposed and analyzed to improve the SFDR of RRM according to the noise bandwidth and ring-waveguide coupling conditions. RRM is shown to be promising for applications with relatively narrow bandwidth (a few GHz) while operating in high operational frequency (millimeter-wave) such as high speed wireless access networks.

3.1 Static analysis

The RRM transfer function in the steady-state is similar to Equation (2.7) however the round trip phase shift (θ) is altered by the applied voltage as formulated in Equation (3.1) [73]

$$\theta = \beta L + \frac{\pi n_0^3 r \Gamma V_{dc}}{\lambda g} L \quad (3.1)$$

where n_0 is the effective refractive index of the propagating mode, L is the perimeter of the ring, r is the electro-optic coefficient of material, V_{dc} is the bias voltage, λ is the optical wavelength, Γ is the electrical-optical overlap integral, and g is the electrode gap.

The RRM in steady-state represents a transfer function of Lorentzian type (transmission versus applied DC voltage) as shown in Figure 3-1. Characteristics of the RRM transfer function depend on the coupling condition between ring and base waveguide defined by α and τ . The critical coupling condition ($\alpha = \tau$) yields maximum resonance extinction ratio providing maximum range of operation at the slopes of Lorentzian transfer function. The resonance bandwidth and modulation index are controlled by critical coupling condition number and ring radius as shown in Figure 3-2. The resonance bandwidth narrows by increasing the critical coupling condition number or ring radius. However narrower resonance bandwidth yields higher slope of transfer function improving MPL gain and noise figure. There is always a trade-off between resonance bandwidth and modulation index and resonance structure is designed according to system level figure-of-merits requirements.

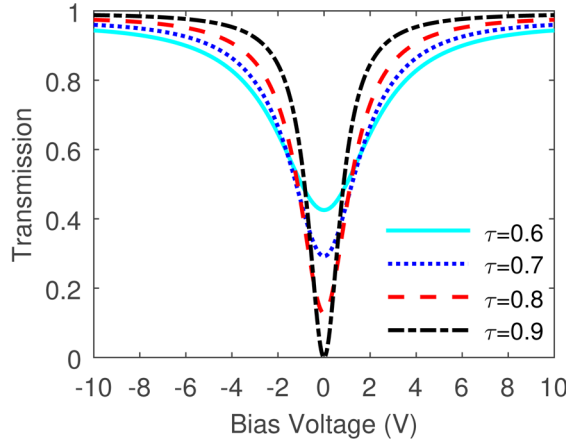


Figure 3-1 RRM transfer function versus coupling condition changes.

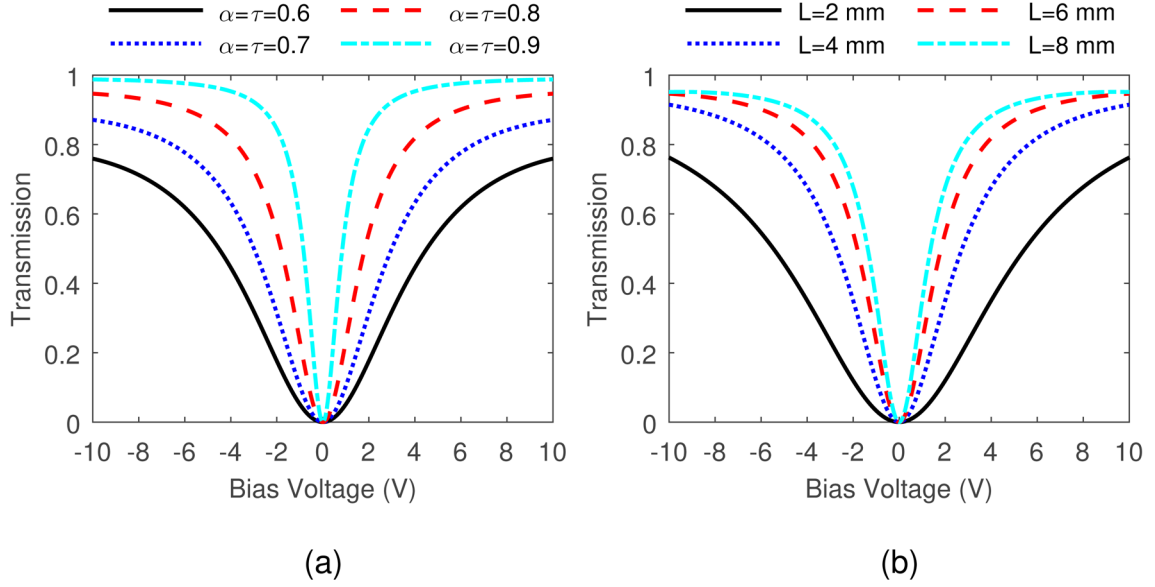


Figure 3-2 RRM transfer function changes versus (a) critical coupling conditions, and (b) ring perimeter size (L).

To analyze nonlinearity using steady-state method, the transfer function is expanded in Taylor series around the specific point of bias voltage (V_{dc}) according to Equation (3.2). The transfer function of the modulator is $Y(v)$ where v represents the time varying function which is the applied RF signal to the modulator and a_k are the expansion coefficients.

$$\begin{aligned}
 Y(v) &= \sum_{k=0}^{\infty} \frac{(v - V_{dc})^k}{k!} \left(\frac{d^k Y}{dv^k} \right)_{v=V_{dc}} \\
 &= \sum_{k=0}^{\infty} a_k (v - V_{dc})^k
 \end{aligned} \tag{3.2}$$

In order to drive the modulator nonlinearity and eventually the SFDR of MPL from the Taylor expansion the common method of single-tone and two-tone test is applied [27]. By applying a single-tone signal in the general form of $v(t) = V_{dc} + A \cos(\omega t)$, where A is the signal amplitude and ω is the angular modulating frequency, to Equation (3.2) and driving the Taylor series coefficients the output signal can be represented as the summation of signals in harmonic frequencies as presented in Equation (3.3).

$$\begin{aligned}
Y(t) \approx & a_0 + \frac{1}{2}a_2A^2 + \left(a_1A + \frac{3}{4}a_3A^3\right)\cos(\omega t) \\
& + \frac{1}{2}a_2A^2\cos(2\omega t) + \frac{1}{4}a_3A^3\cos(3\omega t), \dots
\end{aligned} \tag{3.3}$$

To extract intermodulation distortions the two-tone signal in the form of Equation (3.4) is applied to the Taylor series of modulator transfer function. Using trigonometric functions as shown in Equation (3.5) the output signal can be obtained as shown in Equation(3.6).

$$v(t) = V_{dc} + A[\cos(\omega_1 t) + \cos(\omega_2 t)] \tag{3.4}$$

$$\begin{aligned}
2\cos(\theta)\cos(\varphi) &= \cos(\theta - \varphi) + \cos(\theta + \varphi) \\
2\sin(\theta)\cos(\varphi) &= \sin(\theta + \varphi) + \sin(\theta - \varphi) \\
2\sin(\theta)\sin(\varphi) &= \cos(\theta - \varphi) - \cos(\theta + \varphi) \\
2\cos(\theta)\sin(\varphi) &= \sin(\theta + \varphi) - \sin(\theta - \varphi)
\end{aligned} \tag{3.5}$$

$$\begin{aligned}
Y(t) \approx & a_0 + a_2A^2 \\
& + \left(a_1A + \frac{9}{4}a_3A^3\right)(\cos(\omega_1 t) + \cos(\omega_2 t)) \\
& + \frac{1}{2}a_2A^2(\cos(2\omega_1 t) + \cos(2\omega_2 t)) \\
& + \frac{1}{4}a_3A^3(\cos(3\omega_1 t) + \cos(3\omega_2 t)) \\
& + a_2A^2[\cos((\omega_1 - \omega_2)t) + \cos((\omega_1 + \omega_2)t)] \\
& + \frac{3}{4}a_3A^3[\cos((2\omega_1 - \omega_2)t) + \cos((2\omega_1 + \omega_2)t) \\
& \quad + \cos((2\omega_2 - \omega_1)t) + \cos((2\omega_2 + \omega_1)t)]
\end{aligned} \tag{3.6}$$

As seen in Equation (3.6) besides harmonic distortions the output signal consists of other components with frequencies resulted from linear combinations of two input frequencies. It can be shown that IMD3 distortion power can be expanded to the linear mixing of amplitudes in odd harmonics starting from 3rd harmonic utilizing multinomial theorem as

shown in Equation (3.7) where (a_3, a_5, a_7, \dots) are Taylor series expansion coefficients [127]. Equation (3.7) shows that the third harmonic distortion has the highest contribution in forming the output power at IMD3 distortion. Therefore one type of efforts to improve SFDR in sub-octave applications have been devoted to suppress third order harmonic distortion.

$$E_{out}^{IMD3} = \frac{3}{4}a_3V_m^3 + \frac{25}{8}a_5V_m^5 + \frac{735}{64}a_7V_m^7 + \dots \quad (3.7)$$

The static method can be modeled using computational software to obtain MPL figure-of-merits and is a sufficient approach when the modulator response is not highly frequency dependent. The static model is commonly utilized for MZI modulators [27] however the RRM function is highly frequency dependent due to the resonance characteristics. The frequency dependency of RRM is intensified when traveling-wave electrodes are utilized where the velocity-mismatch and electrode loss factors need to be taken into account. While the static model has been utilized to model RRM's linearity [124, 125], it is shown in the Section 3.2 that the nonlinearity in RRM's is highly dependent on the frequency and the static model is not capable for full analyzing of RRM especially in terms of nonlinearity and link SFDR.

3.2 Dynamic analysis

The dynamic transfer function shown in Equation (3.8) is based on the multiple round-trip approach where the optical wave inside the ring is modeled by refractive index modulation of ring resonator and summation of modulation effects of round-trips [73, 103, 120].

$$\left| \frac{E_{out}(t)}{E_{in}(t)} \right|^2 = \left[\tau - (1 - \tau^2) \sum_{n=1}^{\infty} \tau^{n-1} \alpha^n \times e^{-i(n\theta + \delta_n \sin(\omega_m t - n\varphi))} \right]^2 \quad (3.8)$$

In Equation (3.8) ω_m is the operating microwave angular frequency, t is the time, and n is the number of times the beam propagates inside the ring. $\varphi = \omega_m / FSR$ where FSR is

defined by $c/(n_0L)$ (c is the speed of light in free space, n_0 is the effective refractive index of the propagating mode and L is the perimeter of the ring). The round trip phase shift (θ) due to the steady state refractive index of the ring and applied DC bias voltage is defined in Equation (3.1). The modulation index is δ_n which depends on the electrode type (lumped or travelling-wave) used in the modulator. In the case of lumped electrode with an applied microwave signal in the form of $V(t) = V_m \sin(\omega_m t)$ the δ_n is given by Equation (3.9) [60]. It is assumed that all parts of active waveguide in the modulator, for example the ring waveguide in case of RRM, experience equal refractive index change at time corresponding to the applied RF voltage.

$$\delta_n \sin(\omega_m t - n\varphi) = \frac{\pi n_0^3 r \Gamma V_m}{\lambda g} L \times \frac{\sin\left(\frac{n\varphi}{2}\right)}{\left(\frac{\varphi}{2}\right)} \times \sin\left(\omega_m t - \frac{n\varphi}{2}\right) \quad (3.9)$$

In traveling-wave type electrodes the RF-wave travels along the ring waveguide and depending on the electrode loss and velocity of the RF-wave the optical-wave experience different refractive index modulation related to the RF-wave intensity. Therefore optical field at time (t) and length of propagation in electrode region (x) experiences a voltage in the form of Equation (3.10) [128]

$$V(x, t) = V_m e^{-\alpha_m L} \sin\left(\omega_m t - \frac{\Delta n}{c} x\right) \quad (3.10)$$

where α_m is the microwave electrode loss factor, Δn is the electro-optic material refractive index difference in optical and microwave frequencies, and L is the length of electrodes which in the case of ring resonator modulator it is assumed to be equal to the ring perimeter. δ_n for traveling-wave electrodes can be derived as Equation (3.11) where $\psi = \omega_m \Delta n L / c$ is the velocity mismatch factor [73].

$$\begin{aligned}
\delta_n \sin(\omega_m t - n\varphi) &= \frac{\pi n_0^3 r \Gamma V_m}{\lambda g} L \frac{e^{-\alpha_m L}}{\psi^2 + L^2 \alpha_m^2} \frac{\sin\left(\frac{n\varphi}{2}\right)}{\sin\left(\frac{\varphi}{2}\right)} \\
&\times \left[\psi \left\{ \cos\left(\omega_m t - \frac{(n+1)\varphi}{2} - \psi\right) - e^{\alpha_m L} \cos\left(\omega_m t - \frac{(n+1)\varphi}{2}\right) \right\} \right. \\
&\left. - \alpha_m L \left\{ \sin\left(\omega_m t - \frac{(n+1)\varphi}{2} - \psi\right) - e^{\alpha_m L} \sin\left(\omega_m t - \frac{(n+1)\varphi}{2}\right) \right\} \right] \quad (3.11)
\end{aligned}$$

Equations (3.8)-(3.11) are utilized to model RRM in a MPL extracting link figure of merits. To calculate SFDR the two-tone test and numerical Fourier method is utilized [27] and the RF input power is swept in a range to identify two RF input power levels, which bring fundamental signal and distortion powers to the noise level. A typical set of MPL parameters as presented in Table 3-1 [49] is used for modeling. In addition utilized parameters to model electro-optic polymer modulators are shown in the Table 3-2 [129].

Table 3-1 MPL parameters used in the calculations

Parameter	Value
Laser power	0.1 W
Laser wavelength	1.55 μm
Laser RIN	-165 dB/Hz
Modulator transmission	-10 dB
Detector responsivity	0.7 A/W
Modulator load resistance	50 Ω
Detector load resistance	50 Ω
Noise Bandwidth	1 Hz

Table 3-2 Polymer modulator parameters

Parameter	Value
Electrode gap (g)	10 μm
Electrical-optical overlap (Γ)	1
Effective refractive index (n_0)	1.60
Polymer EO coefficient (r)	36 pm/V

It should be noted that the RRM nonlinearity discussed here is the result of RRM structure itself therefore the analysis can be generalized to RRM on other type of material platforms

such as LiNbO₃. However it should be stressed that the effect of material on modulator linearity needs to be considered for material platforms such as silicon where the material effects is not negligible [123, 124]. Moreover link parameters selections do not limit the generality of study conducted in this research since the MZI modulator is used in the same link parameters for comparison.

3.3 Harmonic distortions

To analyze nonlinearity of RRM, an analytical method is developed based on a dynamic transfer function. Harmonic distortions are derived from the dynamic transfer function by expanding the $\exp(-j(n\theta + \delta_n \sin(\omega_m t - n\varphi)))$ part of Equation (3.8) to harmonic frequencies. The exponential part is reformed as Equation (3.12) and then derived as presented in Equation (3.13) by utilizing Bessel functions equivalent of trigonometric functions as shown in Equation (3.14) and Equation(3.15).

$$\begin{aligned}
 & \exp(-j(n\theta + \delta_n \sin(\omega_m t))) \\
 &= \exp(-jn\theta) \times \exp(-j\delta_n \sin(\omega_m t)) \\
 &= \exp(-jn\theta) \times [\cos(\delta_n \sin(\omega_m t)) - j \sin(\delta_n \sin(\omega_m t))]
 \end{aligned} \tag{3.12}$$

$$\cos(\delta_n \sin(\omega_m t)) - j \sin(\delta_n \sin(\omega_m t)) = \begin{cases} J_0(\delta_n) \\ -j2J_1(\delta_n) \sin(\omega_m t) \\ +2J_2(\delta_n) \cos(2\omega_m t) \\ -j2J_3(\delta_n) \sin(3\omega_m t) \\ \dots \end{cases} \tag{3.13}$$

$$\begin{aligned}\cos(x \sin(y)) &= J_0(x) + 2 \sum_{h=1}^{\infty} J_{2h}(x) \cos(2hy) \\ \sin(x \sin(y)) &= 2 \sum_{h=0}^{\infty} J_{2h+1}(x) \sin((2h+1)y)\end{aligned}\tag{3.14}$$

$$\begin{aligned}\cos(x \sin(y)) &= J_0(x) + 2 \sum_{h=1}^{\infty} J_{2h}(x) \cos(2hy) \\ \sin(x \sin(y)) &= 2 \sum_{h=0}^{\infty} J_{2h+1}(x) \sin((2h+1)y)\end{aligned}\tag{3.15}$$

According to the harmonics in Equation (3.13), a pattern is extracted where the exponential function is derived as Equation (3.16) for odd harmonics ($h = 1, 3 \dots$) and Equation (3.17) for even harmonics ($h = 2, 4 \dots$).

$$\begin{aligned}\exp(-jn\theta) \times (-j) 2J_h(\delta_n) \sin(h\omega_m t) \\ = -\sin(n\theta) 2J_h(\delta_n) \sin(h\omega_m t) - j \cos(n\theta) 2J_h(\delta_n) \sin(h\omega_m t)\end{aligned}\tag{3.16}$$

$$\begin{aligned}\exp(-jn\theta) \times 2J_h(\delta_n) \cos(h\omega_m t) \\ = \cos(n\theta) 2J_h(\delta_n) \cos(h\omega_m t) - j \sin(n\theta) 2J_h(\delta_n) \cos(h\omega_m t)\end{aligned}\tag{3.17}$$

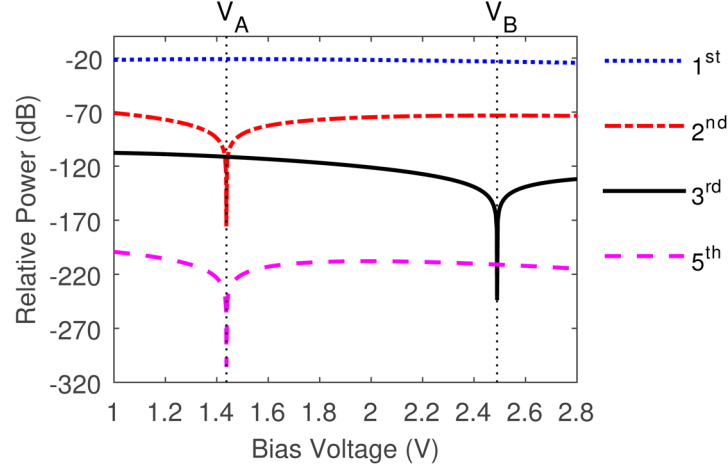
By substituting above equations in Equation (3.8) and considering lumped electrode for the modulator as shown in Equation (3.9) following relations can be derived for output powers at even and odd harmonics:

$$\begin{aligned}\left| \frac{E_{out}(t)}{E_{in}(t)} \right|_{odd}^2 &= \left| \tau - (1 - \tau^2) \sum_{n=1}^{\infty} \tau^{n-1} \alpha^n \right. \\ &\quad \times \left[-\sin(n\theta) 2J_h(\delta_n) \sin\left(h\omega_m t - \frac{hn\varphi}{2}\right) \right. \\ &\quad \left. \left. - j \cos(n\theta) 2J_h(\delta_n) \sin\left(h\omega_m t - \frac{hn\varphi}{2}\right) \right] \right|^2\end{aligned}\tag{3.18}$$

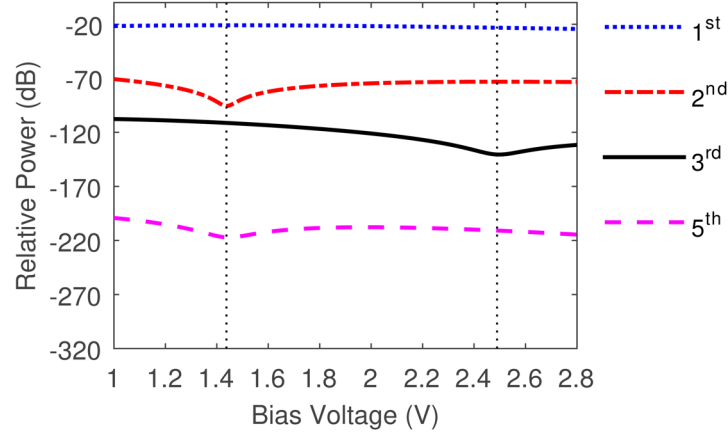
$$\begin{aligned}
\left| \frac{E_{out}(t)}{E_{in}(t)} \right|_{even}^2 &= \left| \tau - (1 - \tau^2) \sum_{n=1}^{\infty} \tau^{n-1} \alpha^n \right. \\
&\quad \times \left[\cos(n\theta) 2J_h(\delta_n) \cos\left(h\omega_m t - \frac{hn\phi}{2}\right) \right. \\
&\quad \left. \left. - j \sin(n\theta) 2J_h(\delta_n) \cos\left(h\omega_m t - \frac{hn\phi}{2}\right) \right] \right|^2
\end{aligned} \tag{3.19}$$

3.4 SFDR and operational bandwidth

Using Equations (3.18) and (3.19), output powers for fundamental, second, third, and fifth harmonics are calculated in the range of bias voltages and in 1 Hz and 50 MHz frequencies as presented in Figure 3-3. Two critical bias voltages are well noticed (V_A and V_B) at 1 Hz operating frequency as shown in Figure 3-3(a). At bias point V_A , second and fifth harmonics are suppressed while at V_B , the third harmonic is suppressed. The Lorentzian-shaped transfer function of RRM has a bias point where the output power in third harmonic is minimum while the fundamental signal has considerable amount of power, resulting in higher SFDR compared to MZI modulators. Therefore, V_B is the optimum bias for the RRM to obtain high SFDR in terms of IMD3. However, by increasing the RF operating frequency from 1 Hz to 50 MHz the suppressing of the harmonics at V_A and V_B is diminished considerably as shown in Figure 3-3(b).



(a)



(b)

Figure 3-3 Normalized output intensities in fundamental, second-harmonic, third-harmonic and fifth-harmonic frequencies versus bias voltages in (a) 1 Hz, and (b) 50 MHz operating frequencies. Results are for input RF power of -20 dBm and a ring resonator with 6 mm perimeter. Output intensity is in logarithmic scale and normalized versus input RF power.

According to the results in Figure 3-3 it is expected that the RRM linearity diminishes considerably by increasing RF frequency which results in MPL SFDR degradation. To see the effect of RF frequency on SFDR, the MPL with RRM is modeled in 1 Hz and 50 MHz RF frequencies while biasing at V_B . As seen in Figure 3-4 at 1 Hz RF frequency the IMD3

power shows fifth order slope meaning third order harmonic cancellation which provides SFDR ($\sim 125 \text{ dB.Hz}^{4/5}$). However by increasing input RF frequency the IMD3 slope moves toward third order slope showing the third order harmonic cancellation is suppressed confirming the results presented by harmonic behaviors as shown in Figure 3-3.

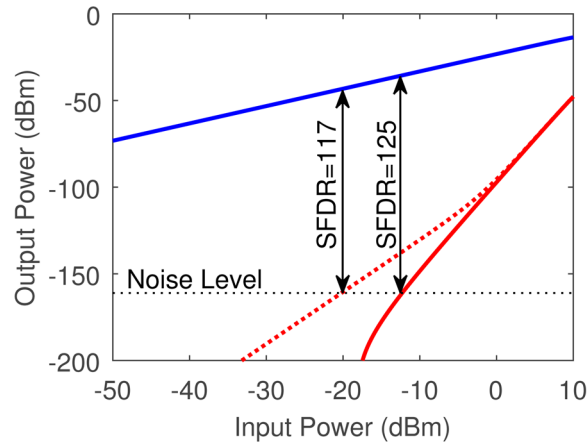


Figure 3-4 Output fundamental and IMD3 powers against the RF input power for RRM. Lines are the results for 1 Hz RF frequency and dots are for 50 MHz. Results are for 6 mm rings biased at V_B . Noise level is at ~ -164 dBm in 1 Hz bandwidth.

To obtain the frequency bandwidth of SFDR, Figure 3-5 presents the calculated SFDR for the RRM that is biased at V_B in the range of RF operating frequency up to 5 GHz. Results show that biasing the single RRM at V_B will provide relatively high SFDR at very narrow bandwidths versus MZI modulator. $\text{SFDR} > 120 \text{ dB}$ (1 Hz noise bandwidth) is obtained only in $\sim 20 \text{ MHz}$ operational frequency and SFDR drops below MZI level ($\sim 110 \text{ dB}$, 1 Hz noise bandwidth) in $\sim 720 \text{ MHz}$ operational frequency.

Obtained results show that bandwidth limitation dictated by RRM on MPL applications due to the SFDR is more severe than bandwidth limitations due to the modulation index presented before [121]. For instance, the 3-dB modulation index bandwidth of the same RRM is 1.6 GHz using Equation (2.16). However in $\sim 1440 \text{ MHz}$ RRM SFDR drops below MZI eliminating one of main advantages of RRM. The modulation index directly impacts MPL gain and noise figure and bandwidth of modulation index is translated to the

bandwidth of link gain and noise figure. Therefore linearity of RRM defines the operational bandwidth of RRM which is in contrary with previously discussed in the literature where bandwidth of RRM has been calculated based on modulation index [121]. Optical resonance linewidth is the limiting factor in the modulator operational frequency bandwidth affecting modulation index [130] and linearity [131]. The frequency dependent linearity and thus the SFDR of MPL limits the operational bandwidth more than the modulation index frequency bandwidth [131]. Thus in order to advance RRM for a wide range of MPL applications it is necessary to investigate ways to increase the SFDR at wider bandwidths (Chapter 4).

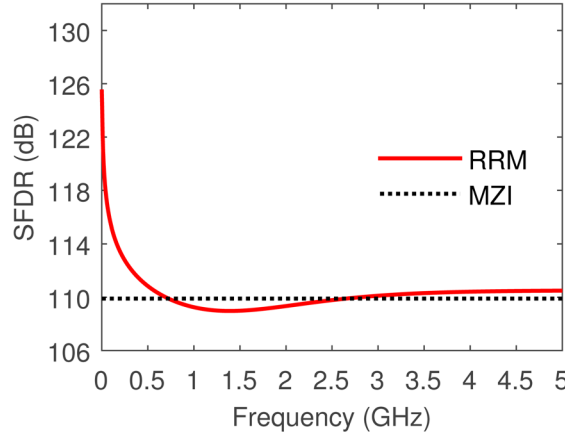


Figure 3-5 SFDR versus RF operating frequency for RRM, and MZI. SFDR is calculated for 1 Hz noise bandwidth. RRM is biased at V_B .

3.5 Noise bandwidth effects on SFDR

In determining the SFDR of a MPL the noise bandwidth requirement by a targeted application has a crucial role because of direct impact of noise bandwidth on the noise level defining the maximum and minimum RF powers that can be transmitted or processed by the link [27].

Although RRM can provide ~15 dB improvement versus MZI modulator at 1 Hz noise bandwidth, the more noise bandwidth increases towards higher bandwidths the RRM is

less effective in keeping the SFDR advantage versus MZI modulator according to Equation (1.4) due to the IMD3 power slope of five versus RF input power. For instance at 500 MHz noise bandwidth RRM offers SFDR ~ 55.6 dB versus ~ 51.9 dB obtained from MZI modulator yielding just ~ 3.7 dB improvement.

A new bias voltage adjustment method is proposed to improve the SFDR of RRM for MPL noise bandwidth requirements. Figure 3-6(a) shows that IMD3 output power is cancelled at a single RF input power yielding a null point in output IMD3 power versus RF input power as shown by P_A . The slope of IMD3 power to the right of P_A is five showing the complete third order harmonic cancellation while the slope on the left of P_A is three showing third harmonic contribution in IMD3. In order to have constant slope of five in the whole interest range of RF input power the null point needs to happen below the intersection of noise level and IMD3 power as shown in Figure 3-6(a). In this case SFDR for other instantaneous bandwidths can be calculated using Equation (1.4). However it is shown here that the SFDR can be improved further by shifting the null point to the vicinity of noise level. The null point of IMD3 power (P_A) can be optimized by adjusting bias voltage as shown in Figure 3-6(b) and Figure 3-6(c) for 1 Hz and 500 MHz instantaneous bandwidths respectively. As seen at the vicinity of the IMD3 null point IMD3 power becomes less than fifth order intermodulation distortion (IMD5) power showing the need of IMD5 power consideration for the accurate SFDR calculation. By moving bias voltage from 2.409 to 2.412 the SFDR is improved from 125.2 dB to 127.9 dB in 1 Hz instantaneous bandwidth. Adjusting the bias voltage is more beneficial in maximizing the SFDR for higher noise bandwidths where the RRM advantage margin is narrower. By biasing the RRM at 2.6 (V) the P_A point is optimized according to the noise level at 500 MHz noise bandwidth as shown in Figure 3-6(c) yielding SFDR ~ 57.7 dB. With this bias voltage adjustment method the superiority margin of SFDR from RRM versus MZI modulator is increased from 3.7 dB to 5.8 dB. To analyze the bias voltage influence on SFDR at higher instantaneous bandwidths SFDR is calculated in the range of bias voltages at 10 MHz and 500 MHz noise bandwidths as shown in Figure 3-7. Results show that

depending on the required system level noise bandwidth the bias voltage of RRM can be adjusted to maximize the SFDR for the desired noise bandwidth. Increasing noise bandwidth yields wider bias voltage range before SFDR sharp drops as seen in Figure 3-7 easing the bias controller required resolution. For instance at noise bandwidth of 10 MHz the RRM maintains 8.3 ± 0.1 dB SFDR margin versus MZI modulator considering ± 10 mV bias voltage tolerance, however, at 500 MHz the RRM maintains 5.6 ± 0.1 dB SFDR margin at ± 30 mV tolerance. It should be noted that the bias voltage controller is a necessary component for MZI modulators due to the bias drift phenomena and precise bias controller with a few mV resolution have been developed that can be utilized for RRM [132].

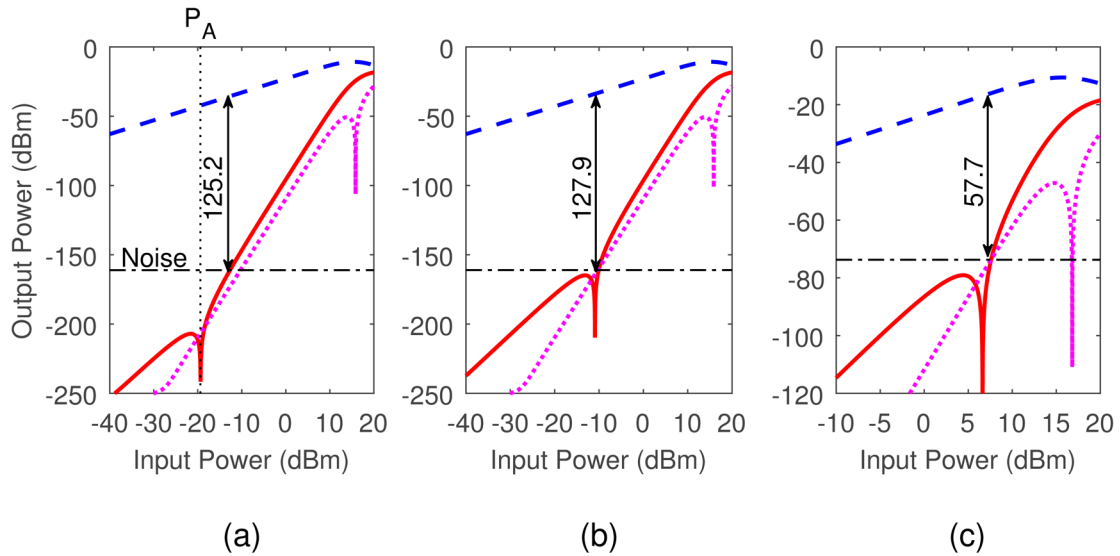


Figure 3-6 Output fundamental, IMD3, and IMD5 powers against the RF input power at three bias voltages, (a) bias voltage is 2.409 (V), and P_A is below noise level, (b) bias voltage is 2.412 (V), P_A is optimized to maximize SFDR for 1 Hz instantaneous bandwidth, (c) bias voltage is 2.6 (V), and P_A is optimized to maximize SFDR for 500 MHz instantaneous bandwidth. Results are for a ring with $L = 6.2$ mm and $\alpha = \tau = 0.8$.

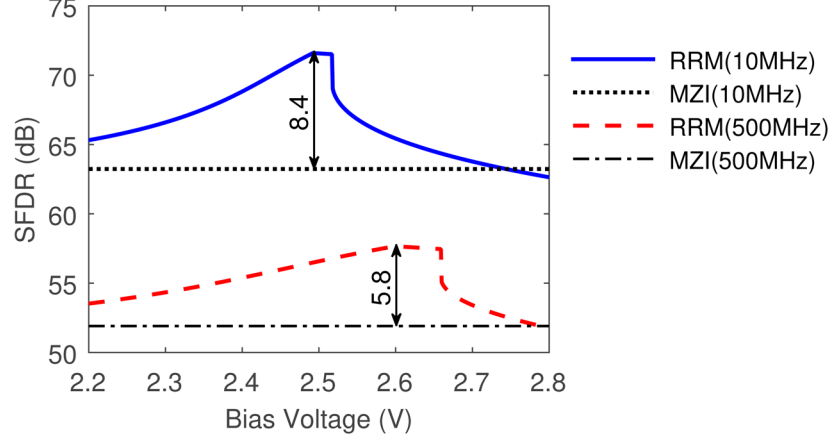
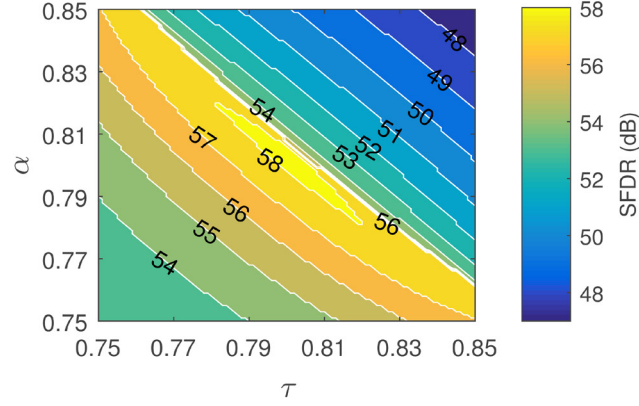


Figure 3-7 SFDR of RRM versus bias voltages at 10 MHz and 500 MHz instantaneous bandwidths in comparison with SFDR of MZI modulator.

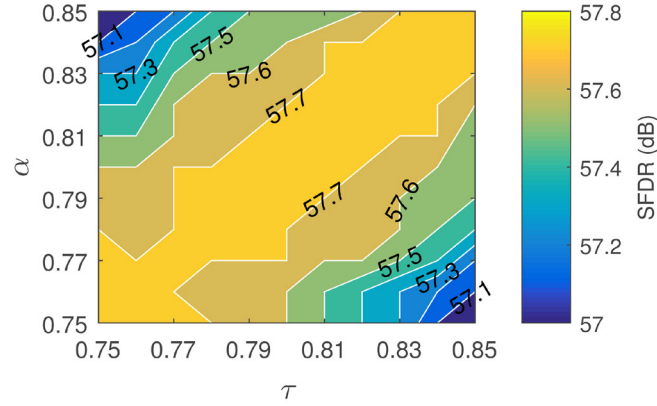
3.6 Ring-waveguide coupling condition tolerances

The RRM transfer function is sensitive to the coupling condition between ring and base waveguide as described in Section 2.4. To achieve desired critical coupling condition physical dimensions of the RRM need to be designed and optimized utilizing numerical electromagnetic methods. However achieving the exact designed coupling condition in fabrication is challenging and requires high precision fabrication steps. Small tolerance in RRM physical dimensions can move α and τ considerably away from desired critical coupling condition [133]. By considering ± 0.05 range of tolerance for α and τ around critical coupling condition $\alpha = \tau = 0.8$ the variation of SFDR versus α and τ tolerances is studied as seen in Figure 3-8(a). Results show dropping of SFDR as low as 46.7 dB (~ 5 dB less than MZI modulator) with just 0.05 tolerance in α and τ showing that RRM is highly vulnerable to lose its prominent advantage because of fabrication tolerances hindering RRM consideration as highly linear modulator. The solution proposed here is to adjust bias voltage according to the obtained α and τ from fabricated RRM. The optimum bias voltage to have maximum IMD3 power suppression is subjected to change by variations in α and τ . Therefore optimum bias voltage to maximize linearity of RRM needs to be adjusted in the application stage according to the fabricated α and τ values. Considering the capability

of bias voltage adjustment in 1 mV resolution the SFDR of RRM presented in Figure 3-8(a) is recalculated as shown in Figure 3-8(b). Results show with the bias voltage adjustment method the linear capability of RRM is restored keeping SFDR > 57 dB despite ± 0.05 tolerance in α and τ . The bias adjustment method can also be used with dynamic bias voltage controllers [132] in order to mitigate environmental and operational effects such as heat on RRM SFDR.



(a)



(b)

Figure 3-8 Contour plot of SFDR versus ring resonator modulator fabrication tolerances according to loss factor (α) and coupling coefficient (τ) tolerances around critical coupling condition at $\alpha = \tau = 0.8$. (a) bias voltage is kept fixed at 2.6 (V) for all α and τ values while (b) bias voltage is optimized according to each α and τ values.

3.7 Ring resonator modulator for radio-over-fiber applications

Despite narrow operational bandwidth of RRM due to the bandwidth of linearity, the RRM can be a promising choice for applications such as 60 GHz wireless access networks which are in need of high frequency operations while in a relatively narrow band. The RRM feasibility in terms of operational bandwidth is examined for RoF application of 60 GHz as shown in Figure 3-9. The 60 GHz wireless access networks will support frequency ranges from 57.240 GHz to 65.880 GHz according to the ratified IEEE 802.15.3c standard [134]. The allocated frequency range is divided into four channels with 2.15 GHz frequency bandwidth each. The RRM is for the channel from 59.40 GHz to 61.56 GHz with central frequency at 60.48 GHz.

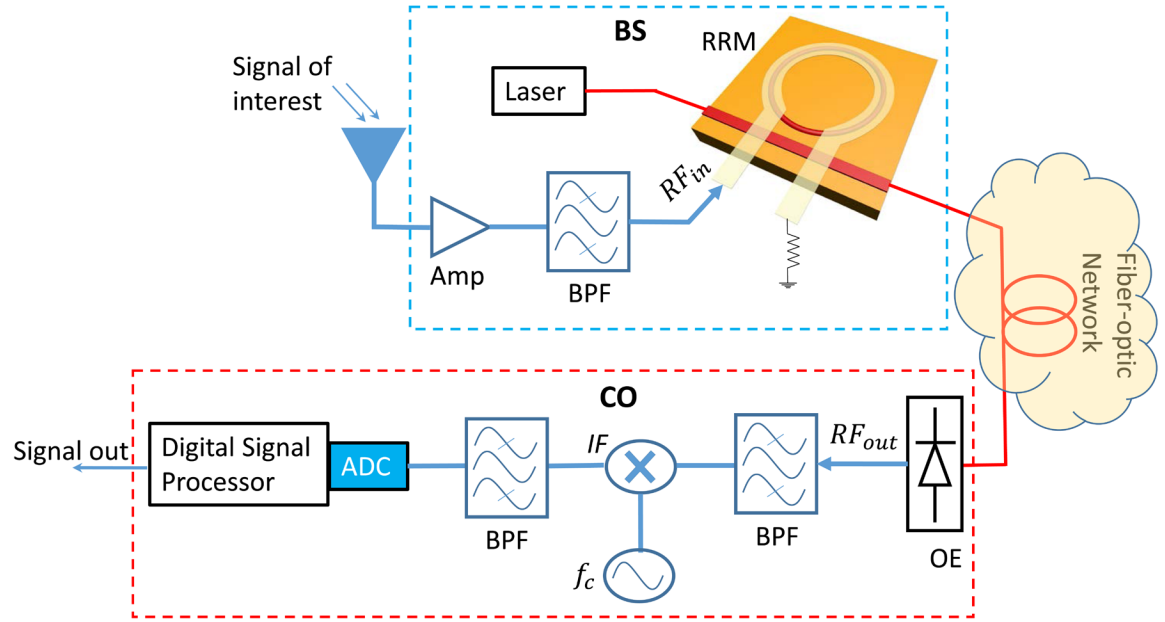


Figure 3-9 Fundamental setup of Radio-over-fiber signal transport using analog fiber optic links between antenna base-station (BS) and central office (CO). A ring resonator modulator (RRM) is shown as electro-optic modulator. Amp: amplifier, BPF: band-pass filter, RF_{in} : radio frequency signal applied to the RRM, OE: optical to electrical converter (photodetector), RF_{out} : radio frequency signal at the photodetector output, IF: intermediate frequency, ADC: analog to digital converter.

To design a RRM for a desired frequency band the resonance frequency is adjusted at a multiple of FSR located at the center of the desired spectrum. For a 60.48 GHz central frequency and according to the effective refractive index of the optical propagating mode ($n = 1.6$) the ring perimeter (L) can be 6.2 mm in order to have a FSR = 30.24 GHz and thus the central frequency of the frequency band is matched with $2 \times \text{FSR}$ of the RRM. By considering critical coupling condition at $\alpha = \tau = 0.8$ the SFDR of link is calculated at 500 MHz noise bandwidth and operational bandwidth (59.40 GHz to 61.56 GHz) as presented in Figure 3-10. As seen the SFDR of link using this RRM diminishes to the MZI modulator level in the desired frequency band.

The optical resonance linewidth can be altered by either ring radius or coupling conditions in a way that smaller ring perimeters (L) or lower coupling conditions yields wider resonance linewidth as described in Section 2.4. To observe the ring perimeter and coupling condition influences on the SFDR, the SFDR of link is calculated for a ring with 3.2 mm perimeter with $\alpha = \tau = 0.8$ and $\alpha = \tau = 0.7$ coupling conditions. As shown by altering ring perimeter and coupling condition the SFDR bandwidth is considerably improved and the RRM with $L = 3.2$ mm and $\alpha = \tau = 0.7$ can provide SFDR > 54 dB (~2 dB improvement versus MZI modulator) for the whole frequency band of interest.

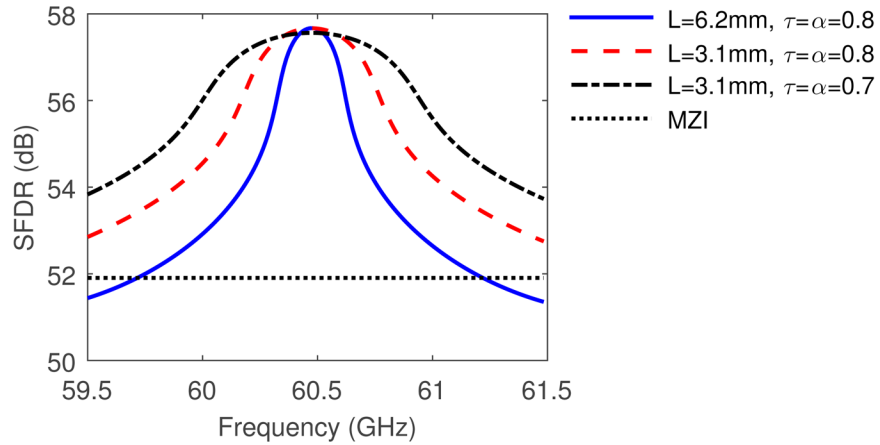


Figure 3-10 SFDR versus operational frequency around 60.5 GHz for ring resonator modulator in comparison with MZI modulator.

It should be noted that a RRM with wider resonance linewidth is needed in order to take advantage of the RRM ~ 5.8 dB SFDR improvement versus MZI modulator in the whole band of interest. In the case of simulated RRM the ring perimeter cannot be reduced further since the FSR will be larger than the targeted frequency band. The coupling condition can however be decreased further targeting maximum achievable improvement in the whole band. However obtaining wide range of coupling conditions can be challenging in the physical structure design step of RRM resulting in physical dimensions causing fabrication difficulties [133]. In addition polymers have limited range of refractive indexes (typically 1.5-1.7) and waveguides fabricated with polymer materials as their core and cladding experience weak mode confinement inside the core region leading to high bending loss in the ring waveguide [135]. Therefore polymer RRM have perimeters magnitudes on the order of millimeters [73, 103, 133]. Using materials with higher refractive indexes can provide more freedom in engineering RRM bandwidth. More options of refractive indexes exist by designing RRM within an silicon platform [124, 136] or hybrid waveguide structure consist of silicon as core and electro-optic polymer as cladding of waveguide [135, 137]. It should be stressed that wider resonance linewidth comes with the price of lower modulation index reducing link gain and noise figure along with higher DC bias voltage required by the modulator. However since the linearity of modulator in a MPL is a dominant factor in achieving application required SFDR it is beneficial to increase operation bandwidth of SFDR with a slight degradation in gain and noise figure.

3.8 Summary

Limitations of RRM frequency response modeling with static method required use of dynamic method to show complete behavior of RRM in MPLs. An analytical approach based on dynamic method is developed for harmonic distortions of RRM pointing out the suppression of harmonic distortions at specific operational points of the Lorentzian transfer function.

The RRM third harmonic distortion suppression provides high SFDR of $125 \text{ dB} \cdot \text{Hz}^{4/5}$ in a MPL which is $\sim 15 \text{ dB}$ SFDR improvement versus MZI modulators. The RRM SFDR superiority fades rapidly at wider operational bandwidth. For instance the RRM with chosen parameters can keep the $\text{SFDR} > 120 \text{ dB}$ (1 Hz noise bandwidth) at just $\sim 40 \text{ MHz}$ of operational bandwidth and SFDR drops below MZI modulator level at $\sim 1.4 \text{ GHz}$. The bandwidth limitation of SFDR is tighter than the modulation index dictated bandwidth and thus for analog applications the SFDR required bandwidth needs to be considered for RRM design.

Increasing SFDR utilizing RRM is the result of third order harmonic cancellation. The SFDR increase considerably diminishes with requirements of noise bandwidth. A bias voltage adjustment method is proposed and assessed maximizing SFDR for various noise bandwidths. Adjusting the RRM bias voltage a SFDR $\sim 57.7 \text{ dB}$ is achieved for 500 MHz noise bandwidth that is $\sim 5.8 \text{ dB}$ more than MZI modulators. While the SFDR shows high vulnerability to the coupling condition tolerance resulting from fabrication it is shown using a second level bias voltage adjustment the RRM can maintain a $\text{SFDR} > 57 \text{ dB}$ despite coupling condition tolerance of ± 0.05 . Results are summarized in Table 3-3 to point out the effectiveness of bias voltage adjustment in improving the SFDR of RRM versus MZI. The developed bias adjustment method can be expanded to dynamic bias voltage controlling in order to mitigate imposed conditions of wavelength tolerance and thermal effects.

Table 3-3 SFDR comparison of RRM and MZI in various instantaneous bandwidths
SFDR (dB)

	RRM	MZI
	With bias voltage adjustment	Biased at $V\pi/2$
B = 1 Hz,	127.9	109.9
B = 10 MHz	71.6	63.2
B = 500 MHz	57.7	51.9
B = 500 MHz ^a	57-57.7	-----

^a Including ± 0.05 tolerances for coupling conditions (τ and α) in RRM.

This bias adjustment method for noise bandwidths and fabrication tolerances opens the path for RRM advancement in MPL applications which require high operation frequency while in a limited band. RoF application of 60 GHz wireless access network is targeted as an example to examine operational bandwidth of RRM dictated by the SFDR. By engineering a ring resonator structure the RRM is a promising alternative electro-optic modulator providing higher SFDR in comparison with MZI modulator in the range of operational bands for the next generation wireless communication using millimeter-wave wireless access networks.

Although the developed bias voltage adjustment method and ring structure engineering open the path for RRM advancement in some MPL applications, still the SFDR narrow bandwidth is the main drawback of RRM for most of MPL applications. To exploit the RRM advantages of high SFDR, high modulation index, smaller size, and less power consumption in MPLs it is appealing to investigate methods providing high SFDR in wider bandwidths.

Chapter 4: Dual Ring Resonator Modulator

The high SFDR advantage of RRM discussed in Chapter 3 is promising for some applications with limited operational bandwidths. In order to advance RRM for a wider range of applications the improvement of SFDR bandwidth is inevitable to provide more than 15 dB (1 Hz noise bandwidth) improvements in GHz operational bandwidths versus MZI modulator. To improve SFDR bandwidth the IMD3 distortion needs to be suppressed in wider bandwidths. Dynamics of IMD3 distortion in a RRM are analyzed by further developing the theoretical model for two-tone test. The IMD3 power is analyzed versus fundamental signal power showing that IMD3 power has cubic modulation index dependence however the fundamental signal power has linear modulation index dependence. The developed theoretical model leads to a novel strategy to suppress IMD3 power independent of operational frequency by dividing the RF and optical powers in specific ratios between two RRM in a structure shown in Figure 4-1 and named as dual ring resonator modulator (DRRM). The RF power splitting ratio (F) between two RRM is set according to the optical power splitting ratio. Electrodes can be designed in either lumped or traveling-wave types and depending on the utilized electro-optic material type electrodes locate side-by-side or top-bottom of the optical waveguide. By adjusting RF and optical power ratios, RRM generate equal powers of third harmonic distortions but out-of-phase that are cancelled after recombining the outputs of photodetectors in electrical domain. The third harmonic cancelation approach is frequency independent yielding ~15 dB SFDR improvement (1 Hz noise bandwidth) versus MZI modulators. The impact of the modulator on microwave photonic link figure of merits is analyzed and compared to RRM and MZI modulators.

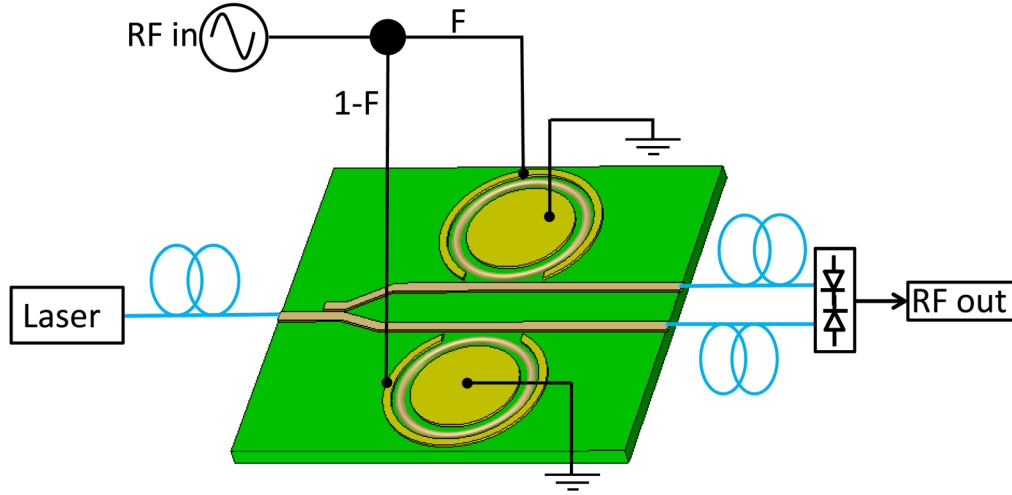


Figure 4-1 Schematic of a MPL with dual ring resonator modulator.

4.1 IMD3 suppression strategy

A Dual Ring Resonator Modulator (DRRM) is proposed to cancel the 3rd order harmonic portion of the IMD3 in order to maintain SFDR over a large bandwidth. Equal powers of the 3rd order harmonic are produced by the DRRM with 180° phase difference allowing cancellation of the 3rd order harmonic. However, the cancellation process of the 3rd harmonic slightly suppresses the fundamental signal as quantified later in Section 4.2. To yield the maximum SFDR the optical and RF powers are divided with a specific ratio between the two RRM paths providing minimum cancellation of the fundamental signal.

To develop a strategy for IMD3 suppression in wide bandwidths the dynamics of IMD3 power are analyzed versus fundamental signal. The analytical approach presented in the Chapter 3 is developed further by applying two-tone test to the RRM dynamic transfer function and extracting the fundamental signal and IMD3 signal powers. Similar to the single tone test, see Section 3-3, the $\exp\left(-j\left(n\theta + \delta_n \sin(\omega_m t - n\phi)\right)\right)$ part is expanded to frequency components. The exponential part shown as E can be written as Equation (4.1) with real and imaginary parts shown in Equations (4.2) and (4.3).

$$\begin{aligned}
E &= \exp\left(-j\left(n\theta + \delta_n\left(\sin(\omega_1 t) + \sin(\omega_2 t)\right)\right)\right) \\
&= \exp(-jn\theta) \times \exp\left(-j\delta_n\left(\sin(\omega_1 t)\right)\right) \times \exp\left(-j\delta_n\left(\sin(\omega_2 t)\right)\right) \\
&= \left[\cos(n\theta) - j\sin(n\theta)\right] \times \left[\cos(\delta_n \sin(\omega_1 t)) - j\sin(\delta_n \sin(\omega_1 t))\right] \\
&\quad \times \left[\cos(\delta_n \sin(\omega_2 t)) - j\sin(\delta_n \sin(\omega_2 t))\right]
\end{aligned} \tag{4.1}$$

$$\begin{aligned}
\text{Re}(E) &= \cos(n\theta) \times \cos(\delta_n \sin(\omega_1 t)) \times \cos(\delta_n \sin(\omega_2 t)) \\
&\quad - \sin(n\theta) \times \sin(\delta_n \sin(\omega_1 t)) \times \cos(\delta_n \sin(\omega_2 t)) \\
&\quad - \cos(n\theta) \times \sin(\delta_n \sin(\omega_1 t)) \times \sin(\delta_n \sin(\omega_2 t)) \\
&\quad - \sin(n\theta) \times \cos(\delta_n \sin(\omega_1 t)) \times \sin(\delta_n \sin(\omega_2 t))
\end{aligned} \tag{4.2}$$

$$\begin{aligned}
\text{Im}(E) &= -j\sin(n\theta) \times \cos(\delta_n \sin(\omega_1 t)) \times \cos(\delta_n \sin(\omega_2 t)) \\
&\quad - j\cos(n\theta) \times \sin(\delta_n \sin(\omega_1 t)) \times \cos(\delta_n \sin(\omega_2 t)) \\
&\quad + j\sin(n\theta) \times \sin(\delta_n \sin(\omega_1 t)) \times \sin(\delta_n \sin(\omega_2 t)) \\
&\quad - j\cos(n\theta) \times \cos(\delta_n \sin(\omega_1 t)) \times \sin(\delta_n \sin(\omega_2 t))
\end{aligned} \tag{4.3}$$

By using Bessel function expansions presented in Equation (3.14) and (3.15) the $\text{Re}(E)$ and $\text{Im}(E)$ are given by Equation (4.4) where Bessel functions are considered up to the third order.

$$\begin{aligned}
\text{Re}(E) &= \cos(n\theta) \\
&\times [J_0(\delta_n) + 2J_2(\delta_n)\cos(2\omega_1 t) + \dots] \\
&\times [J_0(\delta_n) + 2J_2(\delta_n)\cos(2\omega_2 t) + \dots] \\
&- \sin(n\theta) \\
&\times [2J_1(\delta_n)\sin(\omega_1 t) + 2J_3(\delta_n)\sin(3\omega_1 t) + \dots] \\
&\times [J_0(\delta_n) + 2J_2(\delta_n)\cos(2\omega_2 t) + \dots] \\
&- \cos(n\theta) \\
&\times [2J_1(\delta_n)\sin(\omega_1 t) + 2J_3(\delta_n)\sin(3\omega_1 t) + \dots] \\
&\times [2J_1(\delta_n)\sin(\omega_2 t) + 2J_3(\delta_n)\sin(3\omega_2 t) + \dots] \\
&- \sin(n\theta) \\
&\times [J_0(\delta_n) + 2J_2(\delta_n)\cos(2\omega_1 t) + \dots] \\
&\times [2J_1(\delta_n)\sin(\omega_2 t) + 2J_3(\delta_n)\sin(3\omega_2 t) + \dots]
\end{aligned} \tag{4.4}$$

$$\begin{aligned}
\text{Im}(E) &= -j\sin(n\theta) \\
&\times [J_0(\delta_n) + 2J_2(\delta_n)\cos(2\omega_1 t) + \dots] \\
&\times [J_0(\delta_n) + 2J_2(\delta_n)\cos(2\omega_2 t) + \dots] \\
&- j\cos(n\theta) \\
&\times [2J_1(\delta_n)\sin(\omega_1 t) + 2J_3(\delta_n)\sin(3\omega_1 t) + \dots] \\
&\times [J_0(\delta_n) + 2J_2(\delta_n)\cos(2\omega_2 t) + \dots] \\
&+ j\sin(n\theta) \\
&\times [2J_1(\delta_n)\sin(\omega_1 t) + 2J_3(\delta_n)\sin(3\omega_1 t) + \dots] \\
&\times [2J_1(\delta_n)\sin(\omega_2 t) + 2J_3(\delta_n)\sin(3\omega_2 t) + \dots] \\
&- j\cos(n\theta) \\
&\times [J_0(\delta_n) + 2J_2(\delta_n)\cos(2\omega_1 t) + \dots] \\
&\times [2J_1(\delta_n)\sin(\omega_2 t) + 2J_3(\delta_n)\sin(3\omega_2 t) + \dots]
\end{aligned} \tag{4.5}$$

By multiplying the components in Equation (4.4) and Equation (4.5) and using trigonometric identity functions, $\text{Re}(E)$ and $\text{Im}(E)$ can be written as presented in Equations (4.6) and (4.7).

$$\begin{aligned}
\text{Re}(E) = & \cos(n\theta) \\
& \times \left[J_0(\delta_n)J_0(\delta_n) + 2J_0(\delta_n)J_2(\delta_n)\cos(2\omega_1 t) \right. \\
& + 2J_0(\delta_n)J_2(\delta_n)\cos(2\omega_2 t) \\
& + 2J_2(\delta_n)J_2(\delta_n)\cos(2(\omega_1 - \omega_2)t) \\
& \left. + 2J_2(\delta_n)J_2(\delta_n)\cos(2(\omega_1 + \omega_2)t) \right] \\
& - \sin(n\theta) \\
& \times \left[2J_0(\delta_n)J_1(\delta_n)\sin(\omega_1 t) + 2J_0(\delta_n)J_3(\delta_n)\sin(3\omega_1 t) \right. \\
& + 2J_1(\delta_n)J_2(\delta_n)\sin((\omega_1 + 2\omega_2)t) \\
& + 2J_1(\delta_n)J_2(\delta_n)\sin((\omega_1 - 2\omega_2)t) \\
& + 2J_2(\delta_n)J_3(\delta_n)\sin((2\omega_1 + 3\omega_2)t) \\
& \left. + 2J_2(\delta_n)J_3(\delta_n)\sin((2\omega_1 - 3\omega_2)t) \right] \\
& - \cos(n\theta) \\
& \times \left[2J_1(\delta_n)J_1(\delta_n)\cos((\omega_1 - \omega_2)t) \right. \\
& - 2J_1(\delta_n)J_1(\delta_n)\cos((\omega_1 + \omega_2)t) \\
& + 2J_1(\delta_n)J_3(\delta_n)\cos((\omega_1 - 3\omega_2)t) \\
& - 2J_1(\delta_n)J_3(\delta_n)\cos((\omega_1 + 3\omega_2)t) \\
& + 2J_3(\delta_n)J_3(\delta_n)\cos(3(\omega_1 - \omega_2)t) \\
& \left. - 2J_3(\delta_n)J_3(\delta_n)\cos(3(\omega_1 + \omega_2)t) \right] \\
& - \sin(n\theta) \\
& \times \left[2J_0(\delta_n)J_1(\delta_n)\sin(\omega_2 t) \right. \\
& + 2J_0(\delta_n)J_3(\delta_n)\sin(3\omega_2 t) \\
& + 2J_1(\delta_n)J_2(\delta_n)\sin((2\omega_1 + \omega_2)t) \\
& - 2J_1(\delta_n)J_2(\delta_n)\sin((2\omega_1 - \omega_2)t) \\
& + 2J_2(\delta_n)J_3(\delta_n)\sin((2\omega_1 + 3\omega_2)t) \\
& \left. - 2J_2(\delta_n)J_3(\delta_n)\sin((2\omega_1 - 3\omega_2)t) \right]
\end{aligned} \tag{4.6}$$

$$\begin{aligned}
\text{Im}(E) = & -j \sin(n\theta) \\
& \times \left[J_0(\delta_n) J_0(\delta_n) + 2J_0(\delta_n) J_2(\delta_n) \cos(2\omega_1 t) \right. \\
& + 2J_0(\delta_n) J_2(\delta_n) \cos(2\omega_2 t) \\
& + 2J_2(\delta_n) J_2(\delta_n) \cos(2(\omega_1 - \omega_2)t) \\
& \left. + 2J_2(\delta_n) J_2(\delta_n) \cos(2(\omega_1 + \omega_2)t) \right] \\
& - j \cos(n\theta) \\
& \times \left[2J_0(\delta_n) J_1(\delta_n) \sin(\omega_1 t) + 2J_0(\delta_n) J_3(\delta_n) \sin(3\omega_1 t) \right. \\
& + 2J_1(\delta_n) J_2(\delta_n) \sin((\omega_1 + 2\omega_2)t) \\
& + 2J_1(\delta_n) J_2(\delta_n) \sin((\omega_1 - 2\omega_2)t) \\
& + 2J_2(\delta_n) J_3(\delta_n) \sin((3\omega_1 + 2\omega_2)t) \\
& \left. + 2J_2(\delta_n) J_3(\delta_n) \sin((3\omega_1 - 2\omega_2)t) \right] \\
& + j \sin(n\theta) \\
& \times \left[2J_1(\delta_n) J_1(\delta_n) \cos((\omega_1 - \omega_2)t) \right. \\
& - 2J_1(\delta_n) J_1(\delta_n) \cos((\omega_1 + \omega_2)t) \\
& + 2J_1(\delta_n) J_3(\delta_n) \cos((3\omega_1 - \omega_2)t) \\
& - 2J_1(\delta_n) J_3(\delta_n) \cos((3\omega_1 + \omega_2)t) \\
& + 2J_3(\delta_n) J_3(\delta_n) \cos(3(\omega_1 - \omega_2)t) \\
& \left. - 2J_3(\delta_n) J_3(\delta_n) \cos(3(\omega_1 + \omega_2)t) \right] \\
& - j \cos(n\theta) \\
& \times \left[2J_0(\delta_n) J_1(\delta_n) \sin(\omega_2 t) \right. \\
& + 2J_0(\delta_n) J_3(\delta_n) \sin(3\omega_2 t) \\
& + 2J_1(\delta_n) J_2(\delta_n) \sin((2\omega_1 + \omega_2)t) \\
& - 2J_1(\delta_n) J_2(\delta_n) \sin((2\omega_1 - \omega_2)t) \\
& + 2J_2(\delta_n) J_3(\delta_n) \sin((2\omega_1 + 3\omega_2)t) \\
& \left. - 2J_2(\delta_n) J_3(\delta_n) \sin((2\omega_1 - 3\omega_2)t) \right]
\end{aligned} \tag{4.7}$$

From Equation (4.6) and Equation (4.7) various harmonics and intermodulation distortions can be recognized. By extracting fundamental signal and IMD3 amplitudes at real and imaginary parts of (E) Equation (4.8) and Equation (4.9) are given. By replacing these relations in RRM transfer function [Equation (3.6)] finally Equation (4.10) and Equation (4.11) are obtained for output RF signal and IMD3 powers.

$$\begin{aligned} \text{Re}(E)_{IMD3} &\propto -\sin(n\theta) 2J_1(\delta_n) J_2(\delta_n) \\ \text{Im}(E)_{IMD3} &\propto -j \cos(n\theta) 2J_1(\delta_n) J_2(\delta_n) \end{aligned} \quad (4.8)$$

$$\begin{aligned} \text{Re}(E)_{Fun} &\propto -\sin(n\theta) 2J_0(\delta_n) J_1(\delta_n) \\ \text{Im}(E)_{Fun} &\propto -j \cos(n\theta) 2J_0(\delta_n) J_1(\delta_n) \end{aligned} \quad (4.9)$$

$$P_{Fun} \propto \left| \tau - (1 - \tau^2) \sum_{n=1}^{\infty} \tau^{n-1} \alpha^n \times \left[-\sin(n\theta) 2J_0(\delta_n) J_1(\delta_n) - j \cos(n\theta) 2J_0(\delta_n) J_1(\delta_n) \right] \right|^2 \quad (4.10)$$

$$P_{IMD3} \propto \left| \tau - (1 - \tau^2) \sum_{n=1}^{\infty} \tau^{n-1} \alpha^n \times \left[-\sin(n\theta) 2J_1(\delta_n) J_2(\delta_n) - j \cos(n\theta) 2J_1(\delta_n) J_2(\delta_n) \right] \right|^2 \quad (4.11)$$

Obtained relations for fundamental and IMD3 powers show that the fundamental signal power is proportional to the $J_0(\delta_n) J_1(\delta_n)$ product, however the IMD3 signal power is related to the product of Bessel functions $J_1(\delta_n) J_2(\delta_n)$. In analog modulation the applied RF signal is in small signal criteria with one or more orders of magnitude smaller than DC operational points yielding the $\delta_n \ll 1$ and hence the $J_0(\delta_n) J_1(\delta_n)$ and $J_1(\delta_n) J_2(\delta_n)$ products can be expanded as shown in Equation (4.12) and Equation (4.13).

$$J_0(\delta_n) J_1(\delta_n) = -\delta_n + \text{higher orders} \quad (4.12)$$

$$J_1(\delta_n) J_2(\delta_n) = -\frac{1}{16} \delta_n^3 + \text{higher orders} \quad (4.13)$$

The output fundamental signal power has approximately linear modulation index dependence according to Equations (4.12) and (4.13) while the IMD3 signal power has approximately the cubic modulation index dependence. Derived relations provide a method to suppress IMD3 power by utilizing third harmonic cancellation while maintaining fundamental signal suppression at a minimum level. Dividing RF and optic powers between two RRM's in order to produce equal powers of third harmonic with 180° phase difference at the detectors yields complete third harmonic cancellation.

To illustrate, consider dividing the RF input power between two modulators such that RF input voltage amplitude for one modulator (main) is two times of the RF voltage amplitude for another modulator (secondary). Then the output third harmonic power from the primary modulator is eight times of the third harmonic power from the secondary one. If the optic power is divided between two modulators that primary modulator receives eight times optic power less than the secondary modulator the third harmonic powers from primary and secondary modulators are expected to be equal. By having 180° phase difference in the third harmonic signals from the modulators the third harmonic signal is completely cancelled after combining the outputs of the detectors as shown in Figure 4-1.

The suggested method can be formulated as following that to cancel the third order harmonic of IMD3 two RRM's are utilized with divided RF power at ratio $F^2:1$ while optical power ratio needs to be the inverse cube of the RF power ratio, i.e. $1:F^3$. The main modulator is fed by higher RF power while receiving less optical power and the secondary modulator receives less RF power but it is driven with higher optical power. The optical power ratio ($1:F^3$) between the modulators is set by the coupling ratio between the base waveguides of the main and secondary modulators. If the RF and optical power are held at the previously mentioned ratios the third harmonic produced from two modulators is equal and exactly canceled at the output.

The output power vs. input power for the fundamental and the IMD3 for RRM and DRRM (both biased at V_A according to Figure (3.1)) with $F = 3$ are shown in Figure 4-2. In the

DRRM IMD3 power is suppressed more than fundamental signal yielding an enhancement in SFDR as marked in Figure 4-2. It is worth mentioning that the IMD3 power versus input power in the RRM has a slope equal to 3 showing third order harmonic contribution in IMD3. Having a linearization process in the DRRM the slope of IMD3 increases to 7, therefore by biasing the modulators at the proper voltages and having DRRM with the proper power ratio of RF and optical powers both third and fifth order harmonics are cancelled.

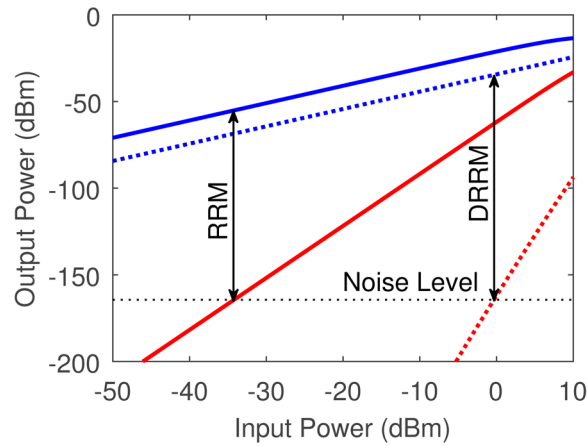


Figure 4-2 Output fundamental and IMD3 powers against the RF input power. Lines are the results for single RRM and dots are for the DRRM. Results are for 6 mm rings biased at V_A . Noise level is at ~ -164 dBm in 1 Hz bandwidth.

To take advantage of the fifth order harmonic suppression modulators are biased at voltages that the fifth order harmonic is suppressed (V_A) as shown in Figure (3.1). However in order to produce 180° degree phase difference between IMD3 signals at the output, the ring modulators branches need to be biased at voltages that are symmetric versus the center of the Lorentzian transfer function as shown in Figure 4-3(a) by $\pm V_A$. To confirm third order harmonic cancellation in DRRM harmonic distortions are calculated and compared to the RRM as shown in Figure 4-3(b). The third harmonic is suppressed in the range of ~ 130 dB while the fundamental signal is decreased by ~ 14 dB showing the capability of DRRM to suppress IMD3 and enhance SFDR.

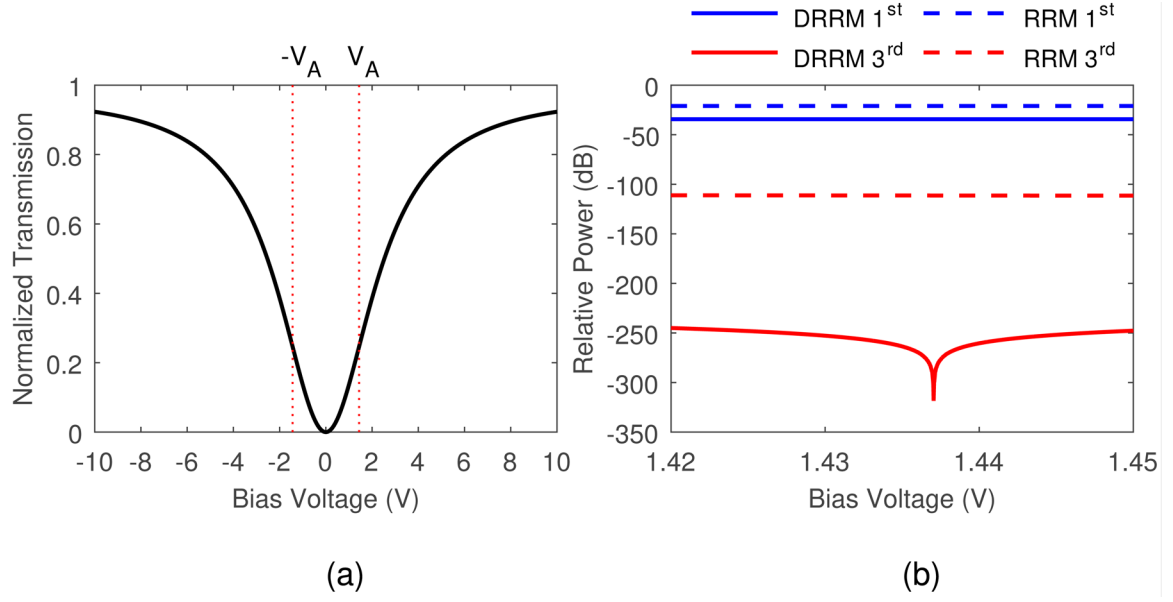


Figure 4-3 (a) Lorentzian transfer function of a RRM versus bias voltage showing the symmetrical bias points ($\pm V_A$), (b) fundamental and 3rd harmonic distortion in DRRM and RRM versus bias voltage.

4.2 DRRM figure of merits

The DRRM provides the third order harmonic cancellation process which is independent of frequency. Variation of the SFDR versus operating RF frequency is shown in Figure 4-4 for DRRM and compared to the RRM. When the operating RF frequency is at resonance frequency the complete suppression of the fifth order harmonic comes with biasing at V_A . Working at frequencies away from resonance the fifth harmonic contribution in IMD3 power increases reducing SFDR, however DRRM maintains complete cancellation of the third harmonic regardless of the operating frequency. Therefore DRRM provides SFDR > 129 dB (1 Hz noise bandwidth) in a relatively narrow operational bandwidth around the resonance frequency (~ 40 MHz) while keeping SFDR > 124.6 dB (1 Hz noise bandwidth) at unlimited operational bandwidth. The nondispersive third harmonic cancellation using DRRM is a great advantage in comparison with ring assisted MZI modulators where the linearization process is highly sensitive to the operating frequency [81, 98].

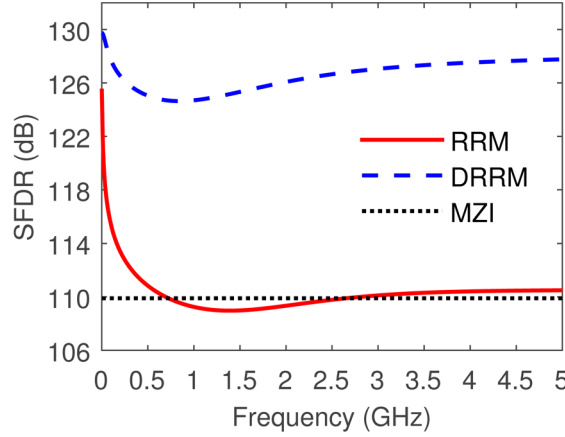


Figure 4-4 SFDR versus RF operating frequency for RRM, DRRM and MZI. SFDR is calculated for 1 Hz noise bandwidth. RRM is biased at V_B and DRRM is biased at V_A .

It is inevitable that with the DRRM there will be some reduction of the fundamental signal affecting system level figure of merits mainly gain and noise figure. The reduction of the fundamental signal is not linearly related to the F-ratio therefore the link figure of merits is analyzed by sweeping the F-ratio as shown in Figure 4-5. Optimum figure of merits is obtained at $F \sim 2.4$ when minimum cancellation of the fundamental signal occurs yielding improvement in SFDR, gain and noise figure. According to this ratio optical power splitter should be designed to split optical power at $1:2.4^3$ while RF power is divided in $2.4^2:1$ ratio.

The main challenge in order to maximize link figure of merits is to design and fabricate optical and RF power splitters precisely. The optical power splitter ratio is set in the fabrication process and no control is accessible after fabrication step within the current design. Moreover, depending on the material used in the fabrication, optical power splitter can be vulnerable to the device thermal fluctuations. RF power splitting can be controlled in the application step and the RF splitting ratio can be tuned to the desired number after obtaining measurements of optical power splitter in order to satisfy the ratio relations between RF and optical powers. The DRRM imposes a very high tolerance of the SFDR to the RF signal splitting ratio accuracy as shown in Figure 4-6. Results are calculated for $F = 3$ meaning the RF voltage amplitude should be divided in 75% to 25% between the

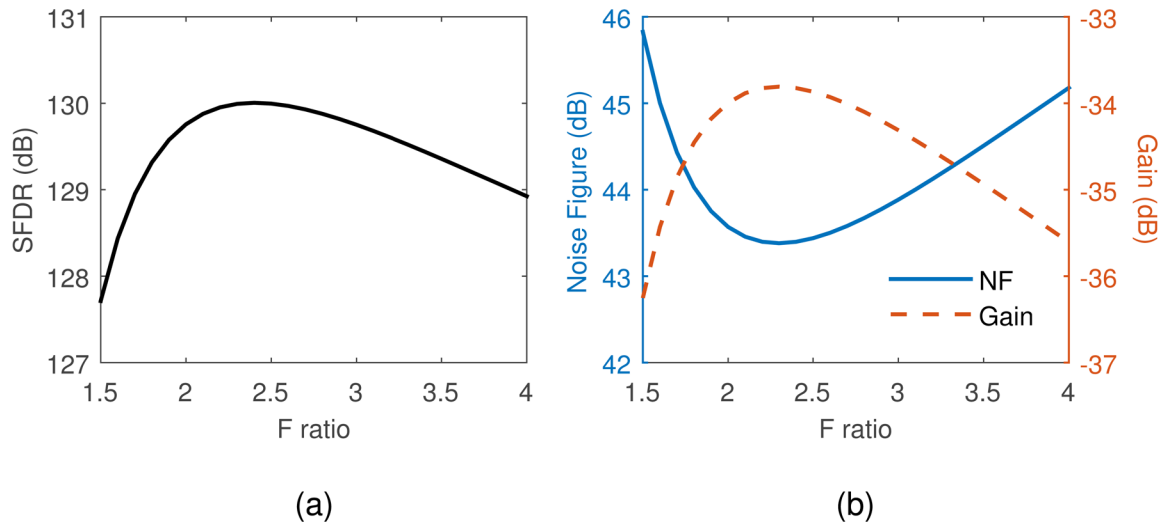


Figure 4-5 Link figure of merits versus F-ratio (a) SFDR, (b) noise figure and gain.

main modulator and the secondary modulator respectively. In order to analyze the tolerance of the DRRM to splitting ratio the voltage amplitude receiving by the second modulator is swept around 25% ratio while keeping the fixed 75% voltage amplitude receiving by the main modulator. To keep the SFDR > 120 dB the RF voltage amplitude needs to be divided in a resolution finer than 0.2% of the input amplitude. To control RF dividing ratio with this high accuracy active control will likely be necessary where an active feedback feed by distortion of a pilot tone can be used [49]. In addition dividing RF signal with high accuracy can be achieved utilizing integration techniques to minimize the fabrication and application tolerances [67].

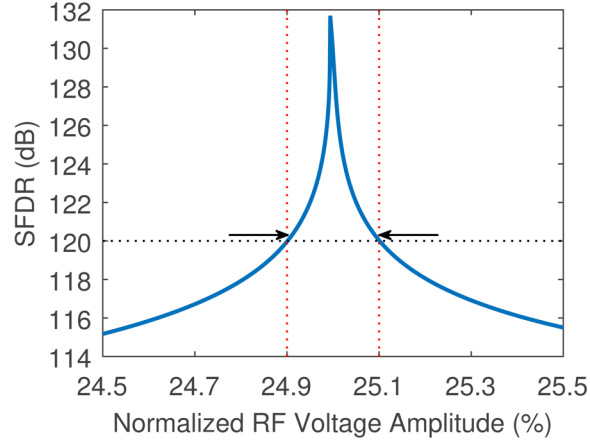


Figure 4-6 SFDR change versus RF voltage amplitude received by the secondary modulator.

Although the DRRM can provide high SFDR in wide bandwidth, the DRRM inherits operational bandwidth limits from the RRM in terms of the modulation index affecting gain and noise figure. The RRM and consequently the DRRM impose bandwidth limitation to the modulation index based on optical resonance line-width (BW_{res}). The BW_{res} can be controlled by the optical resonator structure including size of the ring and coupling parameters and is the trade-off for an increasing in modulation index as discussed in Chapter 3. High-Q optical resonances result in an increased modulation efficiency, but more limited RF bandwidth. In Figure 4-7 variation of the link figure of merits, gain and noise figure versus operating RF frequency up to 5 GHz is shown for RRM and DRRM. While SFDR improvement in DRRM is clear in Figure 4-4, gain and noise figure is slightly diminished due to the fundamental signal reduction as shown in Figure 4-7. Since SFDR is not a bandwidth limiting factor for DRRMs, unlike RRM, the ring resonators in DRRM can be designed according to bandwidth requirements of gain and noise figure.

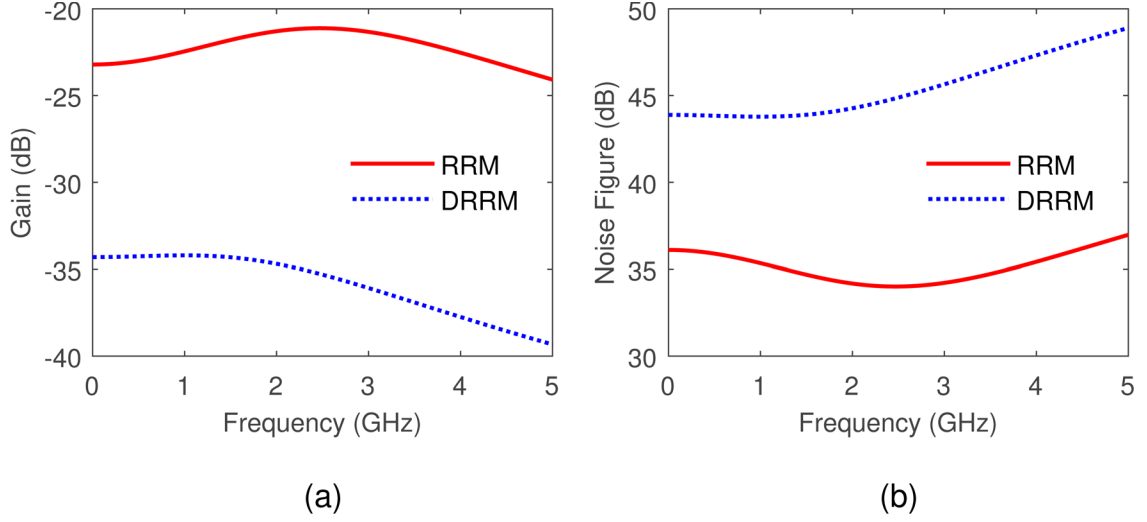


Figure 4-7 Link figure of merits versus operational bandwidth using RRM and DRRM, (a) gain, and (b) noise figure.

By using traveling-wave electrodes the capacitance and the photon transit-time bandwidth limitations due to the lumped electrodes are removed [128] and the DRRM can operate at multiples of FSR. A DRRM with lumped electrode can be only operated in baseband up to $BW_{\text{res}}/2$. However a DRRM with traveling-wave electrodes can work at multiples of FSR with BW_{res} around the resonance frequency. By utilizing traveling-wave electrodes the DRRM inherits the advantages in enhanced modulation index from RRM for high frequency operations. RRM modulators provide higher modulation index in a bandwidth around the resonance frequency in comparison to the MZI based modulators when the velocity mismatch and RF loss are taken into account as described in Chapter 2 [73]. Although the SFDR of DRRM reported here is calculated based on the lumped electrode the results can be generalized to the traveling-wave electrodes since the type of electrode does not affect the linearization process in DRRM. However for the gain and noise figure, similar to RRM as discussed in Chapter 3, microwave electrode loss and velocity mismatch factors must be taken into account since these factors can have detrimental effect on modulation index at multiple FSR operating frequencies [73, 103].

For practical implementations SFDR versus the noise bandwidth is a critical link parameter as discussed for RRM in Section 3-5. As seen in Figure 4-2 IMD3 power shows constant slope in the RF input power range of interest and Equation (1.4) is utilized to calculate SFDR at noise bandwidths other than 1 Hz. For DRRM operating at frequencies close to the resonance frequency both third and fifth order harmonics are cancelled yielding $m = 7$ while at frequencies away from the resonance just the third order harmonic is cancelled yielding $m = 5$. In Figure 4-8 variation of SFDR versus instantaneous bandwidth is presented for the DRRM in comparison with MZI. In order to show the operational frequency effect on SFDR versus noise bandwidth the results for DRRM are presented in 1 Hz and 5 GHz frequencies. The DRRM in comparison with MZI presents $\sim 7\text{--}9$ dB SFDR improvement in 1 MHz instantaneous bandwidth while improving ~ 3 dB at 1 GHz instantaneous bandwidth. Results show that DRRM loses its SFDR superiority by large margin in high noise bandwidths because of harmonic cancellations similar to the RRM. Proposing a method, similar to the developed method for RRM in Section 3-5, to restore the DRRM advantage of high SFDR at high noise bandwidths would be beneficial in future application implementations.

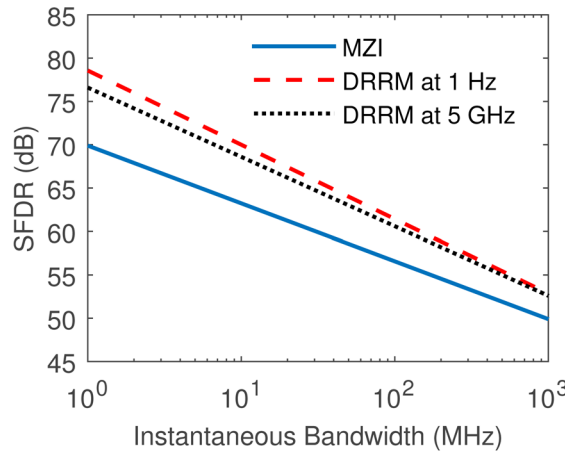


Figure 4-8 SFDR versus instantaneous bandwidth in MZI and DRRM.

A comparison between DRRM, RRM, and MZI modulators is summarized in Table 4-1. Operational bandwidths and noise bandwidths are considered ± 5 GHz around the

resonance frequency and 1 GHz respectively. Since the RRM and DRRM have frequency dependence, due to the resonance, the figure of merits is defined in a range for ± 5 GHz operational bandwidth around the resonance frequency. DRRM can provide ~ 4 – 15 dB and ~ 15 – 20 dB SFDR improvement versus RRM and MZI respectively in 1 Hz instantaneous bandwidth. In 1 GHz instantaneous bandwidth the DRRM maintains ~ 3 dB SFDR improvement versus MZI. The low improvement in 1 GHz instantaneous bandwidth is related to the higher order harmonic cancellation method yielding higher m in Equation (1.4). The presented SFDR improvement comes with the price of the gain and noise figure deteriorating as quantified in Table 4-1. However it should be stressed that the SFDR is a prevalent figure of merit for increasing performance metrics and wide scale implementation. While linearity of the modulator has the direct critical effect on the SFDR of MPL there are other mechanisms to mitigate degradation of the gain and noise figure including use of higher laser power, higher detector responsivity, and lower laser relative intensity noise. In addition, resonator structure in the DRRM can be modified to address gain and noise figure requirements since SFDR is not a limiting factor while the narrow bandwidth of SFDR is the main limiting factor of RRM as described in Chapter 3.

The DRRM requires lower DC bias voltage compared to RRM and MZI modulator as quantified in Table 4-1. The lower bias voltage helps in reducing the power consumption in DRRMs however for a complete assessment of the power consumption other factors such as optical power loss, power consumptions in photodetectors, and gain reductions need to be considered which can be a subject for future studies.

Table 4-1 DRRM, RRM and MZI figure of merits comparison

Figure-of-merits	MZI	RRM	DRRM
SFDR (dB) ^a	109.9	109 – 125.6	124.6 – 130
SFDR (dB) ^b	49.9	49 – 53.6	52.6 – 52.9
Gain (dB)	-24.2	-24.2 – -21.1	-39.5 – -34.2
Noise figure (dB)	37.1	34 – 37.1	43.8 – 49
DC Bias (V)	4.44 ^c	2.49	1.44

^a1 Hz instantaneous bandwidth, ^b1 GHz instantaneous bandwidth, ^c1 cm branch length

4.3 Summary

To investigate possible methods to suppress IMD3 power independent of frequency the theoretical analysis of RRM is expanded for two-tone test in order to analyze dynamics of IMD3 power versus fundamental signal. It is shown that IMD3 signal power has cubic modulation index dependence while the fundamental signal has linear modulation index dependence leading to a novel dual ring resonator modulator to obtain high SFDR at wide operational bandwidths. By dividing the RF and optical powers in specific ratios between two RRM and proper DC biasing the 3rd harmonic distortion signals at the output have equal powers but 180° of phase yielding the IMD3 power suppression independent of the operational frequency. The design takes advantage of fifth harmonic cancellation by proper biasing the modulators at narrow operational bandwidth around the resonance frequency in order to reach SFDR $\sim 130 \text{ dB.Hz}^{6/7}$ while the 3rd order cancellation method maintains the SFDR $> 124.6 \text{ dB.Hz}^{4/5}$ in frequencies away from the resonance frequency. The gain and noise figure of the DRRM design are degraded by $\sim 14 \text{ dB}$ and 12 dB respectively compared to the RRM because of the fundamental signal reduction. The gain and noise figure degradation can be mitigated by optimizing other link parameters such higher laser power, higher detector responsivity, and lower laser relative intensity noise. The resonator structure of DRRM also can be optimized to maximize the modulation index improving gain and noise figure.

The DRRM provides a platform to cancel 2nd, 3rd, and 5th harmonics simultaneously. The second and fifth harmonic cancellations are frequency dependent based on the resonance bandwidth however the 3rd harmonic cancellation is independent of frequency. The DRRM yields $\sim 15 \text{ dB}$ SFDR (at 1 Hz noise bandwidth) improvement versus MZI and RRM regardless of operational frequency. The high SFDR of DRRM is a promising factor for future advancements of MPLs.

Chapter 5: Ring Resonator Modulator Design

To fabricate electro-optic modulators, physical dimensions of modulators need to be chosen and optimized utilizing numerical simulation techniques. To succeed in realization of optimized electro-optic modulators the design process is critical and requires information from material properties, fabrication process/tolerances, and targeted applications.

RRMs are more complicated to design and fabricate in comparison with MZI modulators because the RRM functionality is highly related to the ring-waveguide coupling condition as discussed in Sections 3-1 and 3-6. The coupling condition is directly related to material properties and fabrication tolerances. To realize RRM operating in the desired ring-waveguide coupling condition precise design and fabrication processes are required. The design process is optimized by obtaining feedback from the fabrication process to take into account the fabrication tolerances.

A design procedure is developed to obtain physical dimensions of RRM. Different computational electromagnetic methods are studied and examined to identify the best capable method. Designs are conducted according to fabrication plans on an all-polymer platform however the developed design procedure can be useful in designing RRM in other types of material platforms.

5.1 Photonic device simulation methods

To design optical waveguides for the electro-optic modulators simulation tools are utilized to simulate light-wave propagation within the structures. The light-wave propagation inside waveguides is described by electromagnetic theory and is solved through numerical methods known as computational electromagnetic methods [138].

Numerical methods that directly solve the Maxwell equations without considering any approximations are called full-wave methods which are the most accurate solvers and are applied to wide range of problems. Finite Difference Time Domain (FDTD) as a time domain solver [139] and Finite Element Method (FEM) as a frequency domain solver [138] are powerful full-wave algorithms that are popular for photonic devices. However full-wave solvers are computationally intensive. In this work FDTD and FEM have been available through commercial software packages of RSOFTE and COMSOL respectively. Attempts made to simulate the desired RRM using FDTD and FEM are shown that the ring resonator simulation in three dimension with ring radius sizes in mm ranges is very demanding and not practical with the available computational resources of 256 GB memory.

Some types of approximations can be utilized to ease the computation requirements for optical waveguides. In optical waveguides for electro-optic modulators the light-wave propagation direction is known and unidirectional. In addition the light-wave is considered as slowly varying wave throughout the optical waveguide. According to these assumptions two types of computational electromagnetic methods have been developed namely beam propagation method (BPM) and beam envelope method (BEM) [140, 141]. BPM is based on finite difference method while BEM is based on finite element. BPM and BEM are common methods in designing various types of planar photonic devices including directional couplers, splitters, multimode interference devices, and modulators [142]. In this work BPM and BEM included in RSOFTE and COMSOL packages have been available respectively.

The approximations involved in BPM and BEM limit their implementation criteria specially for structures including discrete structure, fast changes, evanescent waves, scattering, and propagation in wide angles [143]. Wave propagation simulation inside the ring waveguide is also not possible utilizing standard BPM and BEM. However COMSOL BEM module can be modified in order to simulate ring resonator by defining the phase of

propagation wave (φ) inside the ring according to Equation (5.1) where β is the propagation constant, R is the ring radius, and (x, y) represents the coordinates of ring waveguide in the XY plane. By defining the phase of propagating wave inside the ring the COMSOL BEM solver is shown to be capable of simulating ring resonator structure while with much lower requirements of the computational memory and rings up to 2.5 mm radius are simulated in 3D with the available 256 GB memory.

$$\varphi = \beta \times R \times \tan^{-1}(x/y) \quad (5.1)$$

5.2 Single mode optical waveguides

Optical waveguides in electro-optic polymer modulators are based on a platform of stacked layers of passive and active polymer materials as shown in Figure 5-1. The electro-optic polymer material as core layer is sandwiched between cladding layers of non-active polymer materials for mode confinement while providing refractive index changes due to the applied electrical signal [144]. The propagating light-wave is confined due to the refractive index difference between core and cladding layers where $n_{clad} < n_{core}$ and the waveguide cross section structure [142]. Depending on the refractive indices of utilized materials and the operational wavelength the waveguide cross section is designed to support only single propagation mode in the desired polarization [144]. The polarization of propagating light-wave is chosen according to the direction of electro-optic coefficient and applied electric field. The TM polarization is the common polarization utilized for electro-optic polymer modulators and electrodes are located on the top and bottom of the waveguide as shown in Figure 5-1.

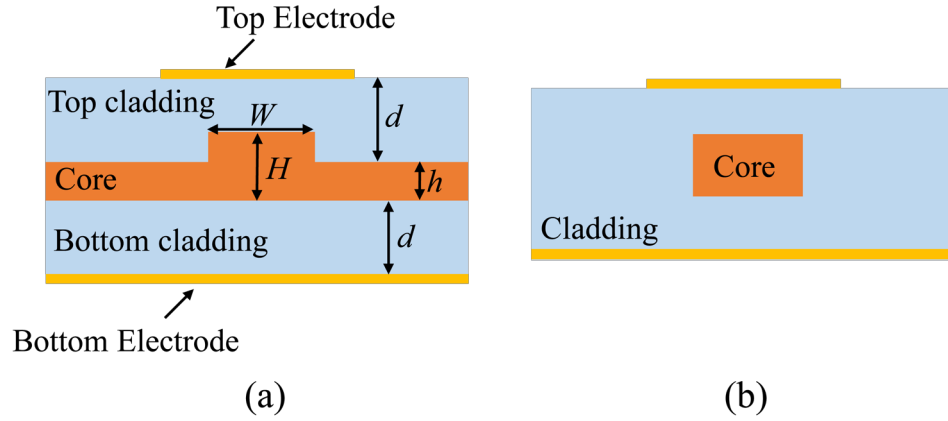


Figure 5-1 Cross section schematics of (a) a rib waveguide, and (b) a channel waveguide.

Waveguide cross section in electro-optic modulators can be in the form of channel and rib waveguides as shown in Figure 5-1 [145]. While the channel type waveguide shown in Figure 5-1(b) can provide better optical mode confinement, which can improve modulation efficiency, the rib type waveguide shown in Figure 5-1(a) is utilized [144]. Rib waveguides are chosen since larger mode sizes can be supported in single mode operation resulting in easier in/out light couplings. In addition for a ring resonator type structure the rib waveguide cross section is beneficial because of less mode confinement loosening the design constraints for ring resonator coupling conditions shown by g and R in Figure 5-2. Rib waveguide cross section can be fabricated utilizing common lithography followed by shallow etching steps yielding straight forward fabrication procedures. Rib waveguides are focused on hereafter.

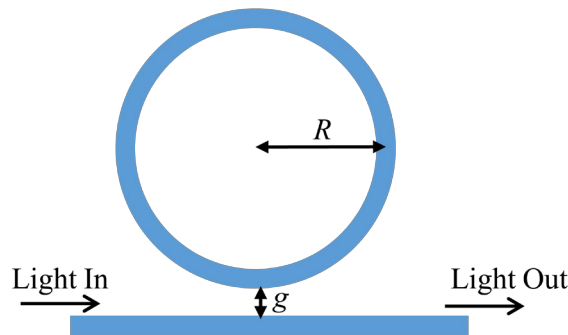


Figure 5-2 Top view of ring resonator structure.

Single mode criteria is calculated in a range of waveguide cross section dimensions of W , H , and h as shown in Figure 5-1(a). Single mode criteria in rib waveguides is determined according to the common higher order radiation method in shallow etched rib waveguides where $r = h/H \geq 0.5$ in order to take advantage of the large mode sizes [144]. In the higher order radiation method the rib section of the waveguide can be multimode, however, higher order modes in the rib area have an effective refractive index less than nearby slab waveguide modes [144]. Therefore the higher modes of rib area radiate horizontally into the slab modes and transform to evanescent modes.

To determine single mode criteria in shallow etched rib waveguides a relation of $\frac{W}{H} < K + \frac{r}{\sqrt{1-r^2}}$ is often utilized where K is a dimensionless constant [146, 147].

However the relation is an approximate and it was shown that in the case of polymer rib waveguides the resulted single mode criteria can be misleading and numerical analysis is required [148]. To simulate single mode criteria the mode solver modules from COMSOL and RSOFTE packages are used.

The single mode criteria is calculated considering materials and fabrication properties. Commercially available materials of SEO100C from Soluxra LLC and NOA73 from Norland Products Inc. are utilized for core and cladding layers respectively. Refractive indexes of SEO100C and NOA73 are used in design process as $n_{core} = 1.7$ and $n_{clad} = 1.55$ respectively. The core thickness (H) and the cladding thickness (d) are chosen according to properties of materials, fabrication, and implementation.

The core layer thickness range is limited due to the film uniformity degradation causing higher propagation loss. The SEO100C film thickness in the range of 2-2.7 μm is recommended by the manufacturer for a uniform layer. A thin core layer decreases the optical mode size causing difficulty in the light in/out coupling process [144]. In addition a thin core layer can add vulnerability from fabrication tolerances [144]. The core layer

thickness is chosen to be 2.7 μm in the design and confirmed by measurements utilizing profilometer technique.

The thickness of cladding layers is critical in poling and modulation efficiencies. Cladding layers are modeled as resistors around the core layer in determining voltage levels across the core layer during poling and modulation. Decreasing the cladding layer thickness is desired in order to increase the voltage levels across the core. However there is a trade-off in the cladding thickness since thinner cladding layers add to the optical mode loss due to the optical mode coupling to the bottom and top metallic layers serving as electrodes [144]. Simulation optimization results in a 4 μm maximum cladding thickness provides negligible optical mode loss (less than 0.1 dB/cm), while maintaining reasonable poling efficiency.

The single mode criteria is determined by calculating the effective refractive indices of slab modes as shown in Figure 5-3(a). A slab waveguide with 2.7 μm thickness can propagate three modes with refractive indices of (n_{r0}, n_{r1}, n_{r2}) as marked in Figure 5-3(a). In order to make single mode rib waveguide the refractive indices of higher order modes inside the rib need to be lower than the fundamental mode of surrounding slab layer. For instance a rib with 0.7 μm height formed in 2.7 core thickness (surrounding slab thickness is 2 μm) results in an effective refractive index of n_{s0} for slab mode, which is higher than n_{r1} and n_{r2} yielding horizontally radiation of higher order modes into the slab modes. To obtain single mode criteria the higher order radiation pattern is examined for a range of waveguide width as shown in Figure 5-3(b). The boundary between single mode and multimode region shows the maximum waveguide width (W) which results in single mode condition for each rib height ratio (h/H). The single mode criteria identifies a range of W and h that can be chosen however the exact values of W and h are designed according to the ring-waveguide coupling condition as described in Section 5.3.

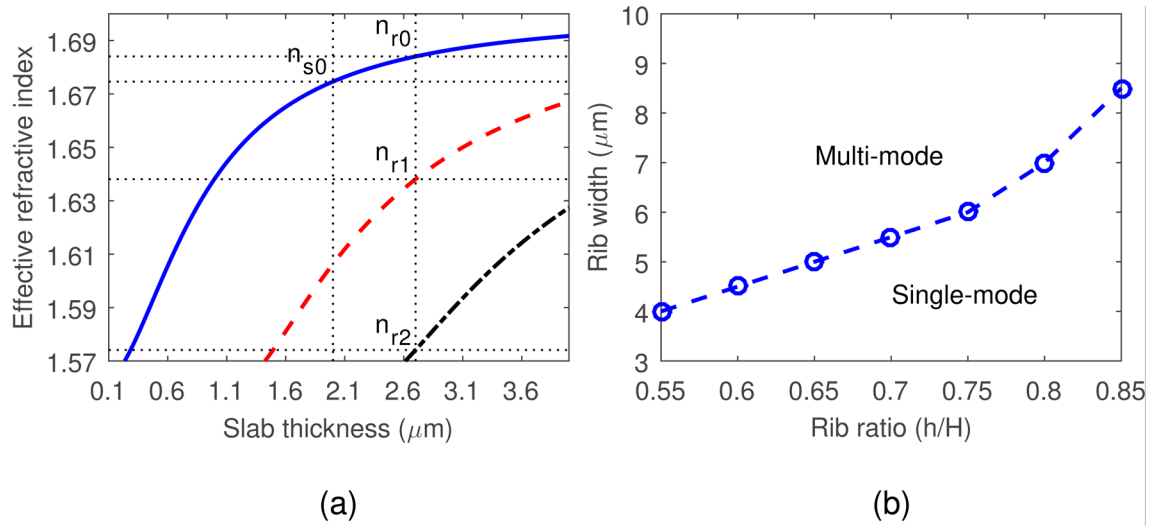


Figure 5-3 (a) Effective refractive indices of propagation modes of slab waveguide, (b) single mode criteria of rib waveguide.

5.3 Ring resonator coupling condition design

The ring resonator structure is designed to operate at critical coupling condition where the ring loss factor (α) is equal to the coupling coefficient between ring and waveguide (τ) maximizing the resonance extinction ratio [118]. The coupling coefficient (τ) is determined by the coupling area between ring and waveguide and the mode confinement factor. The coupling area is defined by the gap size between ring and waveguide (g) and the coupling length determined by the ring radius (R) as shown in Figure 5-2. The mode confinement factor is defined by the waveguide cross section design (W, H, h) as shown in Figure 5-1(a). However the mode confinement factor and the ring radius affect the ring loss factor (α) as well and hence α and τ are interrelated and need to be analyzed together.

The critical coupling condition number for a polymer RRM is dictated by the ring loss factor because of high propagation losses in electro-optic polymers. Initial propagation loss measurements in the fabricated straight waveguides show ~ 5 dB/cm loss yielding loss factor of 0.5 for a ring with 2 mm radius (if the bending loss is negligible). Therefore in order to reach maximum possible critical coupling condition (~ 0.6) an optimum way is to

design the ring resonator with negligible bending loss and adjusting other dimensions to obtain τ as close as possible to α .

To initiate the design process the mode confinement factor is considered to be fixed by choosing waveguide cross section dimensions from single mode criteria. For instance $W = 3 \mu\text{m}$ is chosen according to $H = 2.7 \mu\text{m}$ core layer thickness in order to have a propagation mode shape close to circular improving fiber in/out coupling using tapered fibers. τ and α are calculated in a range of ring radii while the τ is simulated in gap sizes $1\text{--}3 \mu\text{m}$ as shown in Figure 5-4. In these simulations the structure is simulated with $r = 0.6$ from single mode criteria and ignoring propagation insertion loss. As seen in Figure 5-4 a ring with radius $>1.5 \text{ mm}$ has minimal bending loss. Gap sizes of $1.5 \mu\text{m}$ – $2 \mu\text{m}$ shows results close to the critical coupling condition with ring radius sizes (1.5 mm – 2.5 mm). In order to choose the proper gap size the fabrication process and capability must be taken into account. Achieving a gap size smaller than $1 \mu\text{m}$ is challenging on the utilized lithography machine (EVG[®] 620).

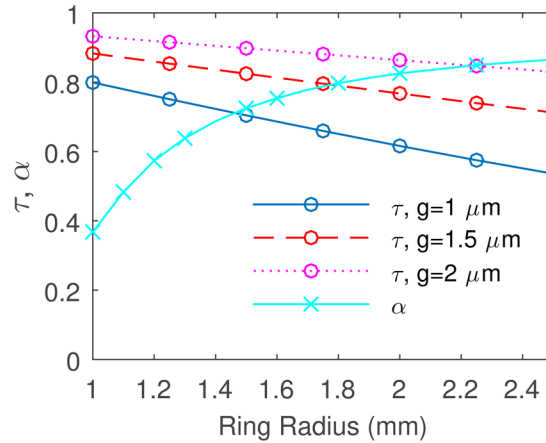


Figure 5-4 Coupling coefficient (τ) and ring loss factor (α) versus ring radius. The Solid line is for α and dashed lines are for τ with gap sizes $1 \mu\text{m}$, $2 \mu\text{m}$, and $3 \mu\text{m}$. Simulated waveguide cross section dimensions are $W = 3 \mu\text{m}$, $H = 2.7 \mu\text{m}$, and $h = 1.9 \mu\text{m}$.

To analyze waveguide cross section W and r parameters in relation to the coupling condition α and τ are simulated for three different values of W and r as shown in Figure

5-5. The performed analysis is helpful to understand the proper dimensions for critical coupling condition as well as understanding fabrication tolerance impact. As seen by increasing ring radius α is less sensitive to the changes in W and r while τ becomes more sensitive in larger ring radius. It is clear that the mode confinement factor defined by W and r plays an important role in determining α and τ . Results show the challenges in designing and fabricating a RRM with success and importance of feedbacks from fabrication process in order to tune the design parameters accordingly.

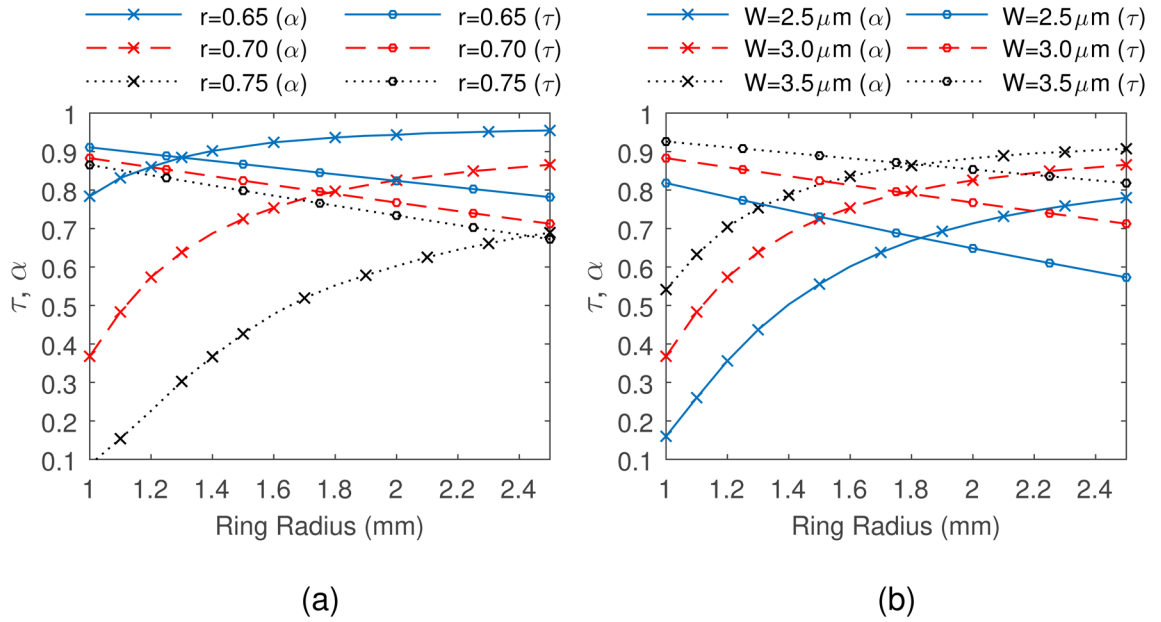


Figure 5-5 τ (dashed lines) and α (solid lines) change versus (a) rib height ratio r while $W=3 \mu\text{m}$ and (b) waveguide width (W) while $r=0.7$

After designing α and τ in separate simulations a complete ring resonator structure is simulated to check the accuracy of the simulation versus theoretical results. This step can be a preliminary step towards analyzing active RRM for MPLs through COMSOL Multiphysics package. As presented in Figure 5-6 there is a close match between theoretical and simulation and the discrepancy can be reduced by improving mesh resolution. Simulation of the complete RRM is challenging because of required computing power and memory. Special attention needs to be paid in proper meshing techniques in

order to optimize computing time as well as required resources but not to sacrifice the accuracy. To obtain the results presented

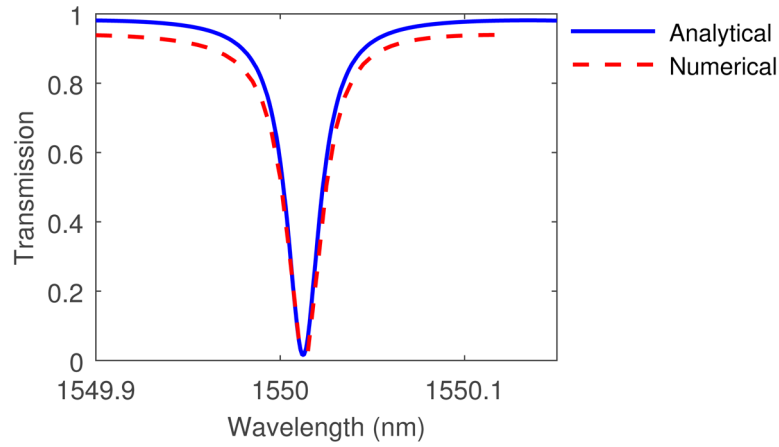


Figure 5-6 Ring resonator resonance function versus light wavelength, comparison between results obtained from analytical equation and numerical simulation.

in Figure 5-6 the number of elements is ~ 600000 which requires ~ 200 Gb memory (The computing resources required for this project is provided by Superior cluster computing at MTU). Capability of the complete RRM simulation provides the opportunity to include all characterizes of the materials as well as fabrication tolerances in obtaining modulator figure of merits for MPLs.

5.4 Optical power splitter design for DRRM

The RRM design can easily be extended to the DRRM structure discussed in Chapter 4 by adding optical power splitter as shown in Figure 5-7. The power splitter consists of S-bends and a directional coupler. The directional coupler divides the input optical power between two RRM in desired ratios while S-bend segments branch out the optical power from directional coupler to the individual RRM.

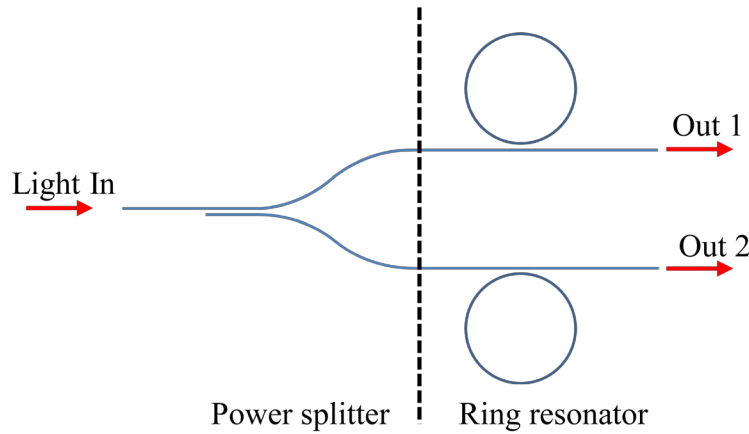


Figure 5-7 2D Optical path of DRRM divided in power splitter and ring resonator sections.

The S-bend of power splitter is designed to have minimum possible propagation insertion loss due to bending loss and material insertion loss. The bending loss is determined by the mode confinement factor and the bending radius. Since the waveguide cross section is already designed according to the ring resonator design the only remaining parameter for designing S-bend is the bending radius as shown in Figure 5-8. Increasing the bending radius decreases the bending loss however the material insertion loss must be taken into account for an optimum bending radius. For instance adding 1 mm to the bending radius adds ~ 1.2 cm to the S-bend length causing ~ 6 dB more propagation loss considering 5 dB/cm material insertion loss. A bending radius of ~ 5 mm is a compromise between material and bending losses.

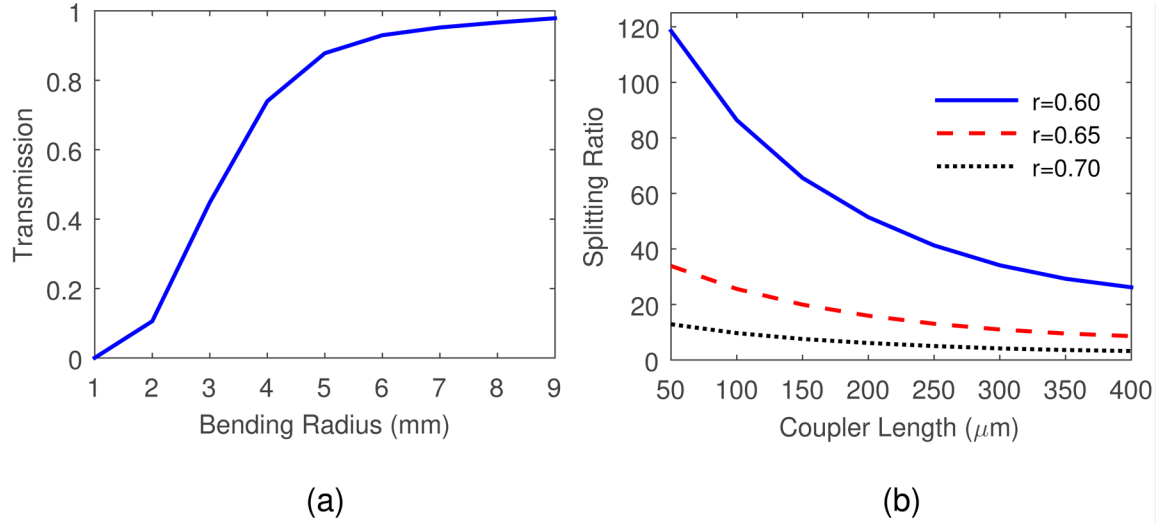


Figure 5-8 (a) Transmission of S-bend versus bending radius, and (b) Power splitting ratio versus coupling length in three rib height ratios and 5 μm gap size.

To split the optical power properly the directional coupler length and the gap size between waveguides must be determined. Figure 5-8(b) shows the power splitting ratio changes versus coupling length. The power splitting ratio is vulnerable to the waveguide cross section dimensions as shown in Figure 5-8(b) for different rib height ratios. It is worth mentioning that power splitting ratio is affected by fabrication tolerances and it could be challenging to obtain the exact power dividing ratio in the fabricated samples. By obtaining fabrication process feedback the design can be optimized to mitigate fabrication tolerances. If there is discrepancy between desired optical power dividing ratio and fabricated results, as described in the Chapter 4, the RF power dividing ratio between two modulators can be tuned in order to have correct ratio between RF power divider and optical power divider.

5.5 Summary

The RRM physical structure based on all-polymer platform is designed and optimized utilizing numerical electromagnetic solvers. Different types of available numerical methods are examined and a design procedure is developed using COMSOL BEM module

while attention is given to optimize required computing resources and time due to the structure complexity and size.

The ring resonator structure is designed to operate at the critical coupling condition using an iterative procedure in order to tune the geometrical dimensions. Properties of utilized materials and fabrication process is investigated and included in the design. It is shown that critical coupling condition number in all-polymer RRM is limited due to the high material insertion loss of electro-optic modulator. Effects of fabrication tolerances are studied showing the requirement of multiple fabrication and metrology runs in order to tune the design according to the fabrication tolerances. The RRM design process is extended to DRRM by designing optical power splitter to divide optical power between two RRM in specific ratio.

Chapter 6: Fabrication of All-polymer Electro-optic Modulation Devices

Fabrication of electro-optic polymer RRM for MPLs is challenging and there are only a couple of reported fabrication samples [73, 103]. Fabrication procedures are highly dependent upon material properties and the majority of electro-optic polymer materials are still in the research stage [68, 69] and not well documented in the literature causing difficulties in accessing material sets and developing fabrication procedures.

A fabrication process is developed to fabricate electro-optic modulators on an all-polymer platform. Research and characterizations are conducted on commercially available materials for core and cladding layers and a set of materials are identified that are compatible according to materials properties and fabrication process. A feasible fabrication process on the selection of material set is developed by examining different types of fabrication process. RRM, and DRRM structures are fabricated and physical dimensions are characterized using metrology techniques. A summary of faced challenges and identified solutions are documented while more details are given in Appendix 1.

6.1 Material selection

Limited types of electro-optic polymer materials were identified to be commercially available at the time of this project. Initially a polymer compound named as DR1-PMMA was found to be commercially available [149, 150]. DR1-PMMA is a guest-host type electro-optic polymer consisted of dispersed red-1 (DR1) chromophore synthesized in a host polymer of polymethylmethacrylate (PMMA). Initially DR1-PMMA was commercialized by IBM [75, 149] however currently DR1-PMMA is available through Sigma Aldrich and Specific Polymer companies. DR1-PMMA has modest electro-optic coefficients of ~ 12 pm/V [75, 149] while recently an electro-optic coefficient of ~ 60 pm/V has been reported using DR1-PMMA from Specific Polymer [150]. Initially in this project

the DR1-PMMA from Specific Polymer was characterized as described in Appendix however the thin-film deposition process could not yield a uniform layer. It is worth continuing the work on DR1-PMMA in the future since it is relatively an accessible and a low cost electro-optic polymer material.

Recently high performance electro-optic polymer materials have been commercialized by Soluxra LLC. A polymer compound named SEO100C is chosen which is a guest-host type electro-optic polymer with chromophores doped into the host polymer of polycarbonate (PC). High electro-optic coefficients of 140 pm/V have been reported using SEO100C [150-152]. A successful fabrication process was developed using SEO100C as described in Section 6.2.

Among various types of polymer materials that can be utilized as cladding layers NOA73 from Norland Products Inc. is identified as a compatible cladding material for SEO100C in terms of optical/electrical properties and fabrication process. Refractive indexes of SEO100C and NOA73 are measured using ellipsometry as 1.7 and 1.55 respectively. NOA73 can be fabricated in thin films with acceptable uniformity and surface roughness. Solvents in NOA73 do not damage SEO100C and the temperature and UV energy needed for NOA73 curing process is within the toleration limits of SEO100C. The resistivity of cladding layers is a crucial factor affecting the electro-optic polymer poling process outcome as well as modulation efficiency [153, 154]. The resistivity of NOA73 is measured as $\sim 3 \times 10^{10}$ (135°C) which is in the same order of SEO100C resistivity $\sim 3.3 \times 10^{10}$ at 135°C [155]. The stack of NOA73/SEO100C/NOA73 is strong enough that can go through post fabrication steps of end-facet preparation and measurements.

6.2 Fabrication Procedure

A developed fabrication process is summarized in Figure 6-1 and more details of the fabrication process are given in Appendix. The fabrication procedure can be divided in three critical sections that are: thin film deposition, rib waveguide patterning, and electrode

fabrication. Devices are fabricated in a clean-room on silicon wafers after standard RCA cleaning.

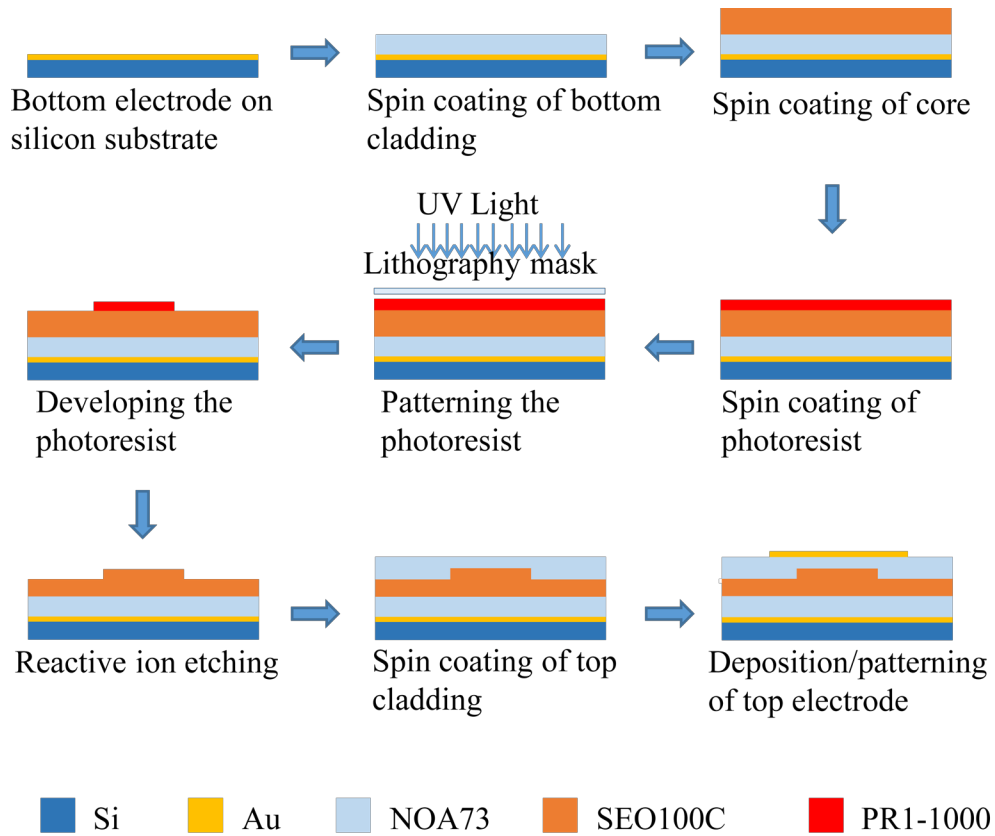


Figure 6-1 Schematic of fabrication steps for all-polymer electro-optic modulator.

Thin films of NOA73 are deposited by spin coating followed by UV radiation curing and thermal baking. NOA73 comes in liquid form and it is ready to spin coating without further treatment. The spin speed/film thickness curve is obtained for NOA73 as shown in Figure 6-2 and $\sim 4 \mu\text{m}$ thin film is deposited at 3000 spin speed.

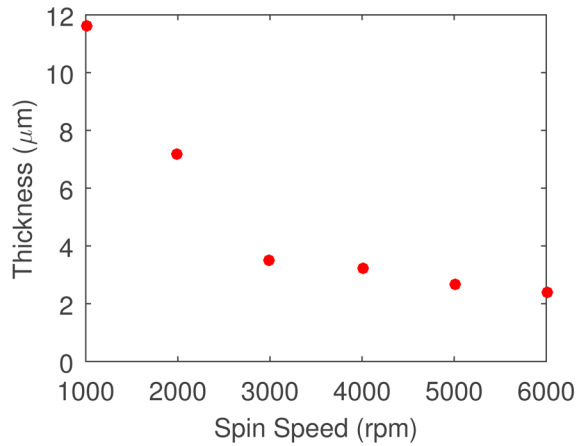


Figure 6-2 Thickness of NOA73 thin film versus spin coating speed.

The curing step of NOA73 layer is crucial in setting the surface roughness, the thin rigidity, and the adhesion. It was determined that NOA73 is sensitive to the UV exposure power and high power UV exposure causes serious damages to the thin film uniformity as shown in Figure 6-3. Lowering the UV exposure power while increasing the UV exposure time solves the problem as detailed in Appendix. In addition the top cladding layer of NOA73 needs to be hard baked otherwise the top electrode metal deposition step using e-beam evaporation technique results in cracks on top cladding as seen in Figure 6-4. On the other hand the hard baking of lower cladding layer weakens the adhesion between lower cladding and core layers causing delamination in dicing step and hence the hard baking step for lower cladding layer is to be avoided.



Figure 6-3 Microscope image of NOA73 thin film surface after high power UV exposure.

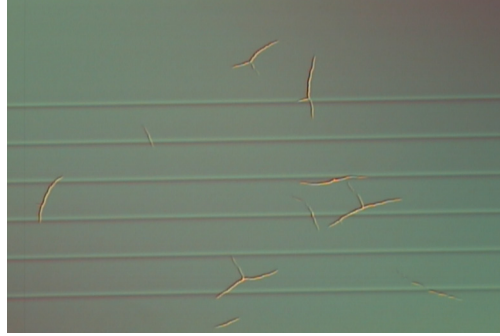


Figure 6-4 Microscope image of the top cladding layer surface after gold deposition for top electrode fabrication.

The thin film of SEO100C is fabricated using spin coating and hard baking inside a vacuum oven. SEO100C comes in powder and solutions of SEO100C is prepared according to the manual provided by Soluxra LLC. The SEO100 powder is mixed with Dibromoethane at the mass ratio of 7%. The powder is dissolved thoroughly in to the solvent using a rotator mixing the solution overnight. The solution is then filtered using 200 nm pore size filter and after 30 min rest time the solution is ready for spin coating process. A $\sim 2.7 \mu\text{m}$ film thickness is achieved at 1000 rpm spin speed. The film is baked inside vacuum oven at 75°C overnight.

The rib waveguide patterning step in SEO100C thin film is a crucial step which is conducted by the UV lithography technique followed by a dry etching step as shown in Figure 6-1. The reactive ion etching (RIE) technique with Oxygen is used as detailed in Appendix 1. Etch rates of SEO100C thin film are measured as shown in Figure 6-5. The PR1-1000 positive photoresist from Futurex was identified to be a proper photoresist. PR1-1000 does not interact with SEO100C and solvents in PR1-1000 are compatible with SEO100C. PR1-1000 can be deposited in a thin layer ($\sim 2 \mu\text{m}$) uniformly and it is suitable to pattern features as small as $1 \mu\text{m}$. PR1-1000 withstands the etch process to transfer the pattern to SEO100C thin film.

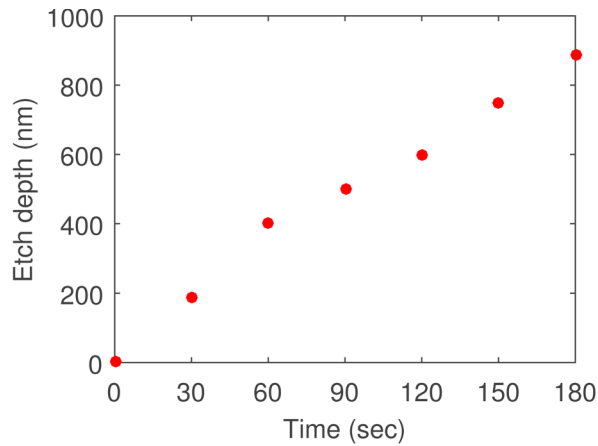


Figure 6-5 Etch rates of SEO100C thin film.

The bottom electrode is fabricated using sputtering technique to deposit 10 nm Cr layer followed by 100 nm Au layer. The Cr layer is used to increase the Au layer adhesion to the silicon wafer. The top electrode is deposited using electron-beam physical vapor deposition (EBPVD) technique similar to the bottom electrode in 10 nm Cr and 100 nm Au layer. To pattern top electrode common Au/Cr wet etching is utilized (Appendix 2). To open windows for accessing the bottom electrodes the RIE Oxygen etching is used (Appendix 2).

Fabricated structures were analyzed using atomic force microscope (AFM) and optical microscope as shown in Figure 6-6 and Figure 6-7 respectively. Results show that the developed fabrication process can pattern features with acceptable fabrication tolerance while there is still room to optimize the fabrication process and minimize the tolerances.

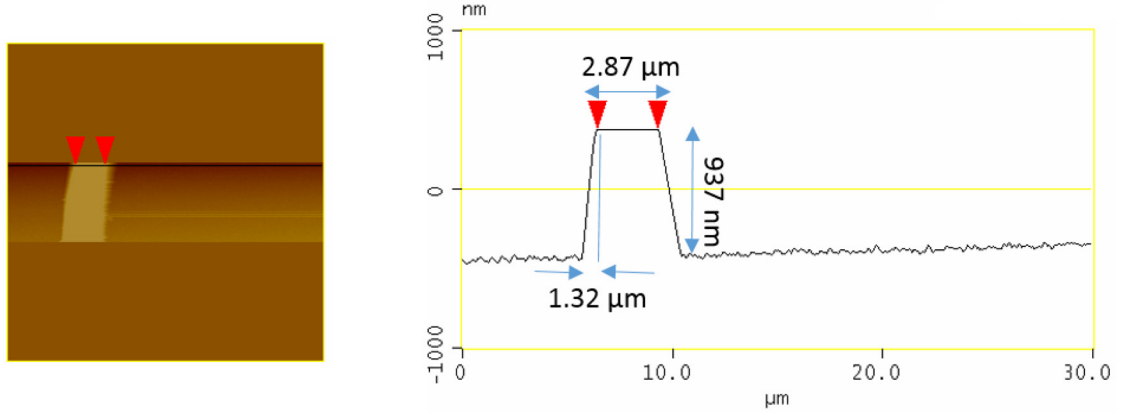


Figure 6-6 AFM measurement of the rib waveguides fabricated on SEO100C

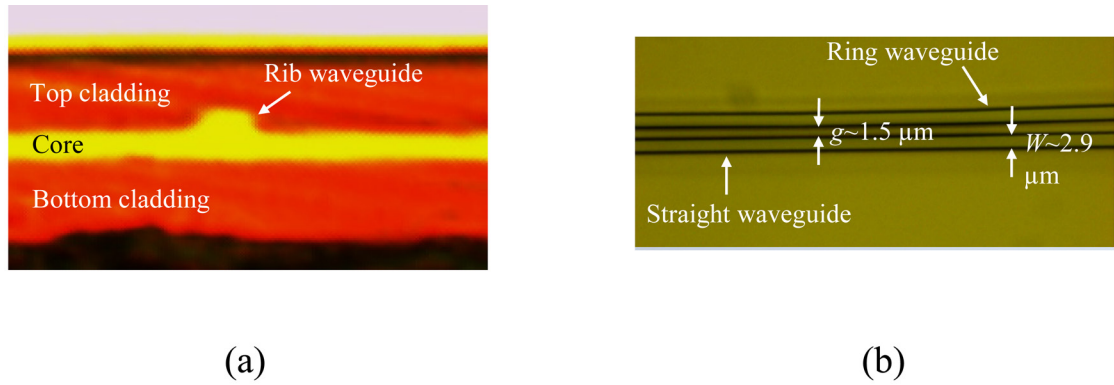


Figure 6-7 Images using optical microscope of a rib design patterned on SEO100C (a) Cross section image of rib waveguide, (b) top view of ring and waveguide at the coupling area.

Complete structures of electro-optic modulators were successfully fabricated on a 4 inch silicon wafer as shown in Figure 6-8. Individual samples are separated from the wafer and are taken through poling and measurement processes as described in Chapter 7. To test device samples a butt-coupling technique is utilized to couple light from an optical fiber into and out of the waveguides requiring the end-facet of waveguides to be as free from imperfection as possible to minimizing the coupling loss. A dicing saw is used for preparing device samples on end-facets see Appendix for further details. Methods such as cleaving and polishing fail to provide clear end-facets due to the lack of crystalline symmetry and low rigidity of polymer layers. The quality of end-facets are improved by

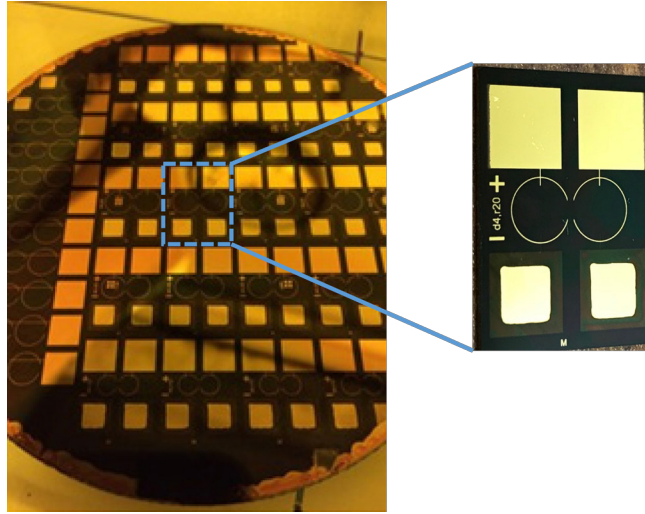


Figure 6-8 Fabricated RRM and DRRM using SEO100C material on 4 inch silicon wafer.

lowering the longitudinal cut speed during dicing. In addition a layer of photoresist such as PR1-1000 is used as a protective layer minimizing the damage caused by the dicing saw to the polymer structure. Removal of the photoresist also serves to clean the end-facets after the dicing.

6.3 Summary

A complete fabrication procedure is developed for an all-polymer electro-optic modulator structures using commercially available polymer materials. Commercially available electro-optic materials are characterized and SEO100C from Soluxra LLC is utilized for the core layer. NOA73 is identified to be a compatible cladding material for SEO100C based on optical/electrical properties and fabrication process. Complete structures of RRM and DRRM are successfully fabricated and examined using metrology techniques including the optical microscope and AFM showing close agreement between fabricated and designed geometrical dimensions.

Chapter 7: RRM Characterizations

In MPLs where the modulator linearity is a prominent factor, the theoretical studies presented in Chapter 3 have shown that the Lorentzian transfer function of RRM improves the SFDR of MPLs versus the sinusoidal transfer function of MZI modulators. The resonance characteristic of RRM yields enhanced modulation index as well compared to MZI modulators improving gain and noise figure of MPLs as described in Chapter 2. The RRM advantage of enhanced modulation index is less susceptible to microwave electrode loss and phase velocity mismatch factors at high frequencies that commonly perturb MZI operation. The resonance characteristics of RRM repeats at multiples of FSR while with a limited bandwidth and hence RRM are promising candidates for applications which require modest bandwidth (a few GHz) while operated at high frequencies > 50 GHz such as MPL applications of wireless access networks as described in Section 3-7.

RRM can be fabricated on various platforms including silicon [115, 124], polymers [73, 103], and hybrid materials [137, 156, 157]. Polymers are platform candidates for advanced generations of high-speed electro-optic modulators. The frequency bandwidth of electro-optic response in polymers is up to millimeter frequency ranges [149]. In addition polymers pose low refractive index differences in microwave and optical frequencies minimizing the velocity mismatch factor which enhances the modulator operational bandwidth [73]. Polymers can have considerably high electro-optic coefficients > 100 pm/V making polymer suitable to improve modulator sensitivity [69]. The spin coating capability of polymers provides relatively easier fabrication process of thin films which can be spin coated on top of other types of materials such as silicon forming hybrid platforms [137, 156].

Despite all-polymer RRM promising advantages, implementation of all-polymer RRM to surpass other modulator structures for MPL applications are limited to a few reported samples. Reported RRM have been examined in terms of modulation index while the

RRM linearity for the analog signal modulation has not been studied thoroughly and validated with experimental results.

Fabricated all-polymer RRM s are characterized in terms of the resonance since the resonance function of ring resonator structure has detrimental impacts on RRM functionality including modulation index and operational bandwidth. The resonance is characterized by testing RRM s in the passive form (no electrical signal applied). The resonance figure-of-merits including resonance extinction ratio, resonance bandwidth, and FSR are measured. The ring-waveguide coupling coefficient and the ring loss factor are calculated according to the measured resonance figure-of-merits. Resonance characterizations of RRM s show successful design and fabrication processes described in Chapters 5 and 6 while providing valuable feedback from fabrication tolerances and design parameters that can be utilized for next generation of devices.

Fabricated all-polymer RRM s are shown to be functional in the active mode by applying electrical signal to devices testing the modulation index. Electro-optic coefficient of the polymer is characterized through the modulation index of the RRM. The realization of all-polymer RRM shows success in the developed all-polymer platform as well as fabrication and poling processes.

Targeting RRM implementations in RF photonic links the nonlinearity of analog signal modulation is characterized through Harmonic distortions and SFDR. Suppression of the harmonic distortions at specific operational points of the RRM Lorentzian transfer function, as described in Chapter 3, is experimentally proven. The third harmonic distortion behavior shows the unique capability of RRM s in enhancing microwave photonic links SFDR in terms of third order intermodulation distortion (IMD3). The SFDR of RRM is measured and compared to theoretical results and roots of discrepancies between theory and experiments are discussed.

7.1 Resonance

The transmission spectrum of ring resonator structures in optical domain is critical for evaluating fabricated RRM. The transmission spectrum reveals the resonance behavior of ring resonator extracting the resonance characteristics including resonance bandwidth, FSR, resonance extinction ratio, and ring-waveguide coupling condition. The resonance have detrimental impacts on RRM system level figure-of-merits including operational bandwidth, operational frequency, modulation index, and linear operational point as discussed in Chapter 3.

The resonance function of ring resonator structures is characterized utilizing the test setup shown in Figure 7-1. A tunable laser source with 1 pm wavelength resolution in the range of 1480-1580 nm is coupled into and out of the waveguides using lensed fibers with $2.5 \pm 0.5 \mu\text{m}$ mode diameter at focal distance $14 \pm 2 \mu\text{m}$. Polarization of light is controlled using manual paddle polarization controller.

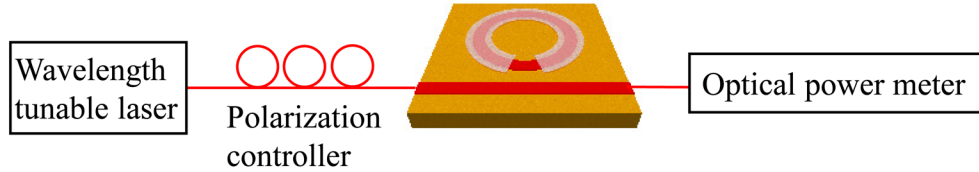


Figure 7-1 Measurement setup used for passive characterizations of RRM.

The transmission spectrum of the ring resonator with a 2.5 mm radius is shown in Figure 7-2. The measured FSR is $\sim 85 \text{ pm}$ which is compared to the theoretical FSR calculated using Equation (7.1) [113]

$$FSR \approx \frac{\lambda^2}{n_{eff} L} \quad (7.1)$$

where λ is the light wavelength, n_{eff} is the effective refractive index of propagation mode, and L is the ring perimeter [113]. The effective refractive index of propagation mode n_{eff} is

calculated as 1.67 using Comsol mode solver as described in Section 5.2 where the core refractive index is 1.7 and the cladding refractive index is 1.54. The theoretical FSR for a 2.5 mm ring radius at 1550 nm wavelength is 91 pm which is in agreement with measured results. The discrepancy between measured and theoretical FSRs is due to the n_{eff} tolerances due to either tolerances in the waveguide cross section dimensions or in the material refractive indexes. The FSR is 11 GHz in the frequency domain showing that fabricated RRM can be operational at multiples of 11 GHz if traveling-wave electrode is utilized to remove electrode related bandwidth limitations of photon transit time and electrode capacitance effects as described in Section 3.2.

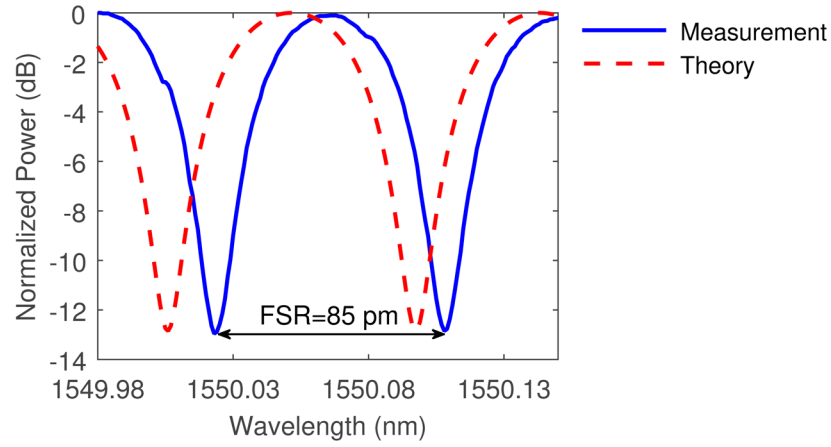


Figure 7-2 Measured transmission spectrum of a fabricated ring resonator.

The resonance line-width is characterized using full-width half maximum (FWHM) measured as ~ 35 pm. The FWHM of the passive ring resonator determines the 3 dB bandwidth of the ring resonator filtering property as 4.4 ± 0.2 GHz. Besides FWHM and FSR the loaded Q-factor defined as $\lambda/FWHM$ and the resonance fineness defined as $FSR/FWHM$ are used to describe the sharpness of the filtering property of ring resonators. Fabricated ring resonators present loaded Q-factor of 4400 ± 500 and resonance fineness of 2.4 ± 0.15 . It is worth mentioning that a higher Q-factor or fineness of resonance yields higher modulation index in RRM while decreases the operational bandwidth of RRM.

The operational bandwidth of RRM can be calculated from passive response of RRM. The 3 dB bandwidth of modulation index in RRM is calculated using Equations (7.2) and (7.3) [121]

$$T_f = 2T_p = \frac{2n_{eff}L}{c(1-\tau^2)} \quad (7.2)$$

$$f_{3dB} = \sqrt{\sqrt{2}-1} \frac{1}{2\pi T_f} \quad (7.3)$$

where T_p is the photon transit time around the ring and τ is the ring-waveguide coupling coefficient. The fabricated ring-waveguide coupling condition is calculated by fitting the measured optical transmission spectrum (Figure 7-2) to the ring resonator transfer function of Equation (2-7). Fabricated RRM operates at a coupling condition with $\alpha \sim 0.31$ and $\tau \sim 0.44$ showing the under-coupling situation ($\tau > \alpha$). Using measured n_{eff} (1.65) and τ (0.44) the 3 dB modulation index is calculated as 450 MHz using Equations (7.2) and (7.3). For MPLs the operational bandwidth of SFDR is more limited than the modulation index bandwidth as discussed in Chapter 3. By modeling the fabricated RRM in a MPL described in Chapter 3 the SFDR bandwidth is ~ 350 MHz in order to have SFDR > 110 dB (1 Hz noise bandwidth). The operational bandwidth of fabricated RRM are limited mainly due to the large size of rings. Decreasing the ring size in the utilized material platform adds to the ring bending loss due to the relatively low refractive index differences between core and cladding materials. To design RRM with wider operational bandwidths different types of material platforms can be used to provide higher refractive index differences between core and cladding.

The ring waveguide propagation loss is calculated as ~ 6.5 dB/cm from obtained loss factor ($\alpha \sim 0.31$) using Equation (7.4).

$$Loss_{(dB/cm)} = \frac{10 \log(\alpha^2)}{L_{(cm)}} \quad (7.4)$$

Since the ring is expected to have negligible bending loss according to the simulations as described in Section 5.3 the propagation loss of ring waveguide is due to the material and surface roughness. Previous studies on different polymer waveguides have shown that the surface/sidewall roughness due to the etching process is a critical factor in propagation loss of polymer waveguides [158, 159]. The propagation loss studies of developed NOA73/SEO100C/NOA73 waveguides and investigating possible methods to decrease the loss is critical for future implantations. The impact of sidewall roughness can be mitigated by designing and fabricating shallower etched waveguides. In addition the etching procedure can be optimized to minimize sidewall roughness.

Decreasing the propagation loss in electro-optic polymer modulators is beneficial in designing RRM. The ring structure and fabrication procedure can be optimized to achieve ring-waveguide coupling conditions closer to the critical coupling conditions in order to maximize the resonance extinction ratio. However as shown here and Chapter 5 the coupling condition in polymer RRM is dictated by the ring loss factor and the range of achievable critical coupling conditions is limited due to the high propagation loss of fabricated waveguides.

7.2 Modulation index

The modulation response of fabricated RRM is tested utilizing the test setup shown in Figure 7-3. Tests are conducted at 1550 nm by applying a triangular electrical voltage with 20 V_{pp} and a 2 second period as shown in Figure 7-4(a).

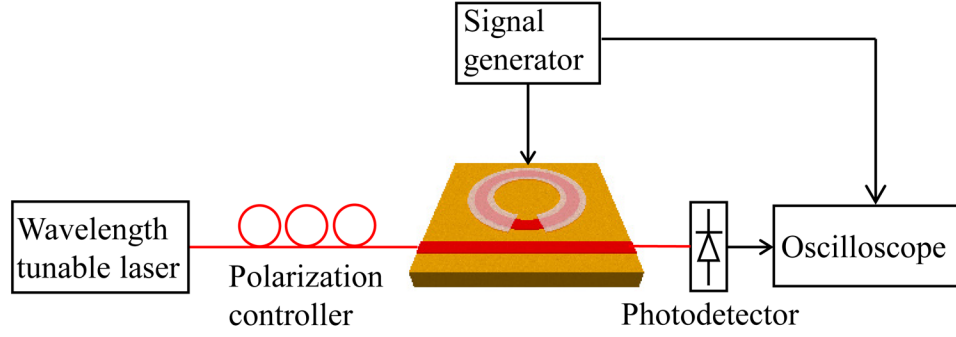


Figure 7-3 Measurement setup used for modulation response of RRM.

The RRM transmission in the response of the applied voltage is shown in Figure 7-4(b). As seen in Figure 7-4(b) the voltage amplitude of 20 V transfers the ring resonator state from out of the resonance state to the resonance state meaning a π radian phase shift in the round trip phase (θ) according to Equation (3.1). Based on Equation (3.1) the electro-optic coefficient of the polymer is calculated from Equation (7.5).

$$r = \frac{\lambda g}{Ln_{eff}^3 \Gamma V} \quad (7.5)$$

The electro-optic coefficient is calculated as ~ 84 pm/V. To calculate the electro-optic coefficient (r) the utilized parameters are $\lambda = 1550$ nm, $g = 2.7$ μ m (thickness of core layer), $L = 0.0143$ (m) (perimeter of the ring with electrode), $n_{eff} = 1.65$ (measured effective refractive index of mode), $\Gamma = 1$ (electrical-optical overlap integral), and $V = 3$ (volt). The voltage (V) that brings ring resonator from out of resonance state to the resonance state is the voltage applied across the 2.7 μ m of core layer. V is calculated from total applied voltage (20 volt) and using measured resistivity values of core and cladding layers as $\sim 3.3 \times 10^{10}$ (135°C) and $\sim 3 \times 10^{10}$ (135°C) respectively [155].

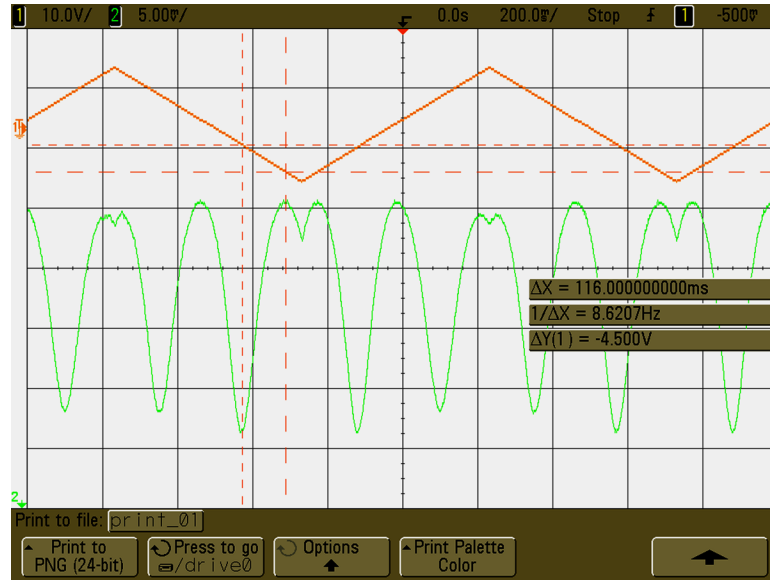


Figure 7-4 The modulated light with a triangular electrical signal.

Measured RRM s are polled by applying 800 (V) using a contact poling process developed for electro-optic polymer modulators [155]. Utilized poling process is critical for the measured electro-optic coefficient. Crucial parameters in the poling process are the applied voltage and device temperature to align chromophore dipoles efficiently in the direction of applied voltage. In the poling process, devices are heated to 135°C while applying voltage.

7.3 Analog modulation

The analog modulation of RRM is characterized by measuring harmonic distortions and SFDR. Harmonic distortions are measured by applying a 20 KHz signal to the RRM and the output signal of the photodetector is amplified and recorded using a Lock-in amplifier as shown in Figure 7-5. To show the harmonic power suppressions versus the RRM Lorentzian transfer function the optical wavelength is swept around 1550 nm in 1 pm resolution.

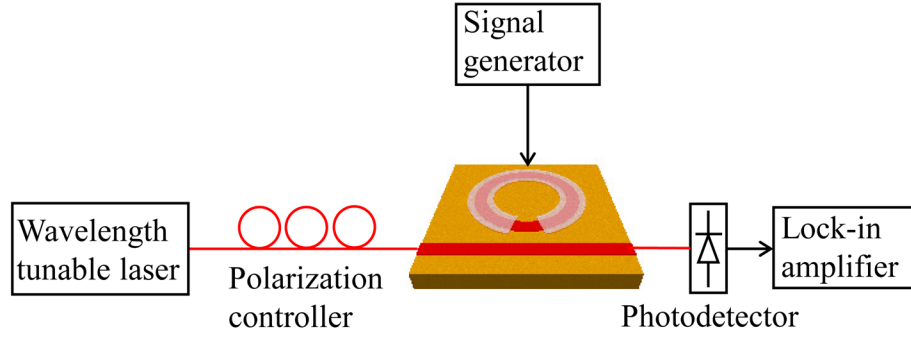


Figure 7-5 Measurement setup used for harmonic characterizations of RRM.

Results presented in Figure 7-6 show that second harmonic is suppressed at λ_1 while third harmonic is suppressed at 11 pm apart from λ_1 as shown by λ_2 in the figure as theoretical studies described in Chapter 3 have shown. The optimum operational point of Lorentzian transfer function occurs at λ_2 to maximize the SFDR for RRM while λ_1 can be exploited in dual ring resonator modulator (DRRM) to maximize the SFDR for IMD3 and 2nd harmonic as discussed in Chapter 4.

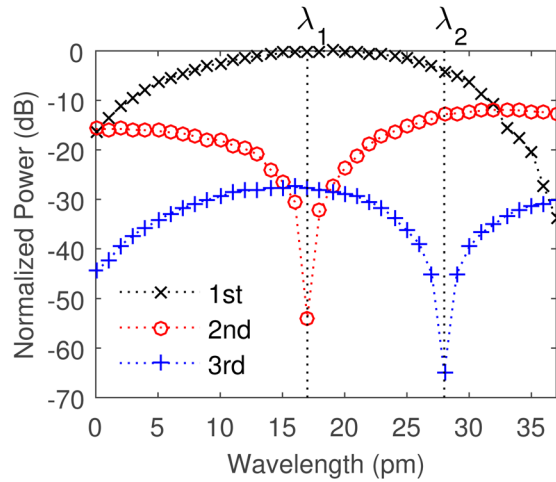


Figure 7-6 Harmonics power versus wavelength for a RRM with 2.5 mm radius.

To characterize the SFDR of a MPL with RRM a two tone test with 1 MHz and 0.950 MHz is applied to the RRM and optical wavelength is set to λ_2 as shown in Figure 7-7.

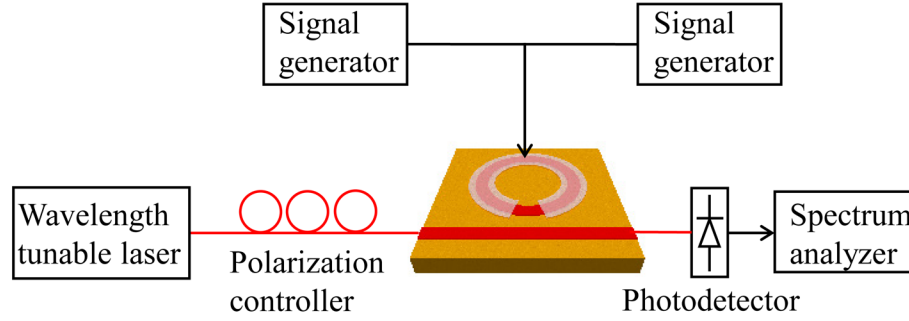


Figure 7-7 Measurement setup used for SFDR measurements.

The powers of fundamental signal and third order intermodulation (IMD3) are measured using RF spectrum analyzer in several input RF powers as presented in Figure 7-8 where the measured SFDR is ~ 74 dB considering -165 dBm noise level. In the measurements the noise level on the spectrum analyzer is limited to -130 dBm in 1 MHz frequency range however it is a common practice to report SFDR based on the noise level achievable in MPLs [7].

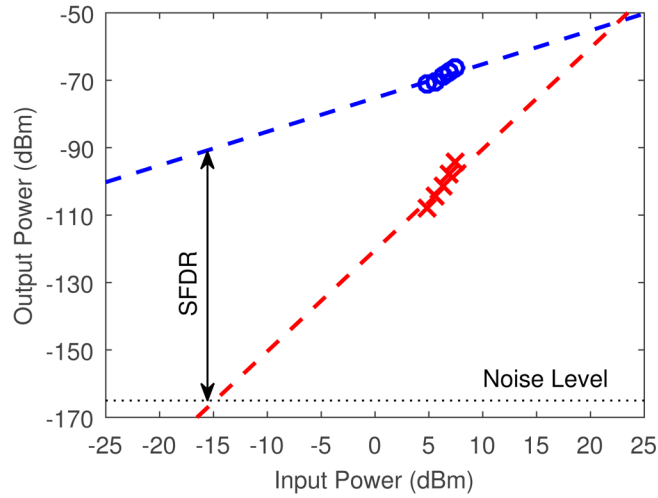


Figure 7-8 RF output fundamental signal and IMD3 powers versus input RF power.

To compare measured SFDR with theoretical SFDR the RRM is modeled in a MPL yielding SFDR of ~ 93 dB according to 1 pm optical wavelength resolution and -12 dBm optical input power to the photodetector. RRM requires wavelength locked operation

however the vulnerability to the wavelength tolerance can be mitigated by increasing the resonance bandwidth as well as controlling the bias voltage. To increase resonance bandwidths, rings with smaller sizes can be designed by having higher refractive index differences between core and cladding layers and platforms such as polymer-silicon hybrid platform can be considered for future advancements [10]. Moreover to reach theoretical SFDR of > 120 dB (1 Hz noise bandwidth) requires 10 dBm optical power at the photodetector which requires using laser power of 20 dBm and considering 10 dB modulator insertion loss as used in theoretical studies described in Chapters 3 and 4. Therefore decreasing modulator insertion loss while utilizing high optical power is necessary in future studies.

7.4 DRRM characterizations

Similar to RRM characterizations, ring resonators on DRRM are characterized in passive form utilizing a tunable laser as shown in Figure 7-9. Output power of each ring resonator is measured separately. Ring resonators show close optical output power spectrum versus wavelength as seen in Figure 7-10. FSR of resonances are measured at 85 ± 2 pm and FWHM are measured at 35 ± 2 pm. Coupling conditions are measured with $\alpha = 0.32 \pm 0.05$ and $\tau = 0.45 \pm 0.05$. Achieving close optical properties from two rings is promising for DRRM full implementation in MPLs.

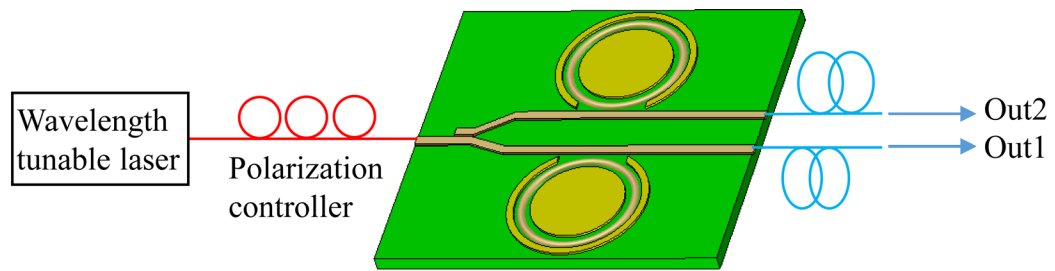


Figure 7-9 Measurement setup for DRRM.

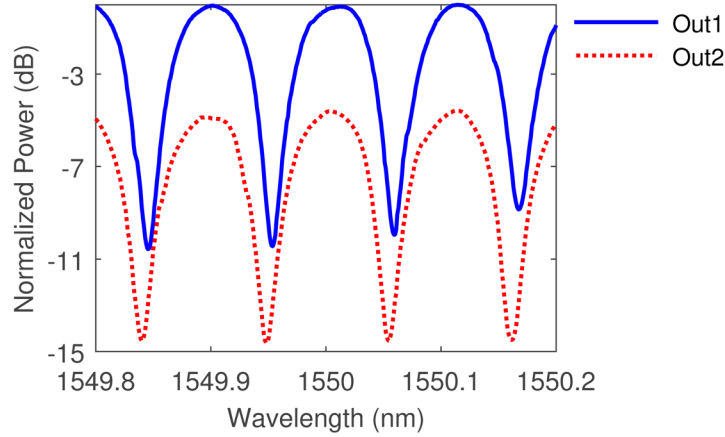


Figure 7-10 Transmission spectrums of ring resonators in a DRRM.

The optical power splitting ratio between two ring resonators is measured at 1:3 ratio while direction couplers were designed for 1:27 ratio showing a considerable discrepancy between designed and measured ratios. The power splitting ratio is affected by fabrication tolerances and it could be challenging to obtain the exact power dividing ratio in the fabricated samples. By obtaining fabrication process feedback the design can be optimized to mitigate fabrication tolerances. In full implementation of DRRM in MPLs the RF power dividing ratio between two modulators can be tuned according to the optical power splitting ratio as described in Chapter 4. However it should be intensified that a close optical splitting ratio between two RRM adds to the fundamental signal suppression degrading link SFDR, gain, and noise figure as discussed in Chapter 4.

Each RRM in a DRRM is tested separately for modulation responses. A sinusoidal signal with 1 (V_{pp}) and 1 Hz frequency is applied to RRMs. The RRM which receives higher optical power provides signal with larger amplitude as shown in Figure 7-11. By having π radian phase difference between applied electrical signal between two RRM the π radian phase difference is also produced between outputs showing the capability to subtract the outputs in order to suppress IMD3 power. In full implementation of DRRM an optimum way is to utilize balanced photodetectors in order to subtract signals.

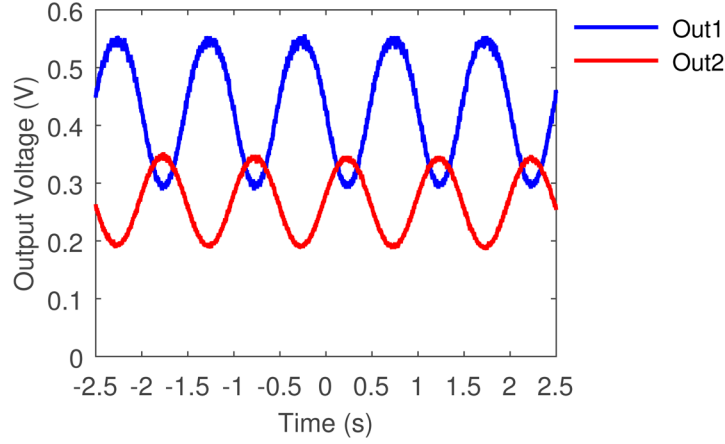


Figure 7-11 Modulation function of each RRM in DRRM.

While fabricated DRRMs are characterized in both passive and active forms, in order to fully characterize DRRMs showing IMD3 suppression the outputs of RRM need to be detected simultaneously. In addition, RF power between two rings need to be divided precisely with ± 0.01 dBm tolerations as discussed in Chapter 4. Dividing RF signal with high accuracy is challenging while can be achieved utilizing integration techniques to minimize the fabrication and application tolerances.

7.5 Summary

Fabricated all-polymer RRM are characterized showing ~ 13 dB resonance extinction ratio and ~ 4400 Q-factor. The over-coupled condition is measured by $\alpha \sim 0.31$ and $\tau \sim 0.44$ coupling conditions. The coupling condition is able to be improved by adjusting the fabrication process taking into account the fabrication tolerances and material properties. The loss factor of ring presents ~ 6.5 dB/cm of propagation insertion loss in waveguides due to the material insertion loss and scattering loss of surface roughness. The measured electro-optic r_{33} is ~ 84 pm/V using contact poling which can be improved by optimizing the poling process.

The analog signal modulation is characterized by measuring harmonic distortion powers and SFDR measurements for IMD3. Suppressions of second and third order harmonics are

experimentally presented at specific operational points of Lorentzian transfer function as predicted by theoretical studies. The third harmonic distortion is suppressed by ~ 37 dB while fundamental signal is degraded by ~ 4 dB showing the unique advantage of RRM to enhance SFDRs of MPLs in comparison to MZI modulators. SFDR of 74 dB at -165 dB noise level is measured. To further improve the SFDR utilizing high power laser while reducing RRM insertion loss is proposed for future work. In addition the vulnerability of RRM linearity is shown versus the operational point of Lorentzian transfer function showing the requirement of wavelength locked lasers for RRM. Operational point vulnerability can be mitigated by designing the ring resonator with wider resonance bandwidths and controlling the operational point using dynamic controlling of bias voltage.

Fabricated DRRMs are characterized in passive and active forms. Ring resonators in DRRM show close optical transmission spectrum with close resonance behaviors. Testing of DRRMs by each RRM separately in active form show feasibility of the device and provide necessary fabrication feedback for next generation of devices.

Future work

This research has substantial progress in advancing RRM for microwave photonic applications through the design, fabrication, testing, and operation. Considerable amount of research and improvement remains on both materials and structures in order to fully implement RRM in practical applications.

The linearity of RRM is proved to surpass the MZI modulator, the RRM linearity is shown to be sensitive to the operational point of the transfer function. The level of sensitivity is related to the designed ring resonator structure and the utilized material sets. The fabricated all-polymer RRM is shown to require 1 pm accuracy in the optical wavelength in order to exploit the high SFDR of RRM. While controlling the optical wavelength in that accuracy could be challenging, the operational point of the transfer function can be controlled using other mechanisms such as bias voltage adjustment or thermal effects. Investigating an applicable method to control operational point of RRM is critical for future advancements.

The optical power that RRM can sustain is an important factor in improving RRM figure-of-merits including gain, noise figure, and SFDR. As discussed in Chapter 7 in order to reach a SFDR > 125 dB/Hz in a MPL with RRM the input optical power of photodetector needs to be in the level of 10 dBm which can be achieved by 20 dBm optical power into the RRM considering 10 dB insertion loss. Polymer modulators can be vulnerable to high optical powers depending on the utilized material platform. The optical power tolerance of developed modulator platform needs to be determined. An insertion loss of 10 dB is challenging in the fabricated modulators due to the high propagation loss and fiber-waveguide in/out coupling loss. Decreasing the RRM insertion loss is critical for future implementations. The surface/sidewall roughness due to the etching process is a crucial factor in propagation loss of fabricated polymer waveguides. Investigating the impacts of etching process on the sidewall roughness and optimizing the etching process is important to minimize the propagation loss of developed modulators. In addition in polymer RRM

the coupling condition is dictated by the ring loss factor due to the high propagation loss in electro-optic polymer materials as discussed in Chapter 7. Decreasing propagation loss of electro-optic polymer can improve the coupling conditions in RRM.

While impacts of ring-waveguide coupling condition tolerances on SFDR is mitigated by optimizing the operational point of RRM, the coupling condition tolerances can decrease modulation index degrading gain and noise figure. Critical coupling conditions are the best conditions to obtain maximum resonance extinction ratio, however, obtaining critical coupling condition is challenging due to the fabrication tolerances. Investigating tolerances of coupling conditions due to fabrication tolerances is beneficial.

It is worth mentioning that most of RRM characteristics are determined by the utilized material sets. Electro-optic polymers have unique advantages such as wide bandwidth and high electro-optic coefficient, however electro-optic polymers are still in the research stage. To advance electro-optic polymer implementations improvements are required on the issues of optical power handlings and temperature tolerations. Recent progress on electro-optic polymers have shown promising advancements in optical power tolerations of 100 mw and operational stability up to 85 C [74, 76]. Investigating the operational dependence of developed modulators on optical power and temperature is critical for future implantations.

In this dissertation the loss and dispersion effects of optical fiber, which connects the modulator to the photodetector, are considered negligible that is a correct assumption for relatively short fiber connections (< 1 Km) [19]. However for long-haul links the impairments of optical fiber on the microwave photonic links need to be included [20]. In addition it is critical to decrease the modulator insertion loss by minimizing the fiber waveguide in/out coupling loss through optimizing the design and end-facet preparation process.

It is valuable to investigate RRM design and fabrication on other material platforms such as silicon, III-V semiconductors, and LiNbO₃. Total insertion loss of a modulator and maximum optical power handling are critical factors in choosing the material platform. A material platform with wider range of refractive index differences between core and cladding is beneficial to realize RRM with smaller foot-prints and wider operational bandwidths. Wider operational bandwidths will also improve RRM figure-of-merit tolerations versus the transfer function operational point as discussed in Chapter 7. A material platform with lower propagation loss is also beneficial for easing constraints on designing ring-waveguide coupling conditions. While all desired characteristics would be challenging to achieve from a single material platform, materials can be used as hybrid platforms such as silicon/polymer or silicon/LiNbO₃ in order to combine advantages of different materials.

The proposed DRRM improves the operational bandwidth limits of RRM SFDR by cancelling third order harmonic distortion in a frequency independent method. However the DRRM implementation is challenging because of the dual output ports. It is worth investigating possible methods to design DRRM with single output. Another limiting factor of DRRM is the decreasing of fundamental signal degrading MPL gain and noise figure. Altering DRRM design or proposing new design that can improve SFDR without degrading gain and noise-figure is more appealing for wider range of applications. In addition DRRM is sensitive to the RF dividing ratios between two ring resonator modulator. Implementation of an active controlling system for the RF divider is an inevitable option which will add to the complexity of DRRM. Decreasing DRRM sensitivity to the RF power dividing ratio eases the implementation complexity.

Appendix

A. Dr1-PMMA thin film fabrication process

DR1-PMMA comes in powder form and needs to be dissolved in a proper solvent. Solvents with higher viscosity, lower evaporation rate are desirable to obtain uniform layer using spin coating. Several solvents are experimented as shown in Table A-1. Dioxane is shown better results in compared to other solvents. Various mixing ratios, mixing methods and optimizing the spin coating process are tested. Solutions with 10% and 15% mass ratio yield thicknesses (2-3 μm), as shown in Figure A-1. The solution with 15% mass ratio shows a better surface quality because of higher spin speed. Overnight mixing in oil bath at 70°C with magnetic bid is used. After mixing the solution is filtered using nylon type filter with 200 nm pore size. After spin coating the thin film is baked overnight in a vacuumed oven at 75 C.

Table A-1 List of the solvents used for dissolving Dr1-PMMA powder

Solvent	Viscosity (mm ² /s, 25°C)	Relative Evaporation rate (Butyl acetate = 1)	Solubility
Dichloromethane	0.15 (20°C)	27.5	✓
1-4 Dioxane	1.17(25°C)	2.7	✓
Dibromomethane	0.39(25°C)	Not available	✓

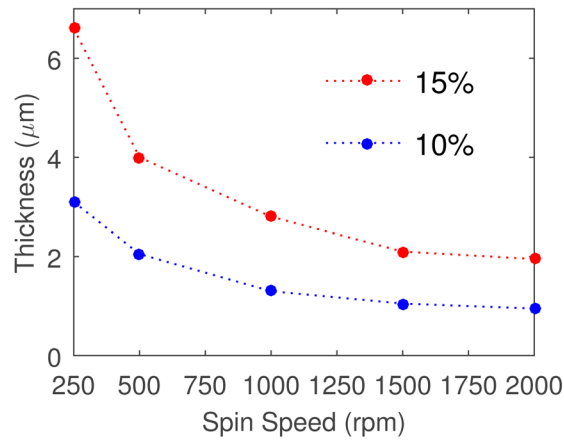


Figure A-1 Spin curves of DR1-PMMA thin film in 10% and 15% ratios dissolved in Dioxane.

To pattern DR1-PMMA the PR1805 photoresist from Shipley is a compatible photoresist. The etch rate of 15% DR1-PMMA using RIE with (Oxygen pressure: 50, ICP power: 100, and RIE power: 50) is shown in Figure A-2. Rib structures are fabricated using the developed process as shown in Figure A-3.

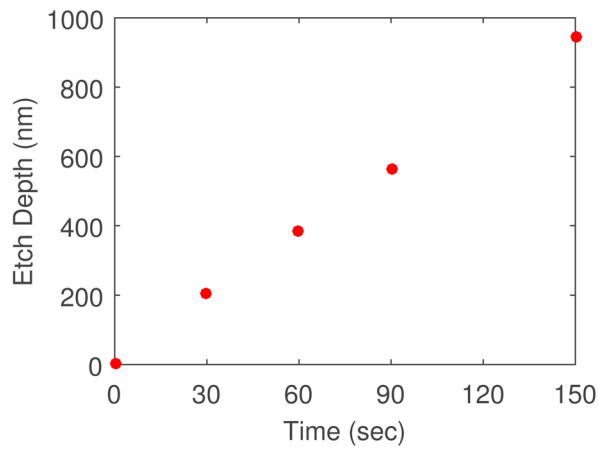


Figure A-2 Etch rates of DR1-PMMA (15%) thin film.

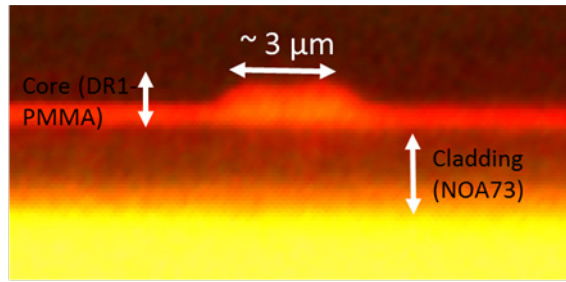


Figure A-3 Rib waveguide structure fabricated using DR1-PMMA.

Despite considerable progress in developing fabrication process using DR1-PMMA a main problem is still remained which is existence of some pinholes in thin films as shown in Figure A-4.

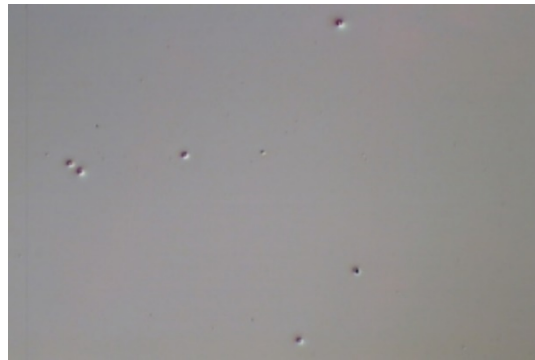


Figure A-4 Surface image, using optical microscope, of a DR1-PMMA layer.

B. Developed fabrication procedure using Soluxra SEO100C and NOA73

- Silicon Wafer: RCA cleaning process and normal cleaning process with acetone, IPA, and DI water before using the wafer
- Bottom cladding: Deposit Cr (10 nm) and Au (100 nm) using sputtering technique.
- Lower cladding layer: thin film deposition of NOA73 using spin coating:
 - Spin speed: 3000 rpm, 40 sec, static speed ($\sim 4 \mu\text{m}$ thickness),
 - Uniform UV exposure: 30 min using uniform low power UV exposure
 - The flood exposure of EV620 Lithography with $\sim 10 \text{ mW/cm}^2$ power at 350 nm wavelength caused very rough surface as shown in Figure 6-3. A UV source with much lower power ($\sim 0.3 \text{ mW/cm}^2$) at 350 nm wavelength yield a smooth thin film with low surface roughness.
 - Hard baking process of bottom cladding decreases the adhesion between the core and cladding layers causing delamination problem during dicing and sample preparation steps.
- Core layer: thin film deposition of SEO100C using spin coating
 - Spin speed: 1000 rpm, 40 sec, static speed ($\sim 2.7 \mu\text{m}$ thickness)
 - Hard baking: over-night under vacuum at 75 C
- Photoresist: type PR1-1000A Futurex
 - Spin speed: 1500 rpm, 40 sec
 - Prebake: hotplate 30 sec at 120 C
 - UV exposure: 120 mJ using EM620 aligner
 - Post-bake: hotplate 30 sec at 120 C
 - Develop: RD6 is used, developing time is related to the feature size: ~ 6 sec followed by DI water wash
- Etch: RIE oxygen plasma etch using
 - Oxygen pressure: 50
 - ICP power: 100
 - RIE power: 50

- Etch time: 150 sec for ~800 nm rib height
- Remove photoresist:
 - Uniform UV exposure: 30 sec using EV620 aligner
 - Developer: RD6 for 30 sec, wash with DI water
- Top clad thin film deposition similar to the bottom cladding
 - Baking: Over-night under vacuum at 75 C
- Top electrode: Deposit Cr (10 nm)-Au (100nm) using E-beam evaporation
- Top electrode patterning: Deposit PR1-1000A Futurex
 - Spin speed: 1500 rpm, 40 sec
 - Prebake: hotplate 30 sec at 120 C
 - UV exposure: 120 mJ using EM620 aligner
 - Post-bake: hotplate 30 sec at 120 C
 - Develop: RD6 ~12 sec followed by DI water wash
 - Etch: Wet etching technique
 - Gold etch: ~40 sec
 - Cr etch: ~5 sec
- Remove photoresist:
 - Uniform UV exposure, 30 sec
 - Developer: RD6 for 30 sec, wash with DI water
- Etch for bottom electrode access pads: A patterned FR4 is used for masking
 - RIE oxygen plasma etch
 - Oxygen pressure: 200
 - RF power: 100
 - Total effective etch time: 2 hours with 10 min etch steps (5 min cool down in between due to the overheating the sample)

References

- [1] T. H. Maiman, "Stimulated optical radiation in ruby," 1960.
- [2] K. Kao and G. A. Hockham, "Dielectric-fibre surface waveguides for optical frequencies," *Electrical Engineers, Proceedings of the Institution of*, vol. 113, no. 7, pp. 1151-1158, 1966.
- [3] J. Capmany and D. Novak, "Microwave photonics combines two worlds," *Nature Photonics*, vol. 1, no. 6, pp. 319-330, 2007.
- [4] S. Melle, R. Dodd, S. Grubb, C. Liou, V. Vusirikala, and D. Welch, "Bandwidth virtualization enables long-haul WDM transport of 40 Gb/s and 100 Gb/s services," *IEEE Communications Magazine*, vol. 46, no. 2, 2008.
- [5] G. Kramer and G. Pesavento, "Ethernet passive optical network (EPON): building a next-generation optical access network," *IEEE Communications magazine*, vol. 40, no. 2, pp. 66-73, 2002.
- [6] C. Kachris, K. Bergman, and I. Tomkos, *Optical interconnects for future data center networks*. Springer Science & Business Media, 2012.
- [7] R. H. Walden, "Analog-to-digital converter survey and analysis," *IEEE Journal on selected areas in communications*, vol. 17, no. 4, pp. 539-550, 1999.
- [8] C. H. Cox III and E. I. Ackerman, "Fiber-Optic Analog Radio Frequency Links," in *Broadband Optical Modulators*: CRC Press, 2016, pp. 82-111.
- [9] D. Novak *et al.*, "Radio-over-fiber technologies for emerging wireless systems," *IEEE Journal of Quantum Electronics*, vol. 52, no. 1, pp. 1-11, 2016.
- [10] H. Al-Raweshidy and S. Komaki, *Radio over fiber technologies for mobile communications networks*. Artech House, 2002.
- [11] M. Sotom, B. Benazet, A. L. Kernec, and M. Maignan, "Microwave photonic technologies for flexible satellite telecom payloads," *ECOC 2009*, 2009.
- [12] J. Capmany, B. Ortega, and D. Pastor, "A tutorial on microwave photonic filters," *Journal of Lightwave Technology*, vol. 24, no. 1, pp. 201-229, 2006.
- [13] T. E. Darcie and G. E. Bodeep, "Lightwave subcarrier CATV transmission systems," *IEEE Transactions on Microwave Theory and Techniques*, vol. 38, no. 5, pp. 524-533, 1990.

- [14] S. Pappert, C. Sun, R. Orazi, and T. Weiner, "Microwave fiber optic links for shipboard antenna applications," in *Phased Array Systems and Technology, 2000. Proceedings. 2000 IEEE International Conference on*, 2000, pp. 345-348: IEEE.
- [15] J. Capmany, J. Mora, I. Gasulla, J. Sancho, J. Lloret, and S. Sales, "Microwave photonic signal processing," *Journal of Lightwave Technology*, vol. 31, no. 4, pp. 571-586, 2013.
- [16] R. T. Schermer, F. Bucholtz, and C. A. Villarruel, "Continuously-tunable microwave photonic true-time-delay based on a fiber-coupled beam deflector and diffraction grating," *Optics express*, vol. 19, no. 6, pp. 5371-5378, 2011.
- [17] J. Yao, F. Zeng, and Q. Wang, "Photonic generation of ultrawideband signals," *Journal of Lightwave Technology*, vol. 25, no. 11, pp. 3219-3235, 2007.
- [18] X. S. Yao and L. Maleki, "Optoelectronic microwave oscillator," *JOSA B*, vol. 13, no. 8, pp. 1725-1735, 1996.
- [19] C. H. Cox, E. I. Ackerman, G. E. Betts, and J. L. Prince, "Limits on the performance of RF-over-fiber links and their impact on device design," *IEEE Transactions on Microwave Theory and Techniques*, vol. 54, no. 2, pp. 906-920, 2006.
- [20] V. J. Urick *et al.*, "Long-haul analog photonics," *Journal of Lightwave Technology*, vol. 29, no. 8, pp. 1182-1205, 2011.
- [21] T. E. Darcie, "Subcarrier multiplexing for lightwave networks and video distribution systems," *IEEE Journal on selected areas in Communications*, vol. 8, no. 7, pp. 1240-1248, 1990.
- [22] M. Nazarathy, J. Berger, A. J. Ley, I. M. Levi, and Y. Kagan, "Progress in externally modulated AM CATV transmission systems," *Lightwave Technology, Journal of*, vol. 11, no. 1, pp. 82-105, 1993.
- [23] W. I. Way, *Broadband Hybrid Fiber Coax Access System Technologies*. Academic Press, Inc., 1998.
- [24] "Wireless future drives microwave photonics," *Nat Photon*, 10.1038/nphoton.2011.292 vol. 5, no. 12, pp. 724-724, 12//print 2011.
- [25] M. Sauer, A. Kobayakov, and J. George, "Radio over fiber for picocellular network architectures," *Journal of Lightwave Technology*, vol. 25, no. 11, pp. 3301-3320, 2007.
- [26] K. Xu *et al.*, "Microwave photonics: radio-over-fiber links, systems, and applications," *Photonics Research*, vol. 2, no. 4, pp. B54-B63, 2014.

- [27] C. H. Cox III and C. H. Cox, *Analog optical links: theory and practice*. Cambridge University Press, 2006.
- [28] S. Iezekiel, *Microwave photonics: devices and applications*. John Wiley & Sons, 2009.
- [29] V. J. Urick, J. D. McKinney, J. F. Diehl, and K. J. Williams, "Fiber-optic links with all-photonic RF gain and low RF noise figure," in *Microwave Symposium Digest (MTT), 2011 IEEE MTT-S International*, 2011, pp. 1-4: IEEE.
- [30] E. I. Ackerman, G. E. Betts, W. K. Burns, C. H. Cox, M. R. Phillips, and H. Roussel, "Low-noise-figure photonic links without pre-amplification," in *Sarnoff Symposium, 2009. SARNOFF'09. IEEE*, 2009, pp. 1-4: IEEE.
- [31] C. H. Cox and E. I. Ackerman, "Photonics for simultaneous transmit and receive," in *Microwave Symposium Digest (MTT), 2011 IEEE MTT-S International*, 2011, pp. 1-4: IEEE.
- [32] R. B. Waterhouse and D. Novak, "Integrated antenna/electro-optic modulator for RF photonic front-ends," in *Microwave Symposium Digest (MTT), 2011 IEEE MTT-S International*, 2011, pp. 1-4: IEEE.
- [33] R. T. Schermer, F. Bucholtz, C. A. Villarruel, J. G. Gil, T. D. Andreadis, and K. J. Williams, "Investigation of electrooptic modulator disruption by microwave-induced transients," *Optics express*, vol. 17, no. 25, pp. 22586-22602, 2009.
- [34] H. Haus *et al.*, "Representation of noise in linear twoports," *Proceedings of the IRE*, vol. 48, no. 1, pp. 69-74, 1960.
- [35] G. P. Agrawal, *Fiber-Optic Communication Systems*. Wiley Online Library, 1997.
- [36] C. Cox, E. Ackerman, R. Helkey, and G. E. Betts, "Direct-detection analog optical links," *IEEE Transactions on Microwave theory and techniques*, vol. 45, no. 8, pp. 1375-1383, 1997.
- [37] L. A. Coldren, S. W. Corzine, and M. L. Mashanovitch, *Diode lasers and photonic integrated circuits*. John Wiley & Sons, 2012.
- [38] H. Shi *et al.*, "Relative intensity noise measurements of a widely tunable sampled-grating DBR laser," *IEEE Photonics Technology Letters*, vol. 14, no. 6, pp. 759-761, 2002.
- [39] P. W. Juodawlkis *et al.*, "High-power, low-noise 1.5- μ m slab-coupled optical waveguide (SCOW) emitters: physics, devices, and applications," *IEEE Journal of Selected Topics in Quantum Electronics*, vol. 17, no. 6, pp. 1698-1714, 2011.

- [40] Y.-G. Zhao *et al.*, "High-power and low-noise DFB semiconductor lasers for RF photonic links," in *Avionics, Fiber-Optics and Photonics Technology Conference (AVFOP), 2012 IEEE*, 2012, pp. 66-67: IEEE.
- [41] A. Nikolov, D. Guenther, W. Liu, R. Cendejas, and R. Dutt, "Advancements and challenges for photonic components for avionic interconnects," in *Avionics, Fiber-Optics and Photonics Conference (AVFOP), 2013 IEEE*, 2013, pp. 5-6: IEEE.
- [42] E. Ackerman, S. Wanuga, D. Kasemset, A. S. Daryoush, and N. R. Samant, "Maximum dynamic range operation of a microwave external modulation fiber-optic link," *IEEE transactions on microwave theory and techniques*, vol. 41, no. 8, pp. 1299-1306, 1993.
- [43] M. L. Farwell, W. S. Chang, and D. R. Huber, "Increased linear dynamic range by low biasing the Mach-Zehnder modulator," *IEEE Photonics Technology Letters*, vol. 5, no. 7, pp. 779-782, 1993.
- [44] M. LaGasse, W. Charczenko, M. Hamilton, and S. Thaniyavarn, "Optical carrier filtering for high dynamic range fibre optic links," *Electronics Letters*, vol. 30, no. 25, pp. 2157-2158, 1994.
- [45] E. I. Ackerman *et al.*, "Signal-to-noise performance of two analog photonic links using different noise reduction techniques," in *Microwave Symposium, 2007. IEEE/MTT-S International*, 2007, pp. 51-54: IEEE.
- [46] A. Karim and J. Devenport, "Low noise figure microwave photonic link," in *Microwave Symposium, 2007. IEEE/MTT-S International*, 2007, pp. 1519-1522: IEEE.
- [47] A. Karim and J. Devenport, "Noise figure reduction in externally modulated analog fiber-optic links," *IEEE photonics technology letters*, vol. 19, no. 5, pp. 312-314, 2007.
- [48] R. W. Ridgway, C. L. Dohrman, and J. A. Conway, "Microwave photonics programs at DARPA," *Journal of Lightwave Technology*, vol. 32, no. 20, pp. 3428-3439, 2014.
- [49] W. B. Bridges and J. H. Schaffner, "Distortion in linearized electrooptic modulators," *Microwave Theory and Techniques, IEEE Transactions on*, vol. 43, no. 9, pp. 2184-2197, 1995.
- [50] J. Capmany, G. Li, C. Lim, and J. Yao, "Microwave photonics: current challenges towards widespread application," *Optics express*, vol. 21, no. 19, pp. 22862-22867, 2013.
- [51] E. I. Ackerman *et al.*, "RF-over-fiber links with very low noise figure," *Journal of Lightwave Technology*, vol. 26, no. 15, pp. 2441-2448, 2008.

- [52] H. V. Roussel *et al.*, "Gain, noise figure and bandwidth-limited dynamic range of a low-biased external modulation link," in *Microwave Photonics, 2007 IEEE International Topical Meeting on*, 2007, pp. 84-87: IEEE.
- [53] A. J. Seeds and K. J. Williams, "Microwave photonics," *Journal of Lightwave Technology*, vol. 24, no. 12, pp. 4628-4641, 2006.
- [54] R. Kalman, J. Fan, and L. Kazovsky, "Dynamic range of coherent analog fiber-optic links," *Journal of Lightwave Technology*, vol. 12, no. 7, pp. 1263-1277, 1994.
- [55] J. M. Wyrwas and M. C. Wu, "Dynamic range of frequency modulated direct-detection analog fiber optic links," *Journal of Lightwave Technology*, vol. 27, no. 24, pp. 5552-5562, 2009.
- [56] A. L. Campillo, "Interchannel nonlinear crosstalk in analog polarization modulated WDM systems," *Journal of lightwave technology*, vol. 24, no. 3, p. 1186, 2006.
- [57] V. J. Urick, J. F. Diehl, M. N. Draa, J. D. McKinney, and K. J. Williams, "Wideband analog photonic links: some performance limits and considerations for multi-octave implementations," in *SPIE OPTO*, 2012, pp. 825904-825904-14: International Society for Optics and Photonics.
- [58] Y. Li and P. Herczfeld, "Coherent PM optical link employing ACP-PPLL," *Journal of Lightwave Technology*, vol. 27, no. 9, pp. 1086-1094, 2009.
- [59] C. H. Cox, G. E. Betts, and L. M. Johnson, "An analytic and experimental comparison of direct and external modulation in analog fiber-optic links," *IEEE Transactions on microwave theory and techniques*, vol. 38, no. 5, pp. 501-509, 1990.
- [60] A. Yariv and P. Yeh, *Optical waves in crystals*. Wiley New York, 1984.
- [61] E. Chen and A. Murphy, *Broadband optical modulators: science, technology, and applications*. CRC press, 2011.
- [62] D. R. Maack, "Reliability of lithium niobate Mach Zehnder modulators for digital optical fiber telecommunication systems," *Critical reviews of optical science and technology*, pp. 197-230, 1999.
- [63] G. Li and P. Yu, "Optical intensity modulators for digital and analog applications," *Journal of Lightwave Technology*, vol. 21, no. 9, pp. 2010-2030, 2003.
- [64] K. Noguchi, O. Mitomi, and H. Miyazawa, "Millimeter-wave Ti: LiNbO₃ optical modulators," *Journal of Lightwave Technology*, vol. 16, no. 4, p. 615, 1998.

- [65] U. V. Cummings, "Linearized and high frequency electrooptic modulators," California Institute of Technology, 2005.
- [66] L. A. Coldren *et al.*, "High performance InP-based photonic ICs—A tutorial," *Journal of Lightwave Technology*, vol. 29, no. 4, pp. 554-570 %@ 0733-8724, 2011.
- [67] D. Marpaung, C. Roeloffzen, R. Heideman, A. Leinse, S. Sales, and J. Capmany, "Integrated microwave photonics," *Laser & Photonics Reviews*, vol. 7, no. 4, pp. 506-538, 2013.
- [68] H. Ma, A. Y. Jen, and L. R. Dalton, "Polymer-based optical waveguides: materials, processing, and devices," *Advanced materials*, vol. 14, no. 19, pp. 1339-1365, 2002.
- [69] J. Liu, G. Xu, F. Liu, I. Kityk, X. Liu, and Z. Zhen, "Recent advances in polymer electro-optic modulators," *RSC Advances*, vol. 5, no. 21, pp. 15784-15794, 2015.
- [70] L. R. Dalton, P. A. Sullivan, and D. H. Bale, "Electric field poled organic electro-optic materials: state of the art and future prospects," *Chemical reviews*, vol. 110, no. 1, pp. 25-55, 2009.
- [71] O. D. Herrera *et al.*, "Silica/electro-optic polymer optical modulator with integrated antenna for microwave receiving," *Journal of Lightwave Technology*, vol. 32, no. 20, pp. 3861-3867, 2014.
- [72] S. Kalluri *et al.*, "Monolithic integration of waveguide polymer electrooptic modulators on VLSI circuitry," *IEEE Photonics Technology Letters*, vol. 8, no. 5, pp. 644-646, 1996.
- [73] B. Bortnik *et al.*, "Electrooptic polymer ring resonator modulation up to 165 GHz," *Selected Topics in Quantum Electronics, IEEE Journal of*, vol. 13, no. 1, pp. 104-110, 2007.
- [74] S. Takahashi *et al.*, "Photo-stability measurement of electro-optic polymer waveguides with high intensity at 1550-nm wavelength," *Journal of Lightwave Technology*, vol. 27, no. 8, pp. 1045-1050, 2009.
- [75] B. Li *et al.*, "Recent advances in commercial electro-optic polymer modulator," in *Optical Fiber Communication and Optoelectronics Conference, 2007 Asia*, 2007, pp. 115-117: IEEE.
- [76] J. Luo *et al.*, "Phenyltetraene-based nonlinear optical chromophores with enhanced chemical stability and electrooptic activity," *Organic letters*, vol. 9, no. 22, pp. 4471-4474, 2007.
- [77] T. Ismail, C.-P. Liu, J. E. Mitchell, and A. J. Seeds, "High-dynamic-range wireless-over-fiber link using feedforward linearization," *Journal of Lightwave Technology*, vol. 25, no. 11, pp. 3274-3282, 2007.

- [78] S. R. O'Connor, T. R. Clark Jr, and D. Novak, "Wideband adaptive feedforward photonic link," *Journal of Lightwave Technology*, vol. 26, no. 15, pp. 2810-2816, 2008.
- [79] B. B. Dingel, "Ultra-linear, broadband optical modulator for high performance analog fiber link system," in *Microwave Photonics, 2004. MWP'04. 2004 IEEE International Topical Meeting on*, 2004, pp. 241-244: IEEE.
- [80] B. Dingel, N. Madamopoulos, A. Prescod, and R. Madabhushi, "Analytical model, analysis and parameter optimization of a super linear electro-optic modulator (SFDR> 130dB)," *Optics Communications*, vol. 284, no. 24, pp. 5578-5587, 2011.
- [81] N. Madamopoulos, B. Dingel, and A. Prescod, "Interferometric modulator with phase-modulating and cavity-modulating components (IMPACC) for high linearity microwave applications: technology review," in *International Conference on Photonics Solutions 2013*, 2013, pp. 888300-888300-12: International Society for Optics and Photonics.
- [82] A. Karim and J. Devenport, "High dynamic range microwave photonic links for RF signal transport and RF-IF conversion," *Journal of Lightwave Technology*, vol. 26, no. 15, pp. 2718-2724, 2008.
- [83] S. K. Korotky and R. M. de Ridder, "Dual parallel modulation schemes for low-distortion analog optical transmission," *IEEE journal on selected areas in communications*, vol. 8, no. 7, pp. 1377-1381, 1990.
- [84] J. L. Brooks, G. S. Maurer, and R. A. Becker, "Implementation and evaluation of a dual parallel linearization system for AM-SCM video transmission," *Journal of Lightwave Technology*, vol. 11, no. 1, pp. 34-41, 1993.
- [85] S. Li, X. Zheng, H. Zhang, and B. Zhou, "Highly linear radio-over-fiber system incorporating a single-drive dual-parallel Mach-Zehnder modulator," *IEEE Photonics Technology Letters*, vol. 22, no. 24, pp. 1775-1777, 2010.
- [86] G. E. Betts, "Linearized modulator for suboctave-bandpass optical analog links," *IEEE Transactions on Microwave Theory and Techniques*, vol. 42, no. 12, pp. 2642-2649, 1994.
- [87] W. K. Burns, "Linearized optical modulator with fifth order correction," *Journal of Lightwave Technology*, vol. 13, no. 8, pp. 1724-1727, 1995.
- [88] G. Betts and F. O'Donnell, "Microwave analog optical links using suboctave linearized modulators," *IEEE Photonics Technology Letters*, vol. 8, no. 9, pp. 1273-1275, 1996.
- [89] L. M. Johnson and H. Roussel, "Reduction intermodulation distortion in interferometric optical modulators," *Optics letters*, vol. 13, no. 10, pp. 928-930, 1988.

- [90] B. M. Haas, V. J. Urick, J. D. McKinney, and T. E. Murphy, "Dual-wavelength linearization of optically phase-modulated analog microwave signals," *Journal of Lightwave Technology*, vol. 26, no. 15, pp. 2748-2753, 2008.
- [91] B. Hraimel *et al.*, "Experimental demonstration of mixed-polarization to linearize electro-absorption modulators in radio-over-fiber links," *IEEE Photonics Technology Letters*, vol. 23, no. 4, pp. 230-232, 2011.
- [92] G. C. Wilson *et al.*, "Predistortion of electroabsorption modulators for analog CATV systems at 1.55/spl mu/m," *Journal of lightwave technology*, vol. 15, no. 9, pp. 1654-1662, 1997.
- [93] L. Roselli *et al.*, "Analog laser predistortion for multiservice radio-over-fiber systems," *Journal of Lightwave Technology*, vol. 21, no. 5, p. 1211, 2003.
- [94] J. A. MacDonald, M. V. Kubak, and A. Katz, "Wideband dynamic range improvement of microwave photonic links," in *Avionics Fiber-Optics and Photonics, 2005. IEEE Conference*, 2005, pp. 67-68: IEEE.
- [95] V. J. Urick, M. S. Rogge, P. F. Knapp, L. Swingen, and F. Bucholtz, "Wide-band predistortion linearization for externally modulated long-haul analog fiber-optic links," *IEEE transactions on microwave theory and techniques*, vol. 54, no. 4, pp. 1458-1463, 2006.
- [96] Y. Shen, B. Hraimel, X. Zhang, G. E. Cowan, K. Wu, and T. Liu, "A novel analog broadband RF predistortion circuit to linearize electro-absorption modulators in multiband OFDM radio-over-fiber systems," *Microwave Theory and Techniques, IEEE Transactions on*, vol. 58, no. 11, pp. 3327-3335, 2010.
- [97] X. Xie, J. Khurgin, J. Kang, and F.-S. Chow, "Linearized Mach-Zehnder intensity modulator," *Photonics Technology Letters, IEEE*, vol. 15, no. 4, pp. 531-533, 2003.
- [98] H. Tazawa and W. H. Steier, "Bandwidth of linearized ring resonator assisted Mach-Zehnder modulator," *Photonics Technology Letters, IEEE*, vol. 17, no. 9, pp. 1851-1853, 2005.
- [99] A. Prescod, B. B. Dingel, N. Madamopoulos, and R. Madabhushi, "Effect of ring resonator waveguide loss on SFDR performance of highly linear optical modulators under suboctave operation," *Photonics Technology Letters, IEEE*, vol. 22, no. 17, pp. 1297-1299, 2010.
- [100] J. Cardenas *et al.*, "Linearized silicon modulator based on a ring assisted Mach Zehnder inteferometer," *Optics express*, vol. 21, no. 19, pp. 22549-22557, 2013.

- [101] C. Zhang, P. A. Morton, J. B. Khurgin, J. D. Peters, and J. E. Bowers, "Ultralinear heterogeneously integrated ring-assisted Mach-Zehnder interferometer modulator on silicon," *Optica*, vol. 3, no. 12, pp. 1483-1488, 2016/12/20 2016.
- [102] E. I. Ackerman, "Broad-band linearization of a Mach-Zehnder electrooptic modulator," *IEEE Transactions on Microwave Theory and Techniques*, vol. 47, no. 12, pp. 2271-2279, 1999.
- [103] H. Tazawa *et al.*, "Ring resonator-based electrooptic polymer traveling-wave modulator," *Journal of lightwave technology*, vol. 24, no. 9, p. 3514, 2006.
- [104] P. Absil, J. Hryniewicz, B. Little, R. Wilson, L. Joneckis, and P.-T. Ho, "Compact microring notch filters," *IEEE Photonics Technology Letters*, vol. 12, no. 4, pp. 398-400, 2000.
- [105] B. Little *et al.*, "Very high-order microring resonator filters for WDM applications," *IEEE Photonics Technology Letters*, vol. 16, no. 10, pp. 2263-2265, 2004.
- [106] B. E. Little, S. T. Chu, H. A. Haus, J. Foresi, and J.-P. Laine, "Microring resonator channel dropping filters," *Journal of lightwave technology*, vol. 15, no. 6, pp. 998-1005, 1997.
- [107] H. L. Lira, S. Manipatruni, and M. Lipson, "Broadband hitless silicon electro-optic switch for on-chip optical networks," *Optics Express*, vol. 17, no. 25, pp. 22271-22280, 2009.
- [108] V. Van *et al.*, "All-optical nonlinear switching in GaAs-AlGaAs microring resonators," *IEEE Photonics Technology Letters*, vol. 14, no. 1, pp. 74-76, 2002.
- [109] B. Liu, A. Shakouri, and J. E. Bowers, "Wide tunable double ring resonator coupled lasers," *IEEE Photonics Technology Letters*, vol. 14, no. 5, pp. 600-602, 2002.
- [110] T. Chu, N. Fujioka, and M. Ishizaka, "Compact, lower-power-consumption wavelength tunable laser fabricated with silicon photonic wire waveguide micro-ring resonators," *Optics express*, vol. 17, no. 16, pp. 14063-14068, 2009.
- [111] C.-Y. Chao, W. Fung, and L. J. Guo, "Polymer microring resonators for biochemical sensing applications," *IEEE Journal of selected Topics in quantum electronics*, vol. 12, no. 1, pp. 134-142, 2006.
- [112] Y. Sun and X. Fan, "Optical ring resonators for biochemical and chemical sensing," *Analytical and bioanalytical chemistry*, vol. 399, no. 1, pp. 205-211, 2011.
- [113] J. Heebner, R. Grover, T. Ibrahim, and T. A. Ibrahim, *Optical microresonators: theory, fabrication, and applications*. Springer Science & Business Media, 2008.

- [114] O. Schwelb, "Transmission, group delay, and dispersion in single-ring optical resonators and add/drop filters-a tutorial overview," *Journal of Lightwave Technology*, vol. 22, no. 5, pp. 1380-1394, 2004.
- [115] Q. Xu, B. Schmidt, S. Pradhan, and M. Lipson, "Micrometre-scale silicon electro-optic modulator," *Nature*, vol. 435, no. 7040, pp. 325-327, 2005.
- [116] L. Zhang *et al.*, "Microring-based modulation and demodulation of DPSK signal," *Optics express*, vol. 15, no. 18, pp. 11564-11569, 2007.
- [117] Y. Vlasov, W. M. Green, and F. Xia, "High-throughput silicon nanophotonic wavelength-insensitive switch for on-chip optical networks," *nature photonics*, vol. 2, no. 4, pp. 242-246, 2008.
- [118] A. Yariv, "Universal relations for coupling of optical power between microresonators and dielectric waveguides," *Electronics Letters*, vol. 36, no. 4, pp. 321-322, 2000.
- [119] A. Yariv, "Critical coupling and its control in optical waveguide-ring resonator systems," *IEEE Photonics Technology Letters*, vol. 14, no. 4, pp. 483-485, 2002.
- [120] W. D. Sacher and J. K. Poon, "Dynamics of microring resonator modulators," *Optics express*, vol. 16, no. 20, pp. 15741-15753, 2008.
- [121] I. L. Gheorma and R. M. Osgood, "Fundamental limitations of optical resonator based high-speed EO modulators," *IEEE Photonics Technology Letters*, vol. 14, no. 6, pp. 795-797, Jun 2002.
- [122] H. Tazawa and W. Steier, "Linearity of ring resonator-based electro-optic polymer modulator," *Electronics Letters*, vol. 41, no. 23, pp. 1297-1298, 2005.
- [123] M. Song, L. Zhang, R. G. Beausoleil, and A. E. Willner, "Nonlinear distortion in a silicon microring-based electro-optic modulator for analog optical links," *Selected Topics in Quantum Electronics, IEEE Journal of*, vol. 16, no. 1, pp. 185-191, 2010.
- [124] A. Ayazi, T. Baehr-Jones, Y. Liu, A. E.-J. Lim, and M. Hochberg, "Linearity of silicon ring modulators for analog optical links," *Opt. Express* 20 (12), pp. 13115-13122, 2012.
- [125] W. Fegadolli, J. E. B. Oliveira, and V. R. Almeida, "Highly linear electro-optic modulator based on ring resonator," *Microwave and Optical Technology Letters*, vol. 53, no. 10, pp. 2375-2378, 2011.
- [126] H. Tazawa and W. H. Steier, "Analysis of ring resonator-based traveling-wave modulators," *Photonics Technology Letters, IEEE*, vol. 18, no. 1, pp. 211-213, 2006.

- [127] S. Hunziker and W. Baechtold, "Simple model for fundamental intermodulation analysis of RF amplifiers and links," *Electronics Letters*, vol. 32, no. 19, pp. 1826-1827, 1996.
- [128] R. C. Alferness, "Waveguide electrooptic modulators," *IEEE Transactions on Microwave Theory Techniques*, vol. 30, pp. 1121-1137, 1982.
- [129] H. Zhang *et al.*, "Push-pull electro-optic polymer modulators with low half-wave voltage and low loss at both 1310 and 1550 nm," *Applied Physics Letters*, vol. 78, no. 20, pp. 3136-3138, 2001.
- [130] W. H. Steier *et al.*, "Electro-Optic Polymer Ring Resonators for Millimeter-Wave Modulation and Optical Signal Processing," in *Practical Applications of Microresonators in Optics and Photonics*, 2009, p. 265.
- [131] A. Hosseinzadeh and C. T. Middlebrook, "Highly linear dual ring resonator modulator for wide bandwidth microwave photonic links," *Optics Express*, vol. 24, no. 24, pp. 27268-27279, 2016.
- [132] Y. Fu, X. Zhang, B. Hraimel, T. Liu, and D. Shen, "Mach-Zehnder: a review of bias control techniques for Mach-Zehnder modulators in photonic analog links," *IEEE Microwave Magazine*, vol. 14, no. 7, pp. 102-107, 2013.
- [133] A. Hosseinzadeh and C. T. Middlebrook, "Design and optimization of polymer ring resonator modulators for analog microwave photonic applications," in *SPIE OPTO*, 2016, pp. 97471L-97471L-10: International Society for Optics and Photonics.
- [134] "IEEE Standard for Information technology-- Local and metropolitan area networks-- Specific requirements-- Part 15.3: Amendment 2: Millimeter-wave-based Alternative Physical Layer Extension," *IEEE Std 802.15.3c-2009 (Amendment to IEEE Std 802.15.3-2003)*, pp. 1-200, 2009.
- [135] B. A. Block *et al.*, "Electro-optic polymer cladding ring resonator modulators," *Optics Express*, vol. 16, no. 22, pp. 18326-18333, 2008/10/27 2008.
- [136] J. Du and J. Wang, "Experimental performance evaluation of analog signal transmission in a silicon microring resonator," *Optics letters*, vol. 40, no. 7, pp. 1181-1184, 2015.
- [137] J. Takayesu *et al.*, "A Hybrid Electrooptic Microring Resonator-Based $1 \times 4 \times 1$ ROADM for Wafer Scale Optical Interconnects," *Journal of Lightwave Technology*, vol. 27, no. 4, pp. 440-448, 2009.
- [138] A. V. Lavrinenko, J. Lægsgaard, N. Gregersen, F. W. Schmidt, and T. Søndergaard, *Numerical Methods in Photonics*. 2015.
- [139] A. Taflove and S. C. Hagness, *Computational electrodynamics*. Artech house, 2005.

- [140] K. Saitoh and M. Koshiba, "Full-vectorial finite element beam propagation method with perfectly matched layers for anisotropic optical waveguides," *Journal of lightwave technology*, vol. 19, no. 3, pp. 405-413, 2001.
- [141] W. Huang and C. Xu, "Simulation of three-dimensional optical waveguides by a full-vector beam propagation method," *IEEE journal of quantum electronics*, vol. 29, no. 10, pp. 2639-2649, 1993.
- [142] K. Okamoto, *Fundamentals of optical waveguides*. Academic press, 2010.
- [143] J. E. Toney, "Multiphysics Modeling of Electro-Optic Devices," *Comsol 2011*, 2011.
- [144] M.-C. Oh *et al.*, "Recent advances in electrooptic polymer modulators incorporating highly nonlinear chromophore," *IEEE Journal of selected topics in quantum electronics*, vol. 7, no. 5, pp. 826-835, 2001.
- [145] A. W. Snyder and J. Love, *Optical waveguide theory*. Springer Science & Business Media, 2012.
- [146] R. A. Soref, J. Schmidtchen, and K. Petermann, "Large single-mode rib waveguides in GeSi-Si and Si-on-SiO₂," *IEEE Journal of Quantum Electronics*, vol. 27, no. 8, pp. 1971-1974, 1991.
- [147] S. P. Pogossian, L. Vescan, and A. Vonsovici, "The single-mode condition for semiconductor rib waveguides with large cross section," *Journal of Lightwave Technology*, vol. 16, no. 10, pp. 1851-1853, 1998.
- [148] B. A. Rahman, V. Haxha, S. Haxha, and K. T. Grattan, "Design optimization of polymer electrooptic modulators," *Journal of lightwave technology*, vol. 24, no. 9, p. 3506, 2006.
- [149] M. Lee *et al.*, "Broadband modulation of light by using an electro-optic polymer," *Science*, vol. 298, no. 5597, pp. 1401-1403, 2002.
- [150] S. Michel, J. Zyss, I. Ledoux-Rak, and C. T. Nguyen, "High-performance electro-optic modulators realized with a commercial side-chain DR1-PMMA electro-optic copolymer," in *OPTO*, 2010, pp. 75990I-75990I-14: International Society for Optics and Photonics.
- [151] R. Himmelhuber *et al.*, "A Silicon-polymer hybrid modulator—design, simulation and proof of principle," *Journal of Lightwave Technology*, vol. 31, no. 24, pp. 4067-4072, 2013.
- [152] W. Hartmann *et al.*, "100 Gbit/s OOK using a silicon-organic hybrid (SOH) modulator," in *Optical Communication (ECOC), 2015 European Conference on*, 2015, pp. 1-3: IEEE.

- [153] X. Sun *et al.*, "Effect of film compatibility on electro-optic properties of dye doped polymer DR1/SU-8," *Applied Surface Science*, vol. 285, pp. 469-476, 2013.
- [154] H. C. Ling, W. Holland, and H. Gordon, "dc electrical behavior of polymers used in electro-optic devices," *Journal of applied physics*, vol. 70, no. 11, pp. 6669-6673, 1991.
- [155] M. Briseno, "Electro-Optic Contact Poling of Polymer Waveguide Devices and Thin Films," 2017.
- [156] B. A. Block *et al.*, "Electro-optic polymer cladding ring resonator modulators," *Optics Express*, vol. 16, no. 22, pp. 18326-18333, 2008.
- [157] L. Chen, J. Chen, J. Nagy, and R. M. Reano, "Highly linear ring modulator from hybrid silicon and lithium niobate," *Optics Express*, vol. 23, no. 10, pp. 13255-13264, 2015/05/18 2015.
- [158] J.-W. Kang, J.-S. Kim, and J.-J. Kim, "Optimized oxygen plasma etching of polycarbonate for low-loss optical waveguide fabrication," *Japanese Journal of Applied Physics*, vol. 40, no. 5R, p. 3215, 2001.
- [159] C.-Y. Chao and L. J. Guo, "Reduction of surface scattering loss in polymer microrings using thermal-reflow technique," *IEEE Photonics Technology Letters*, vol. 16, no. 6, pp. 1498-1500, 2004.